UNIVERSITY OF CALIFORNIA
Los Angeles

A New Tool for Preparing Ultracold Atoms and Molecules

A dissertation submitted in partial satisfaction
of the requirements for the degree
Doctor of Philosophy in Physics

by

Xueping Long

2019

ABSTRACT OF THE DISSERTATION

A New Tool for Preparing Ultracold Atoms and Molecules

by

Xueping Long
Doctor of Philosophy in Physics
University of California, Los Angeles, 2019
Professor Wesley C. Campbell, Chair

Laser cooling and trapping has been essential to the study of ultracold atoms. Conventionally, continuous wave (CW) lasers have been used almost exclusively to transfer momentum to atoms, which is necessary for laser cooling and trapping. In this thesis, I will describe a technique to laser cool and trap atoms with optical frequency comb generated by a mode-locked (ML) laser, which is another type of laser that is better known as a metrology tool.

While atomic magneto-optical trap (MOT), a spatially confined atomic sample created with laser cooling and trapping, has become the workhorse of ultracold atomic physics since its first demonstration a few decades ago [80, 52], the first molecular MOT was only demonstrated a few years ago [13, 76, 89, 92, 8, 7], with a relatively low number of molecules (≈ 5 [8]). The main reason for the low number of molecules in the trap is the low number of molecules that can be slowed to a laser trappable speed, which is due to their high likelihood of spontaneous emission into dark states. In this thesis I will also describe a mode-locked laser slowing technique that suppresses spontaneous emission.

The dissertation of Xueping Long is approved.

Eric R. Hudson

Stuart Brown

Louis-Serge Bouchard

Wesley C. Campbell, Committee Chair

University of California, Los Angeles

2019

To my family and friends

Table of Contents

List of Figures . . . . **viii**

Preface . . . . **xi**

Curriculum Vitae . . . . **xii**

1 Introduction **1**

1.1 Optical Frequency Comb Laser Cooling and Trapping 2

1.2 Suppressed spontaneous emission for coherent momentum transfer 4

2 Direct Frequency Comb Laser Cooling and Trapping **6**

2.1 Introduction 6

2.2 Dopper Cooling and Doppler Temperature 7

2.3 Magneto-Optical Trap 12

2.3.1 Measuring MOT Temperature 15

2.4 Optical Frequency Comb Two-Photon Cooling and Trapping 16

2.4.1 Scattering rate from a frequency comb 16

2.4.2 Doppler Limit for Two-Photon Optical Molasses 19

2.5 Experiment Results 22

2.5.1 Laser Tooth Linewidth Modification 23

2.5.2 Optical Frequency Comb Two-Photon Laser Cooling 27

2.5.3 Optical Frequency Comb Two-Photon MOT 34

2.6 Outlook 37

3 Momentum Transfer via a Stimulated Force **40**

3.1 Advantages of Using a Stimulated Force for Laser Slowing 40
3.2 Stimulated Force Slowing with ML Laser Pulses 42
  3.2.1 Single Photon Cooling 44
3.3 Benchmarking Stimulated Force with ML Laser Pulses 45
3.4 Single ML Pulse (Pair) Excitations 45
  3.4.1 Atomic Excitation by a Mode-Locked Pulse 46
  3.4.2 π-Pulse Condition 50
  3.4.3 Single Pulse (Pair) Excitation for a Finite Size Sample 52
  3.4.4 Experimental Results on Single-Pulse(-Pair)-Induced MOT Fluorescence 56
3.5 Momentum Transfer with ML Pulse Stimulated Force 63
  3.5.1 Theoretical Description of Momentum Transfer from a ML Pulse Stimulated Force 63
  3.5.2 Experimental Characterization of Momentum Transfer with a ML Pulse Stimulated Force 64
  3.5.3 Comb Tooth Effect 68
3.6 Comparison of the ML Pulse Stimulated Force to Other Forces 73
3.7 Application of the ML Pulse Stimulated Force 75

4 Conclusion 76

5 Experiment Apparatus and Software 77
5.1 LabRAD 77
5.2 Tsunami Mode-locked Ti:sapphire laser 77
  5.2.1 Pulse Picking with Conoptics Pockels Cell 78
  5.2.2 Locking the ML laser 79
5.3 CW Lasers 80

5.3.1 Saturated Absorption Lock 80
5.3.2 Cooling and Repumping Lasers 83

Appendix A Variance in Number of Momentum Transfers and Spread in TOF Arrival Times 85

Appendix B Dual Species MOT 87

Bibliography 90

List of Figures

2.1 Velocity dependent force from two counter-propagating red-detuned laser light beams . . . 9

2.2 Arrangement for a MOT in 1D . . . 13

2.3 Constructive interference of multiple paths in a two-photon transition driven by a transform-limited optical frequency comb . . . 17

2.4 Relevant levels of ^{85}Rb for two-photon laser cooling and trapping . . . 23

2.5 Laser-induced fluorescence spectrum of the $5S \rightarrow 5D$ two-photon transition driven by an optical frequency comb . . . 24

2.6 Blue fluorescing MOT . . . 26

2.7 Absorption images of the atom cloud after free expansion following . . . 28

2.8 Sample absorption image of a laser-cooled atomic cloud. . . . 29

2.9 Detuning dependence of 420 nm fluorescence and the resulting temperature of rubidium atoms laser-cooled by an optical frequency comb on a two-photon transition . . . 31

2.10 Temperature v.s. time when the laser detuning is optimized for cooling . . . 32

2.11 Time decay of the 420 nm fluorescence . . . 33

2.12 Position space trajectories for atoms trapped in a two-photon, optical frequency comb MOT . . . 35

2.13 Phase space trajectories for atoms trapped in a two-photon, optical frequency comb MOT . . . 36

2.14 Calculated parameters for laser cooling atomic hydrogen on $1S \rightarrow 3D$ . . . 39

3.1 Presence of rotational and vibrational motions in a diatomic molecule. . . . 41

3.2 Energy level diagram of CaF . . . 42

3.3 Pulse sequence of the stimulated force 43

3.4 Experimental setup for single-pulse(-pair)-induced MOT fluorescence 57

3.5 Fluorescence from single pulse (pair) 58

3.6 Sample time trace of fluorescence after single ML pulse (pair) illumination . . . 59

3.7 Laser power fluctuation 61

3.8 Fits to fluorescence data 62

3.9 Experiment setup for measuring momentum transfers resulted from ML laser pulse 65

3.10 Time domain and frequency domain illustration of single-beam processes in this work 66

3.11 TOF traces of a good versus bad ML laser pulse power for efficient momentum transfer 67

3.12 Effect of varying pulse energy on the arrival times of the atoms at the TOF detection position 69

3.13 Sample TOF trace 70

3.14 Arrival times of the fastest 10% of the atoms at 5 different TOF detection positions, and the velocity fit 70

3.15 Stimulated force comb tooth dependence 72

3.16 Calculated quasi-steady-state normalized scattering rate for illumination by a ML pulse train 73

5.1 Illustration of a spectrum analyzer data for a well-mode-locked frequency comb 78

5.2 Heated rubidium vapor cell 79

5.3 Schematic for the saturated absorption lock 81

5.4 Electronics circuit for the saturated absorption lock 82

5.5 Saturated absorption lock signal 82

5.6 Schematic for the offset lock optics 83

5.7 Electronics circuit for the offset lock 84

B.1 Simultaneous dual species MOT absorption as probe laser frequency is scanned. 87

B.2 Simultaneous dual species MOT absorption as probe laser frequency is scanned. 88

PREFACE

First and foremost I would like to thank my Professor Wesley C. Campbell. His patience and support made it possible for me to get through the difficult times when experiments did not work as expected (which is 90% of time).

I would like to thank Professor Andrew Jayich, the postdoc and my mentor when I first joined the experiment. He taught me how to be a scientist, and his work ethics and persistence changed me as a person.

Last but not least I would like to thank my friends in and out of the Campbell lab, as well as my family, without whom it would not be possible for me to get through these six years.

Curriculum Vitae

2009 – 2013	B.A. in Physics, Reed College, Portland, Oregon, USA
2013 – Present	Ph.D. student in Physics, University of California, Los Angeles (UCLA).

Publications

Xueping Long, Seejia S. Yu, Andrew M. Jayich, and Wesley C. Campbell, "Suppressed spontaneous emission for coherent momentum transfer," (Accepted for publication in PRL, ArXiv:1903.01627).

Michael Ip, Anthony Ransford, Andrew M. Jayich, Xueping Long, Conrad Roman, and Wesley C. Campbell, "Phonon lasing from optical frequency comb illumination of trapped ions," Phys. Rev. Lett. 121, 043201 (2018).

Andrew M. Jayich, Xueping Long, and Wesley C. Campbell, "Direct Frequency Comb Laser Cooling and Trapping," Phys. Rev. X 6, 041004 (2016).

CHAPTER 1

Introduction

Laser cooling and trapping has been essential to the study of ultracold atoms. Conventionally, continuous wave (CW) lasers have been used almost exclusively to transfer momentum to atoms, which is necessary for laser cooling and trapping. In this thesis, I will describe a technique to laser cool and trap atoms with optical frequency comb generated by a mode-locked (ML) laser, which is another type of laser that is better known as a metrology tool.

While atomic magneto-optical trap (MOT), a spatially confined atomic sample created with laser cooling and trapping, has become the workhorse of ultracold atomic physics since its first demonstration a few decades ago [80, 52], the first molecular MOT was only demonstrated a few years ago [13, 76, 89, 92, 8, 7], with a relatively low number of molecules (≈ 5 [8]). The main reason for the low number of molecules in the trap is the low number of molecules that can be slowed to a laser trappable speed, which is due to their high likelihood of spontaneous emission into dark states. In this thesis I will also describe a mode-locked laser slowing technique that suppresses spontaneous emission.

1.1 Optical Frequency Comb Laser Cooling and Trapping

Laser cooling and trapping has played a paramount role in many atomic physics experiments. For example, many precision measurement experiments eventually need a determination of a frequency shift $\Delta\omega$ between two sublevels in the system. The shot-noise limit of frequency sensitivity for such a measurement is given by $\delta(\Delta\omega) = 1/(2\pi\tau\sqrt{N})$, where τ is the coherence time of the experiment, and N is the number of detected particles [23]. Laser cooling decreases this limit in two different ways: the low temperature allows atoms to be put into a single quantum state, thus N can be increased by increasing the number of detectable particles (this is especially true for molecules, because of the many rotational and vibrational states in additional to the hyperfine states); in general laser cooled atoms are slow moving in the laboratory frame, hence the interrogation time is also increased, potentially resulting in larger τ. Further increases in τ could result if atoms are confined in a trap, for instance in a magneto-optical trap (MOT), which would further decrease the shot-noise limit. In addition, laser cooling and trapping enable precise control and manipulation of quantum state, and has led to recent advances in quantum information [38, 19], the search to understand dark energy [41], and quantum sensors [30]. Laser cooling and trapping has recently enabled the measurement and control of ultracold chemical reactions at a new level of detail [103, 27] with molecules made from alkali atoms that are well-suited to CW laser technology.

Laser cooled and trapped sample of hydrogen, in particular, is highly desirable. Spectroscopy of the $^1S \rightarrow {}^2S$ transition in hydrogen is also of great scientific interest. This transition, together with subsequent transitions of the ^2S state to higher states, collectively determine the Rydberg constant, the proton radius, and ultimately provides a test of quantum electrodynamics [26, 74, 17]. Although this transition can now be determined with an incredibly small fractional uncertainty of 4.2×10^{-15} [78], higher precision with reduced systematic effects is desired to resolve mysteries such as the proton radius puzzle [74, 24], and laser cooled and trapped hydrogen will be instrumental. Meanwhile, spectroscopy on the same transition on anti-hydrogen, the antiparticle of hydrogen, requires 300s per data point [5], partially due to the relatively small interaction volume [24]. A sample of laser cooled and trapped anti-hydrogen can increase the interaction time significantly, potentially enables better data to be taken.

Despite the great scientific payoff laser cooled and trapped hydrogen and hydrogen, laser cooling of hydrogen has only been demonstrated once [86], mostly because of the lack of sufficiently powerful CW lasers in the deep ultraviolet (UV). For the same reason, other abundant and chemically interesting species, for example, carbon, nitrogen and oxygen, are not currently laser cooled and trapped, although they are likely to play prominent roles in other scientific fields such as astrophysics [47] and precision measurement [20], where the production of cold samples could help answer fundamental outstanding questions [34, 32, 42].

ML laser, on the other hand, is seldom used as a tool for control and manipulation of atomic and molecular motions [18], in spite of its very high instantaneous intensity that can be used for efficient production of UV light via frequency summing. Its power is divided into thousands or tens of thousands of evenly spaced spectral lines (an optical frequency comb). Most of the laser power would be wasted if only one or few comb teeth are used, unless some clever scheme is used that makes use of the entire frequency spectrum of the ML laser. It should be mentioned that Doppler cooling with combs has been investigated in a mode where each atom interacts with only one or two comb teeth at a time, which uses only a small fraction of the laser's total power [90, 95, 54, 10, 25].

In Chapter 2, following the observation of a pushing force by Marian *et al.* [70] and a proposal by Kielpinski [59], we utilize a coherent effect in far-detuned ML two-photon transitions [11] to laser cool atoms with all of the comb teeth contributing in parallel to enhance the scattering rate (Fig. 2.3). This technique is designed to utilize the high UV conversion efficiency of ML lasers without wasting any of the resulting UV power, and opens the door to laser cool H, C, N, O, and anti-hydrogen ($\bar{\mathrm{H}}$), species for which single-photon laser cooling is beyond the reach of even ML lasers [59]. We extend these ideas to create a magneto-optical trap, and find that the density of the comb spectrum introduces no measurable effects in our system, demonstrating that it may be possible to create MOTs of these species using this technique.

1.2 Suppressed spontaneous emission for coherent momentum transfer

The rich internal structures of polar molecules and their readily available long-range and anisotropic dipolar interactions make ultracold molecules uniquely promising candidates for precision measurements [98, 48, 94, 6, 65], quantum information processing [28, 9, 81, 50, 12, 73] and quantum chemistry [77, 67]. However, for molecules, spontaneous emission populates excited vibrational states, which has largely precluded the adaptation of atomic laser cooling techniques for molecules.

Recently, the workhorse of ultracold atomic physics, the magneto-optical trap (MOT), has been successfully demonstrated with some carefully chosen diatomic molecules [13, 76, 89, 92, 8, 7]. Despite this substantial step forward, the largest number of molecules that have been trapped in a MOT (≈ 5 [8]) is still orders of magnitude less than a typical atomic MOT. This number is primarily limited by the small fraction of molecules that can be slowed from a molecular beam to the MOT capture speed [71]. Further, extension of this technique to molecules with higher vibrational branching probability (such as polyatomics) will likely require new methods for beam deceleration.

While the most commonly used laser deceleration methods employ spontaneous radiation pressure, the time-averaged force is limited to a low value by the need to wait for spontaneous decay after each $\hbar k$ of momentum transfer. For molecules, slowing via spontaneous scattering has been limited to a handful of specially-chosen diatomic species [91, 14, 102, 46, 100, 79] with extremely low vibrational branching probabilities [31]. Moreover, multiple molecular transitions must be driven that connect various ground states to the same excited state, which further reduces the time-averaged force that can be achieved [16]. As a result, radiative deceleration of molecular beams leads to long slowing lengths and low trap capture efficiencies associated with molecule loss from transverse velocity spread and spontaneously populated excited vibrational states.

Various optical forces that utilize *stimulated* emission are being pursued (as recently reviewed by Metcalf [72]). For stimulated forces, a reasonable figure of merit for evaluating the gain in requisite cycle closure of stimulated over spontaneous scattering is the average momentum transferred (in units of the photon momentum, $\hbar k$) per spontaneous emission event, which we denote by the symbol Υ. For spontaneous scattering, $\Upsilon = 1$. For most stimulated scattering schemes, the stimulated processes can be driven quickly compared to the spontaneous emission lifetime, and the stimulated force can therefore be stronger than the spontaneous scattering force by a factor of approximately Υ.

In Chapter 3, we demonstrate and benchmark an optical force derived entirely from stimulated scattering of mode-locked (ML) laser pulses [58, 56]. Early work on this technique showed order-of-unity force gains over spontaneous scattering [93, 75, 39]. By using a pre-cooled sample of atoms to benchmark and optimize the force, we show that its performance can be substantially improved. We are able to achieve an average of $\Upsilon = (19^{+6}_{-4})$ momentum transfers of $\hbar k$ per spontaneous emission event. This potentially extends optical deceleration to molecules with state leakage probabilities an order of magnitude worse than currently used species, such as complex polyatomics [63] and molecules well-suited to precision measurement [65, 29, 69, 53].

CHAPTER 2

Direct Frequency Comb Laser Cooling and Trapping

2.1 Introduction

It is not immediately clear why laser cooling and trapping with mode-locked laser should be ever desirable. The broad spectrum coverage of the ML laser means the power on each frequency comb tooth is tiny, and using a ML laser for single photon cooling and trapping is undoubtedly wasteful. Yet, if a two-photon process is involved, then as we will see in this chapter, all the frequency comb teeth can coherently add up, leading to an efficient use of laser power. In addition, if a nonlinear effect (for example second harmonic generation) is involved in the process of generating the photons for the two-photon process, mode-locked laser can be more efficient overall, due to its high instantaneous intensity. As such, mode-locked laser can be useful for laser cooling and trapping species with ultra-violet transitions that are hard to reach with a conventional CW laser.

In this chapter, a technique to laser cool and trap using a mode-locked laser in the optical frequency comb regime is described, and results from applying this technique in 1D are presented.

2.2 Dopper Cooling and Doppler Temperature

Care needs to be taken when the notion of temperature is applied to in cold atoms, because a laser-cooled system may very well be in a steady-state but not in thermal equilibrium. In laser cooling, temperature can be used to describe an atomic sample with 1D average kinetic energy $\langle E_k \rangle$:

$$\frac{1}{2} k_B T = \langle E_k \rangle, \tag{2.1}$$

where k_B is the Boltzmann's constant. For an atomic sample trapped still in space (for example, by a magneto-optical trap), the kinetic energy can be written as

$$\langle E_k \rangle = \frac{1}{2} m_{\text{atom}} \langle v_z^2 \rangle, \tag{2.2}$$

where m_{atom} is the mass of an atom and $\langle v_z^2 \rangle$ is the 1D mean squared velocity of the atomic sample. Eq. (2.1) and (2.2) allows the temperature to be found by

$$T = \frac{m_{\text{atom}}}{k_B} \langle v_z^2 \rangle. \tag{2.3}$$

Eq. (2.3) also implies that a beam of fast moving atoms could be cold in the some reference frame as long as the spread in velocity is small. It also means that for spatially confined sample, narrowing its velocity spread would result in a colder sample.

In this section, following [35], we will derive a temperature limit for Doppler cooling. Doppler cooling relies on applying a velocity dependent force that "pushes" atoms toward zero velocity. One way to produce such a velocity dependent force is by illuminating the atomic sample with two counter-propagating laser beams. To see how this works, we define the on-resonance saturation parameter

$$s_0 \equiv 2|\Omega|^2/\Gamma^2 = I/I_s, \tag{2.4}$$

where Ω is the Rabi frequency, Γ the excited state decay rate, I the laser intensity and I_s the saturation intensity of a transition. In the low intensity limit where stimulated emission is not important, the scattering rate of light from a laser field is given by

$$\gamma_p = \frac{s_0 \Gamma/2}{1 + s_0 + (2\delta/\Gamma)^2} \tag{2.5}$$

Here, $\delta \equiv \omega_l - \omega_a$ is the laser detuning from the atomic resonance frequency. The scattering force from such a light beam is

$$\vec{F} = \gamma_p \hbar \vec{k} = \frac{\hbar \vec{k} \Gamma}{2} \frac{s_0}{1 + s_0 + (2\delta/\Gamma)^2}. \tag{2.6}$$

The sum of forces from two counter-propagating beams is

$$\vec{F}_{OM} \approx \frac{8\hbar k^2 \delta s_0}{\Gamma(1 + s_0 + (2\delta/\Gamma)^2)^2} \vec{v} = -\alpha \vec{v}, \tag{2.7}$$

where

$$\alpha = -\frac{8\hbar k^2 \delta s_0}{\Gamma(1 + s_0 + (2\delta/\Gamma)^2)^2}, \tag{2.8}$$

and terms of order $(kv/\Gamma)^4$ and higher have been neglected. Velocity dependence of this force is illustrated in Figure 2.1. Within the capture velocity ($v \leq v_{\mathrm{c}}$ where $v_{\mathrm{c}} = \Gamma/k$, indicated by the gray shaded region), this force is proportional to velocity with a negative gradient, resulting in a viscous damping slowing force. Atoms with the wrong velocity (moving away from zero) are pushed toward 0 by the negative velocity gradient. This technique is known as "optical molasses."

To find the cooling rate, we note that the change in kinetic energy of an atom,

$$\frac{\mathrm{d}}{\mathrm{d}t}\left(\frac{1}{2} m_{\mathrm{atom}} v_z^2\right) = v_z m_{\mathrm{atom}} \frac{\mathrm{d}v_z}{\mathrm{d}t} = v_z F_{OM} = -\alpha v_z^2, \tag{2.9}$$

can be used to determine the average cooling power:

$$\left.\frac{\mathrm{d}\langle E \rangle}{\mathrm{d}t}\right|_{\mathrm{cool}} = \frac{\mathrm{d}}{\mathrm{d}t}\left(\frac{1}{2} m_{\mathrm{atom}} \overline{v_z^2}\right) = -\alpha \overline{v_z^2}. \tag{2.10}$$

Eq. (2.10) suggests that atoms that fall into the capture velocity range can be slowed to zero velocity, hence resulting in a absolute zero temperature. This is however not the case, as photon illumination of atoms causes heating. There are two sources of heating during this process: one from the random walk of the atoms as a result of spontaneous emission, and one from the random walk of the atoms as a result of absorption. In the case of spontaneous emission heating, absorption of N photons leads to N spontaneous emissions, and causes a random walk of N steps. Such a random walk results in a mean square displacement of N

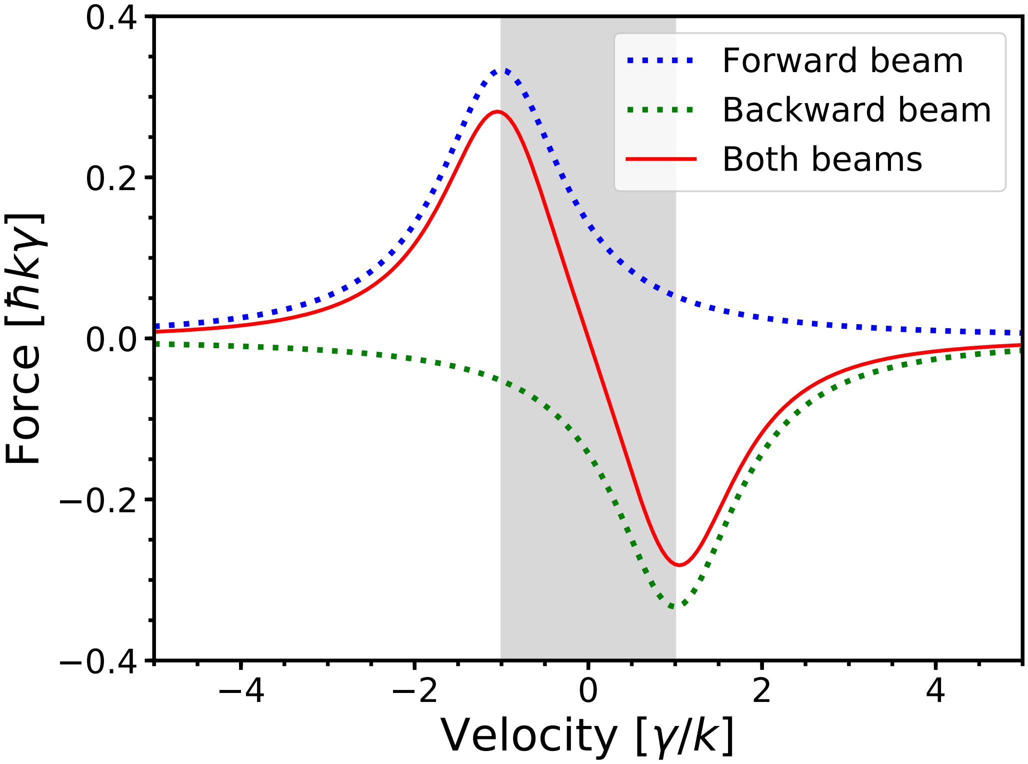

Figure 2.1: Velocity dependent force from two counter-propagating red-detuned laser light beams. The resulting force from the forward and backward beams produces a slowing force approximately proportional to velocity for atoms with a small enough speed, indicated by the gray region.

times the square of the step length. For a given time t the total number of scattered photons satisfies

$$N = \gamma_p t. \tag{2.11}$$

Thus the mean square velocity is increased by

$$\left\langle v_z^2 \right\rangle_{\mathrm{spont}} = \eta v_{\mathrm{r}}^2 \gamma_p t, \tag{2.12}$$

where $r_{\mathrm{r}} = \dfrac{\hbar k}{m}$ is the recoil velocity, $\eta = 1/3$ for 3D isotropic spontaneous emission [35], and the heating rate due to spontaneous emission is

$$\left.\frac{\mathrm{d}\langle E\rangle}{\mathrm{d}t}\right|_{\mathrm{heat,spont}} = \eta m_{\mathrm{atom}} v_{\mathrm{r}}^2 \gamma_p. \tag{2.13}$$

Here a factor of 2 is taken into account because there are 2 counter-propagating beams, giving rise to twice the scattering rate.

On the other hand, during time t an atom does not always absorb the same number of photons. The mean number of cycles of absorption followed by spontaneous emission is also given by Eq. (2.11). The result is another random walk with a mean square velocity increase of

$$\left(\overline{v_z^2}\right)_{\mathrm{abs}} = v_{\mathrm{r}}^2 \gamma_p t. \tag{2.14}$$

Note that Eq. (2.14) does not have a factor η because this random walk is in 1D. The heating rate due to absorption is thus

$$\left.\frac{\mathrm{d}\langle E\rangle}{\mathrm{d}t}\right|_{\mathrm{heat,abs}} = m_{\mathrm{atom}} v_{\mathrm{r}}^2 \gamma_p. \tag{2.15}$$

Now, we extend the system to 3 pairs of counter-propagating beams in x-, y- and z-direction to form a 3D optical molasses. At equilibrium the total cooling rate equals total heating rate, i.e.

$$-\alpha \overline{v_z^2} = 3\eta m_{\mathrm{atom}} v_{\mathrm{r}}^2 \gamma_p + m_{\mathrm{atom}} v_{\mathrm{r}}^2 \gamma_p. \tag{2.16}$$

Note there is a factor 3 in front of the spontaneous heating term but the absorptive heating term is unchanged. This is because we are only considering the velocity spread along z-direction in Eq. (2.13), and to calculate the total heating rate due to spontaneous emission we need to include all directions. Solving for equation Eq. (2.16), we can get

$$k_B T = \frac{\hbar k}{4} \frac{1 + (2\delta/\Gamma)}{(-2\delta/\Gamma)}. \tag{2.17}$$

Since we are trying to determine the minimum temperature we could get via Doppler cooling, we take the derivative with respect to δ for Eq. (2.17) and set it to 0, and note that in the low intensity regime $s_0 \approx 0$, to get

$$\delta = -\Gamma/2. \tag{2.18}$$

The temperature at this detuning is defined to be the Doppler temperature T_D:

$$\boxed{T_D = \frac{\hbar \Gamma}{2k_B}}. \tag{2.19}$$

2.3 Magneto-Optical Trap

Even though the optical molasses technique introduced in Section 2.2 provides a velocity dependent slowing force that laser cools an atomic sample, it does not hold the atoms in space because it does not have a position-dependent restoring force.

By choosing the appropriate laser polarization, and introducing a inhomogeneous magnetic field (for example a quadruple magnetic field with linear magnetic field gradient), a position-dependent confining force can be produced to trap the laser cooled atoms. This setup is known as the magneto-optical trap (MOT), which, since its first demonstrations [80], has become the workhorse in cold atomic physics.

Figure 2.2 shows an arrangement for a type I MOT in 1D. A linear magnetic field gradient induces a Zeeman shift given by

$$\Delta E_{\text{Zeeman}} = \mu_B g_F M_F B_z. \tag{2.20}$$

where μ_B is the Bohr magneton, g_F is the Landé g-factor, $B_z = Az$ is the magnetic field in the z-direction, A is the magnetic field gradient, and M_F is the projection of the angular momentum along B_z. At position $z' > 0$ in the figure, the Zeeman sublevel $M_e = -1$ is shifted closer to resonance with the σ_- polarized red-detuned laser light incident from the right, while the sublevel $M_e = +1$ is shifted further away from resonance for the right beam. The atoms at z' will thus be driven towards the center where $B = 0$. This configuration thus creates a spatially-dependent restoring force. The magnitude of this restoring force can be found by making appropriate changes to the detuning term in Eq. (2.6):

$$\vec{F}_{\pm} = \pm \frac{\hbar \vec{k} \gamma}{2} \frac{s_0}{1 + s_0 + (2\delta_{\pm}/\gamma)^2}, \tag{2.21}$$

where the detunings $\delta_{\pm}$ are modified by

$$\delta_{\pm} = \delta \mp \vec{k} \cdot \vec{v} \pm \mu' B/\hbar, \tag{2.22}$$

where $\vec{v}$ is the velocity vector and $\mu' \equiv (g_e M_e - g_g M_g)\mu_B$ is the effective magnetic moment for the transition. If we assume both the Doppler shift term $\vec{k} \cdot \vec{v}$ and the Zeeman shift term

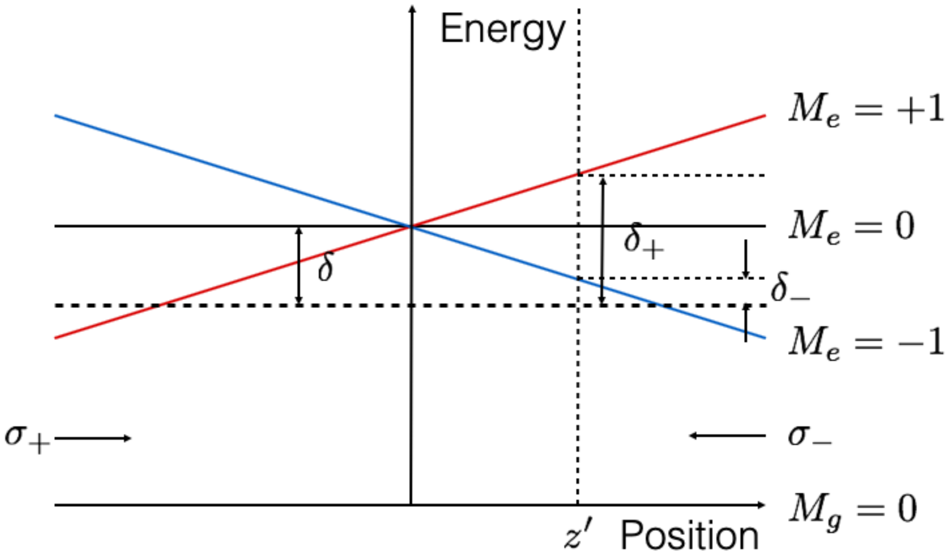

Figure 2.2: Arrangement for a MOT in 1D. For an atom at location z', an energy shift is caused by the presence of the magnetic field. A $\sigma+$ photon original detuned by δ will be shifted further away from resonance, while a $\sigma-$ photon will be shifted closer to resonance. Hence the atom will preferentially absorb a $\sigma-$ photon, and acquire a momentum kick towards the trap center.

$\mu' B/\hbar$ are small compared to the detuning δ, we can write the net MOT force as:

$$\begin{aligned} F_{\mathrm{MOT}} &= |\vec{F}_+ + \vec{F}_-| = \frac{\hbar k \gamma s_0}{2}\left[\frac{1}{1+s_0+(2\delta_+/\gamma)^2} - \frac{1}{1+s_0+(2\delta_-/\gamma)^2}\right] \\ &\approx \frac{\hbar k \gamma s_0}{2[1+s_0+(2\delta/\gamma)^2]^2}\left((2\delta_-/\gamma)^2 - (2\delta_+/\gamma)^2\right) \\ &= \frac{\hbar k \gamma s_0}{2[1+s_0+(2\delta/\gamma)^2]^2}\frac{-16\delta\left(kv - \mu' B/\hbar\right)}{\gamma^2} \\ &= -\alpha v - \kappa z, \end{aligned} \tag{2.23}$$

where α is defined in Eq. (2.8), and κ is the spring constant

$$\kappa = \frac{\mu' A}{\hbar k}\alpha. \tag{2.24}$$

Eq. (2.23) is the equation of a 1D damped harmonic oscillator. The damping rate is

$$\Gamma_{\mathrm{MOT}} = \frac{\alpha}{m_{\mathrm{atom}}} \tag{2.25}$$

and oscillation frequency is

$$\omega_{\mathrm{MOT}} = \sqrt{\frac{\kappa}{m_{\mathrm{atom}}}}. \tag{2.26}$$

2.3.1 Measuring MOT Temperature

We can start by assuming a Gaussian-distributed atomic sample that follows Maxwell-Boltzmann statistics. Then the probability of finding a given atom along a single dimension at time t, $P(x,t)$ (along x-direction), evolves according to an average over the initial ballistic velocity distribution $\langle P(x \to x + v_x t)\rangle_{v_x}$ at temperature T

$$P(x,t) \propto \int dv_x \exp\left(-\frac{1}{2}\left(\frac{x+v_x t}{\omega_0}\right)^2\right) \exp\left(-\frac{m v_x^2}{2k_\mathrm{B}T}\right), \tag{2.27}$$

$$P(x,t) \propto \exp\left(-\frac{x^2}{2\omega_0^2 + \frac{2k_\mathrm{B}Tt^2}{m}}\right) \tag{2.28}$$

where ω_0 is the $\frac{1}{e}$ MOT extant at $t = 0$. The spatial width as a function of time, is

$$\omega(t) = \sqrt{\omega_0^2 + \frac{k_\mathrm{B}Tt^2}{m}}. \tag{2.29}$$

Therefore, the temperature of a MOT can be determined by setting the MOT into free expansion and measuring the spatial extant of the atomic cloud as a function of time. In the experiments we describe in this chapter and the following chapter, we perform a series of MOT free expansions and measure the MOT spatial extants as a function of time with absorptive imaging, then use Eq. (2.29) to determine the temperature of the MOT.

2.4 Optical Frequency Comb Two-Photon Cooling and Trapping

In this section, we extend the theory we have developed in the previous two sections to a two-photon transition driven by an optical frequency comb.

2.4.1 Scattering rate from a frequency comb

Scattering rate from a frequency comb on a two-photon transition is needed to determine the theoretical two-photon Doppler limit. As shown in Figure 2.3(c), the frequency associated with the n^{th} comb tooth can be written as

$$f_n = n f_{\text{r}} + 2 f_0, \tag{2.30}$$

where f_0 is the carrier envelope offset frequency of the optical frequency comb, and $f_{\text{r}} \equiv 1/T_{\text{r}}$ is the pulse repetition rate. For a transform-limited ML laser, we can model the effective (time-averaged) resonant Rabi frequency of the n^{th} tooth of this two-photon comb as

$$\Omega_n = \sum_p \frac{g_p^{(1)} g_{n-p}^{(2)}}{2\Delta_p} \tag{2.31}$$

where $g_p^{(1)}$ is the resonant single-photon Rabi frequency for excitation from the ground $|\text{g}\rangle$ to the intermediate state $|\text{i}\rangle$ due to the p^{th} optical comb tooth and $g_p^{(2)}$ is the same quantity for excitation from the intermediate state $|\text{i}\rangle$ to the excited state $|\text{e}\rangle$ (Fig. 2.3**a**,**b**). In comparison, when the pulse is chirped, different frequency components arrive at different times and hence are not in phase, resulting in destructive interference. Mathematically, g_p is complex and the phase of the product $g_p^{(1)} g_{n-p}^{(2)}$ becomes a function of p, reducing the magnitude of Ω_n. The single-photon detuning from the intermediate state is $\Delta_p = p f_{\text{r}} + f_0 - \Delta E_{\text{gi}}/h$ where ΔE_{gi} is the energy difference between the ground state and the intermediate state. We also denote by N the index of the two-photon comb tooth closest to resonance (associated with the optical sum frequency $f_N = N f_{\text{r}} + 2 f_0$). If the pulse duration T_{p} is short compared to the excited state's lifetime $\tau \equiv 1/\gamma$ ($T_{\text{p}} \ll \tau$), the resonant Rabi frequency of each two-photon comb tooth can be approximated by Ω_N.

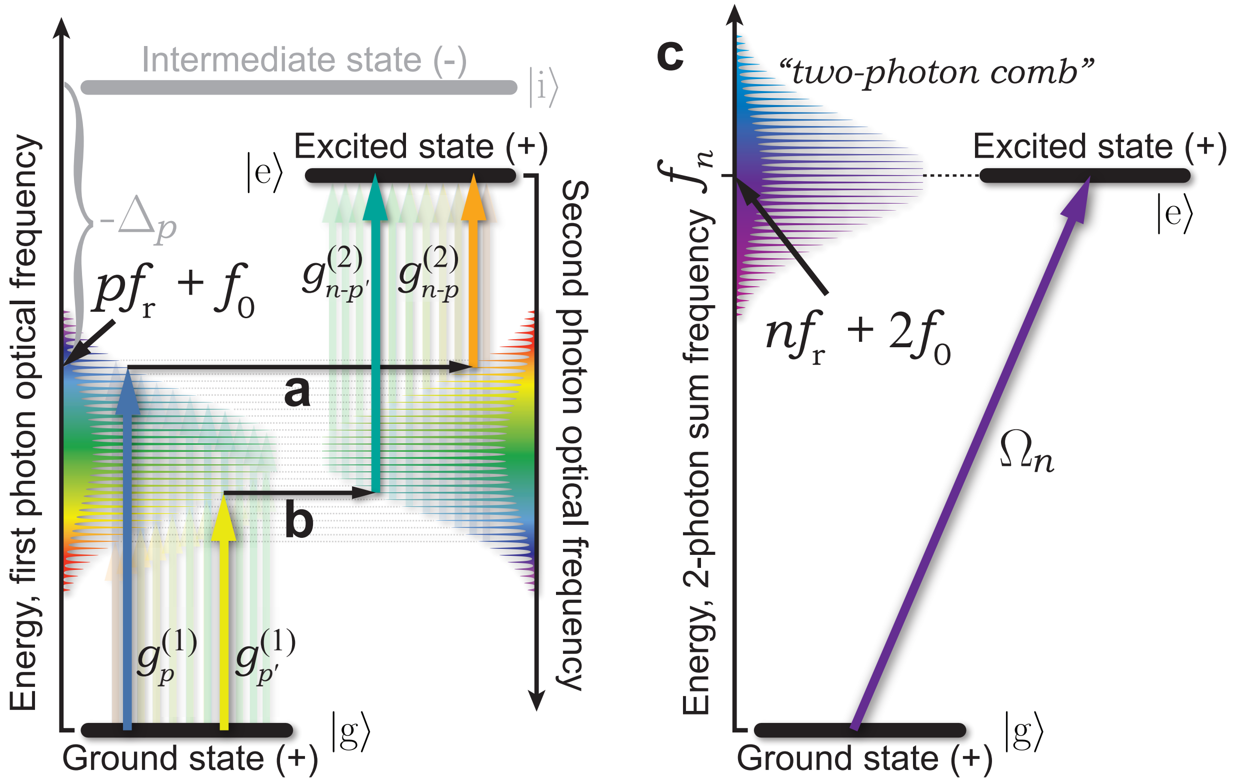

Figure 2.3: Constructive interference of multiple paths in a two-photon transition driven by a transform-limited optical frequency comb. All pairs of comb teeth whose sum frequency matches the excited state energy interfere constructively to excite atoms. Two example pairs are shown as **a** and **b**, and the effective two-level system that results from the sum is shown in **c**. Every tooth of the resulting "two-photon comb" of resonant coupling strength Ω leverages the full power of all of the optical frequency comb teeth through this massively-parallel constructive interference.

We define the resonant saturation parameter of the n^{th} comb tooth of the two-photon comb (shown in Figure 2.3(c)) to be

$$s_n \equiv 2\Omega_n^2/\Gamma^2, \tag{2.32}$$

where Γ is the decay rate of the excited state, which we will model as decaying only to the ground state, and Ω_n is the coupling strength between the ground and excited state from the n^{th} comb tooth in the two-photon comb. We consider $s_n \ll 1$ and $\Omega_n T_{\text{r}} \ll \pi$, which is typically true due to the low Rabi frequency under realistic experimental conditions.

Experimentally we are interested in time-averaged instead of instantaneous behavior of the optical force, thus we sum up the scattering rates due to each comb tooth instead of the excitation amplitudes. The steady-state time-averaged scattering rate from the n^{th} comb tooth by a stationary atom will then be given by

$$\gamma_n \approx \Gamma \frac{s_n}{2} \frac{1}{1+(2\delta_n/\gamma)^2} \tag{2.33}$$

where $f_{\text{ge}} \equiv \Delta E_{\text{ge}}/h$ is the two-photon resonance frequency, ΔE_{ge} is the energy difference between the ground and excited state, and $\delta_n \equiv 2\pi(f_n - f_{\text{ge}})$ is the detuning of the n^{th} comb tooth of the two-photon comb from the two-photon resonance. For a two-photon comb whose center frequency is near f_{ge}, we can approximate $s_n \approx s_N$, where N is the index of the comb tooth closest to resonance, because s_n will not change much over the range of n that is within a few Γ of resonance. We can then use the identity

$$\sum_{n=-\infty}^{\infty} \frac{1}{1+a^2(n-b)^2} = \frac{\pi}{a} \frac{\sinh(2\pi/a)}{\cosh(2\pi/a) - \cos(2\pi b)} \tag{2.34}$$

to write

$$\gamma_{\text{comb}} = \sum_n \gamma_n = \Gamma \frac{s_N}{2} \frac{(\Gamma T_{\text{r}}/4)\sinh(\Gamma T_{\text{r}}/2)}{\cosh(\Gamma T_{\text{r}}/2) - \cos(\delta_N T_{\text{r}})}. \tag{2.35}$$

In the limit where both $\delta_N/2\pi$ and $\Gamma/2\pi$ are small compared to the repetition rate f_{r}, Eq. (2.35) reduces to Eq. (2.33) with $\gamma_{\text{comb}} \approx \gamma_N$. For the laser cooling and trapping with rubidium we report in this chapter, the combined effect of all of the off-resonant comb teeth to the scattering rate when $\delta_N = -\Gamma/2$ is approximately $10^{-4}\gamma_N$, and we can neglect their presence for slow-moving atoms.

2.4.2 Doppler Limit for Two-Photon Optical Molasses

To derive the Doppler cooling limit for (approximately equal frequency) two-photon transitions, assume that the two-photon transitions are driven well below saturation (resonant saturation parameter $s_N \ll 1$) and with a two-photon detuning of $\Gamma/2$ to the red side of resonance. In the case of cooling with an optical frequency comb, we will assume that the single-tooth approximation discussed in Section 2.4.1 is valid.

The average cooling force can be obtained by replacing α in Eq. (2.7) by α_N, where

$$\alpha_N = -\frac{8\hbar(2k)^2\delta s_N}{\Gamma(1+s_N+(2\delta_N/\Gamma)^2)^2}, \tag{2.36}$$

note that the wavenumber k in Eq. (2.7) is replaced by $2k$, where $k = \frac{1}{2}\frac{\omega_{\text{ge}}}{c}$, to account for the fact that it takes 2 photons to complete the transition. Hence at $\delta_N = \Gamma/2$, and in the limit where the Doppler shifts are small compared to the excited state linewidth, the cooling rate equation Eq. (2.10) becomes

$$\left.\frac{\mathrm{d}\langle E\rangle}{\mathrm{d}t}\right|_{\text{cool}} = -\alpha_N\overline{v_z^2} = -\frac{\alpha_N k_B T}{m_{\text{atom}}} \approx -\frac{4\hbar k^2 s_N k_B T}{m_{\text{atom}}}. \tag{2.37}$$

Similar to Section 2.2, this cooling power is balanced by two sources of heating: heating due to randomly-distributed momentum kicks from absorption events and heating due to momentum kicks from spontaneous emission. For the former, there are only contributions from the single-beam processes since two-beam absorption does not induce a momentum kick for counter-propagating beams, and the heating power from absorption is in the same form as Eq. (2.15):

$$\left.\frac{\mathrm{d}\langle E\rangle}{\mathrm{d}t}\right|_{\text{heat,abs}} = m_{\text{atom}}v_{\text{r}}^2\gamma_N = \frac{s_N\Gamma\hbar^2(2k)^2}{4m_{\text{atom}}} = \frac{s_N\Gamma\hbar^2k^2}{m_{\text{atom}}}. \tag{2.38}$$

The second heating term is due to spontaneous emission and will depend upon the details of the decay channels available to the excited state. If the probability that an excited atom emits a photon with frequency ω_i at some point on its way to the ground state is $\mathcal{P}_i$, the heating from these decays can be modeled with a probability-weighted sum of the squares of the momentum kicks from these spontaneously-emitted photons, *viz.*

$$\left.\frac{\mathrm{d}\langle E\rangle}{\mathrm{d}t}\right|_{\text{heat,spon.}} = \frac{1}{2m}\gamma_{\text{tot}}\sum_i \mathcal{P}_i\left(\hbar\frac{\omega_i}{c}\right)^2 \tag{2.39}$$

where γ_{tot} is the total excitation rate (see *e.g.* Eq. (2.35) for the case with a single beam from an optical frequency comb) and we are for the moment modeling the spontaneous emission as being confined to 1D, which gives a Doppler limit that agrees with the 3D calculation in the standard single-photon case.

Eq. (2.39) shows the mechanism by which multi-photon cooling can give rise to a lower Doppler limit than single-photon cooling; by splitting the decay into smaller, uncorrelated momentum kicks, the mean square total momentum transfer (and therefore the heating) will on average be lower than for a single photon decay channel. Eq. (2.39) also shows that there is an additional heating mechanism for the CW case since γ_{tot} will in this circumstance include two-beam excitations that are Doppler free for counter-propagating beams [101]. The excitation rate from the two-beam terms (which does not contribute to the cooling in 1D) is 4 times larger than each single-beam term, and the size of this effect for 1D two-photon laser cooling of atomic hydrogen on a quenched $1S{\to}2S$ transition, for example, would lead to a comb-cooled Doppler temperature that is a factor of 2 lower than the predicted CW limit [101]. In order to make a quantitative estimate of the magnitude of these effects, we model the decay cascade as proceeding via a single intermediate state halfway between $|\mathrm{g}\rangle$ and $|\mathrm{e}\rangle$ ($\mathcal{P}_i = 1$ and $\omega_i = \omega_{\text{ge}}/2$ for $i = 1, 2$), which gives us

$$\left.\frac{\mathrm{d}\langle E\rangle}{\mathrm{d}t}\right|_{\text{heat,spon.}} = \frac{1}{2m}\gamma_{\text{tot}}\sum_i \mathcal{P}_i\left(\hbar\frac{\omega_i}{c}\right)^2 = \frac{1}{2m}\gamma_{\text{tot}}\cdot 2(\hbar k)^2 = \frac{\hbar^2k^2}{m_{\text{atom}}}\gamma_{\text{tot}}. \tag{2.40}$$

For the CW case there are 3 possible ways to contribute to γ_{tot}: both photons coming from the left beam, the right beam, or one photon coming from each beam. When both photons come from one beam,

$$\gamma_{\text{one-beam}} = \frac{s_N\Gamma/2}{1+s_N+(2\delta_N/\Gamma)^2} \approx \frac{s_N\Gamma}{4}, \tag{2.41}$$

while for the one-from-each-beam situation the scattering rate is 4 times that of the one-beam situation:$\gamma_{\text{two-beams}} = 4\gamma_{\text{one-beam}}$, since scattering rate $\propto$ intensity^2. Then

$$\gamma_{\text{tot,CW}} = 2\gamma_{\text{one-beam}} + \gamma_{\text{two-beams}} = \frac{3}{2}s_N\Gamma, \tag{2.42}$$

and the corresponding CW heating rate from spontaneous emission is

$$\left.\frac{\mathrm{d}\langle E\rangle}{\mathrm{d}t}\right|_{\text{heat,spon.,CW}} = \frac{3s_N\Gamma\hbar^2k^2}{2m_{\text{atom}}}. \tag{2.43}$$

For the ML case, γ_{tot} only contains 2 terms because in general the two counter-propagating beams do not overlap at the location of the atoms. Only the two one-beam scattering rates contribute, and the total scattering rate for the ML case is

$$\gamma_{\text{tot,ML}} = 2\gamma_{\text{one-beam}} = \frac{s_N\Gamma}{2}. \tag{2.44}$$

The ML heating rate from spontaneous emission is

$$\left.\frac{\mathrm{d}\langle E\rangle}{\mathrm{d}t}\right|_{\text{heat,spon.,ML}} = \frac{s_N\Gamma\hbar^2k^2}{2m_{\text{atom}}}, \tag{2.45}$$

a factor of 3 lower than its CW counterpart due to the absence of Doppler free absorption.

The equilibrium temperature can be solved by setting the cooling and heating terms sum to zero.

$$\left.\frac{\mathrm{d}\langle E\rangle}{\mathrm{d}t}\right|_{\text{cool}} + \left.\frac{\mathrm{d}\langle E\rangle}{\mathrm{d}t}\right|_{\text{heat,abs}} + \left.\frac{\mathrm{d}\langle E\rangle}{\mathrm{d}t}\right|_{\text{heat,spon.}} = 0. \tag{2.46}$$

For the CW case, the Doppler limit for two-photon 1D optical molasses with counter-propagating CW laser beams is given by

$$-\frac{4\hbar k^2 s_N k_B T}{m_{\text{atom}}} + \frac{s_N\Gamma\hbar^2k^2}{m_{\text{atom}}} + \frac{3s_N\Gamma\hbar^2k^2}{2m_{\text{atom}}} = 0, \tag{2.47}$$

$$T_{\text{D,CW}} = \frac{5}{4}\frac{\Gamma\hbar}{2k_{\text{B}}}. \tag{2.48}$$

This is 25% hotter than single-photon cooling on a transition with the same linewidth, despite the fact that it includes the reduction in heating from the cascade decay.

For the ML case, in a similar fashion we can find

$$T_{\text{D,ML}} = \frac{3}{4}\frac{\Gamma\hbar}{2k_{\text{B}}}, \tag{2.49}$$

which is colder than both the CW and the single-photon cases.

2.5 Experiment Results

We report first experimental test of direct frequency comb two-photon cooling and trapping in this section. We demonstrate the technique using rubidium atoms. We drive the $5^2S_{1/2} \rightarrow 5^2D_{5/2}$ transition in rubidium on a two-photon transition at 778 nm for both cooling and trapping. For the experiment described in this chapter, we operate a Tsunami Ti:Sapphire laser that emits 2–5 ps pulses (less than 500 GHz bandwidth) at 778 nm at a repetition rate of $f_{\mathrm{r}} = 81.14$ MHz.

2.5.1 Laser Tooth Linewidth Modification

For the $5^2S_{1/2}\rightarrow 5^2D_{5/2}$ transition in rubidium (Figure 2.4), the natural decay rate of the excited state is $\Gamma/2\pi = 667$ kHz [87]. Eq. (2.49) gives a Doppler cooling limit of 12 μK, which will also be true in 3D for a ML laser with non-colliding pulses. The transition linewidth, however, is broadened by Doppler effects of moving atoms, as well as the laser linewidth. To sensibly determine a theoretical Doppler temperature, we therefore attempt to quantify an effective transition linewidth that accounts for both these effects.

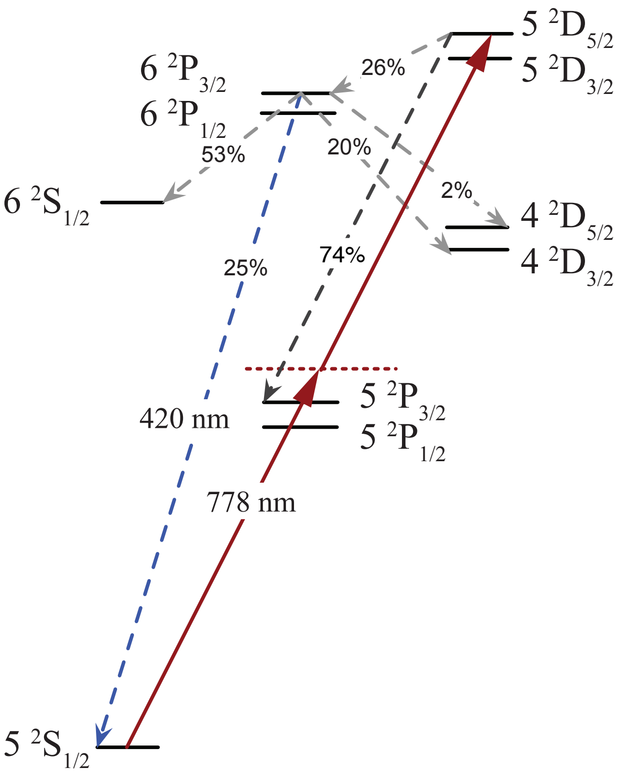

Figure 2.4: Relevant levels of ^{85}Rb for two-photon laser cooling and trapping. A two-photon transition from $5\ ^2S_{1/2} \rightarrow 5\ ^2D_{5/2}$ state is performed with two 778 nm photons for laser cooling and trapping. The excited Rb atom then decays to the $6\ ^2P_{3/2}$ state 26% of the time, which then decays back to the ground state 25% of the time. The $6\ ^2P_{3/2} \rightarrow 5\ ^2S_{1/2}$ transition is a blue transition at 420 nm, and hence a background-free fluorescence detection at 420 nm can be readily performed for characterization of transition linewidth.

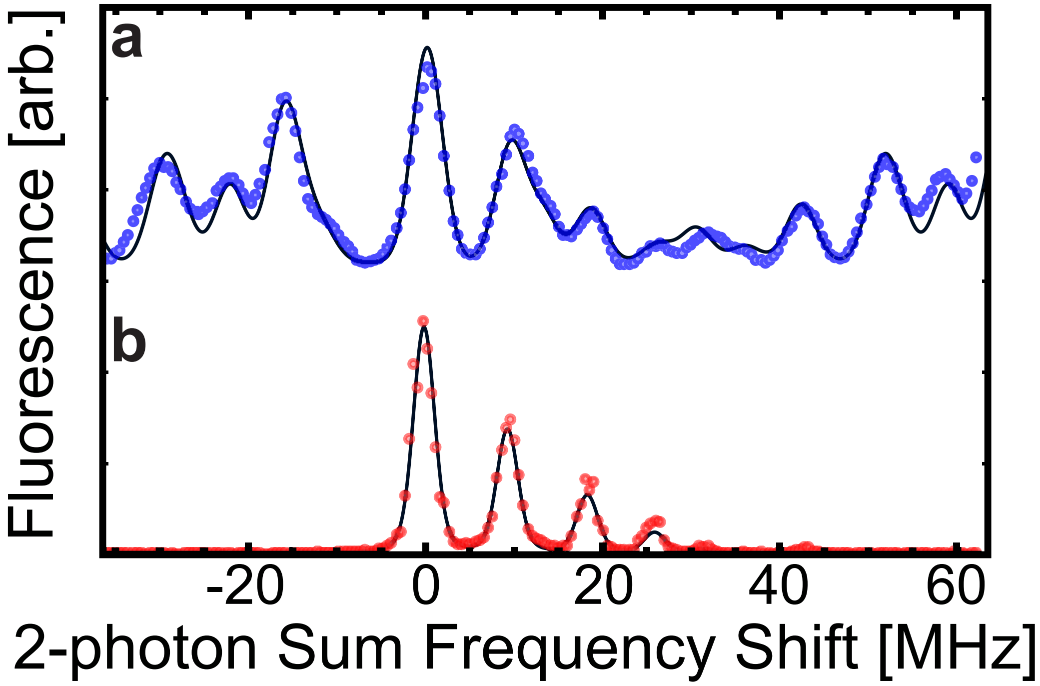

Figure 2.5: Laser-induced fluorescence spectrum of the $5S \rightarrow 5D$ two-photon transition driven by an optical frequency comb. **a**: Spectrum from a natural abundance vapor cell and **b**: a ^{85}Rb CW MOT. Solid curves are theory fitted for **a** Gaussian and **b** Voigt line shapes. These spectra repeat with a period of $f_\mathrm{r} = 81.14$ MHz on the horizontal axis.

By monitoring the 420 nm fluorescence from a hot vapor cell (Fig. 2.5**a**), a continuously-operating CW MOT (Fig. 2.5**b**), and the pre-cooled (and then released) rubidium atoms as the ML laser frequency is swept (shown at the top of Fig. 2.9), we obtain a line shape that is more broad than the natural linewidth of $\Gamma/2\pi = 667$ kHz [87]. For the latter, the Doppler broadening expected from motion would be 630 kHz if taken alone, and the magnetic field is zeroed to a level where magnetic broadening will not contribute to the spectral width. We find that, after taking into account the natural linewidth and the expected Doppler broadening, we have a residual FWHM of the two-photon spectrum of around 1.8 MHz, which we attribute to the laser. It is worth noting that using this width to infer an optical (that is, single-photon) comb tooth width or vice versa is highly dependent on the details of the broadening mechanism (see, *e.g.* [84]), and we therefore rely on the two-photon spectroscopy exclusively for determining our relevant effective two-photon spectral linewidth, which is model-independent. Combining this with the natural linewidth again via convolution gives us an effective two-photon spectral linewidth with a FWHM of $\gamma_{\text{eff}}/2\pi = 2.2$ MHz.

To account for the effect of finite two-photon spectral linewidth on scattering rate, we approximate the line shape as Lorentzian to adopt the model of Haslwanter *et al.* [43], which in the low-intensity limit ($s_N \ll 1$) gives the scattering rate

$$\gamma_N = \frac{\Omega_N^2}{\Gamma} \frac{\Gamma/\Gamma_{\text{eff}}}{1 + \left(2\delta_N/\Gamma_{\text{eff}}\right)^2}. \tag{2.50}$$

We can recognize this as Eq. (2.33) with the replacement

$$\Gamma \rightarrow \Gamma_{\text{eff}}, \quad n \rightarrow N, \tag{2.51}$$

and conclude that a first approximation of the Doppler temperature limit can be made in the case of finite spectral linewidth by applying the replacement Eq. (2.51) to expressions for the Doppler temperature (*e.g.* Eq. (2.49)). Using this approach for our experimental case where cooling is applied in 1D but spontaneous emission is approximated as being isotropic in 3D, we predict a Doppler limit of $T_{\text{D,comb}} = 31\ \mu$K.

The blue fluorescence from the 420 nm $6\ ^2P_{3/2} \rightarrow 5\ ^2S_{1/2}$ transition photons can readily be observed by shining a pair of counter-propagating ML laser whose nearest comb tooth is slightly red-detuned. Figure 2.6 shows a MOT fluorescing 420 nm photons. The image is taken with an Andor iXon EMCCD camera with a blue filter.

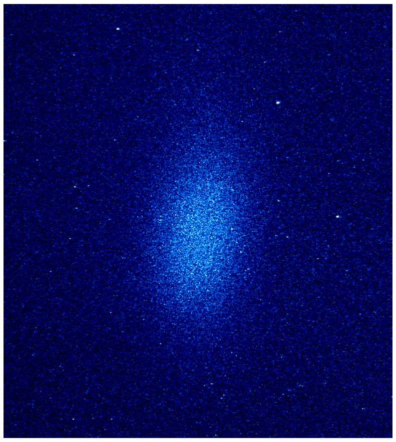

Figure 2.6: Blue fluorescing MOT induced by the $5S \rightarrow 5D$ two-photon transition driven by an optical frequency comb.

2.5.2 Optical Frequency Comb Two-Photon Laser Cooling

To demonstrate optical frequency comb two-photon laser cooling, we prepare an initial sample of $\approx 10^7$ ^{85}Rb atoms using a standard CW laser MOT at 780 nm. We then turn off the magnetic field and the CW laser cooling light. The atoms are at a temperature typically near 110 μK at this stage. The temperature is determined by using method described in Section 2.3.1. A weak CW "repump" laser is left on continuously to optically pump atoms out of the $F_\mathrm{g} = 2$ ground state, and has no measurable direct mechanical effect. Each ML beam typically has a time-averaged power of (500 ± 50) mW and a $1/e^2$ intensity diameter of(1.1 ± 0.1) mm. After illumination by the ML laser, the atoms are allowed to freely expand and are subsequently imaged using resonant CW absorption to determine their position and velocity distributions.

We measure the resonant excitation rate by monitoring momentum transfer from a single ML beam. As illustrated in Figure 2.7, the amount of momentum transfers to the atoms by a single ML laser beam from **b** right and **c** left after 2 ms of resonant ML laser illumination can be found by comparing the change in center of mass from the unilluminated position in **a**. We infer a resonant excitation rate to be $\gamma_\mathrm{scatt} = (6500 \pm 700)$ s^{-1}. Our transform-limited theoretical estimate from Eq. (2.31) and our laser parameters gives (13000 ± 2000) s^{-1}. Since the two-photon Rabi frequency is inversely proportional to the pulse time-bandwidth product [82], this suggests that there is residual chirp that is increasing the time-bandwidth product by a factor of $\approx \sqrt{2}$. The measured rate is well above the threshold needed to support these atoms against gravity (≈ 810 s^{-1}), which suggests that 3D trapping should be possible with additional laser power for the inclusion of four more beams.

We observe Doppler cooling and its dependence on two-photon detuning by applying counter-propagating linearly-polarized ML beams to the atom cloud for 4 ms in zero magnetic field. An illustration of the resultant laser-cooled atomic cloud is shown in Figure 2.7**d**. Because of the inhomogeneity of the ML laser intensity profile, different regions of the MOT experience different scattering rate, as demonstrated in Figure 2.7**b** and **c**. Therefore we measure the spatial spread of the MOT for a selected region, indicated by the red dashed

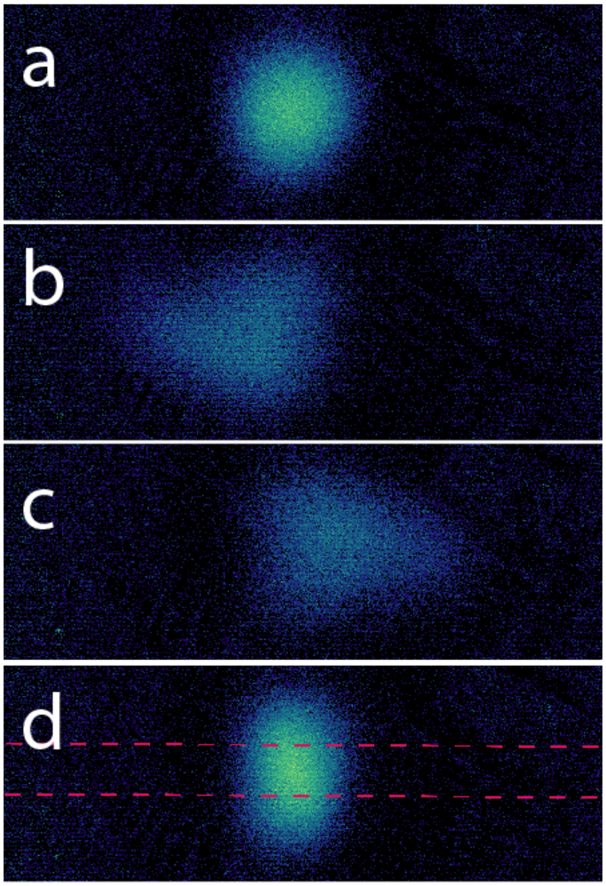

Figure 2.7: Absorption images of the atom cloud after free expansion following **a**: no ML illumination, **b**: ML illumination from the right, **c**: left and **d**: both directions, detuned to the red of resonance. Mechanical forces are evident in **b** and **c**, and the narrowing of the velocity distribution in the horizontal direction in **d** is the hallmark of cooling. The region bounded by red dashed lines indicates where the spatial spread of the MOT is measured from.

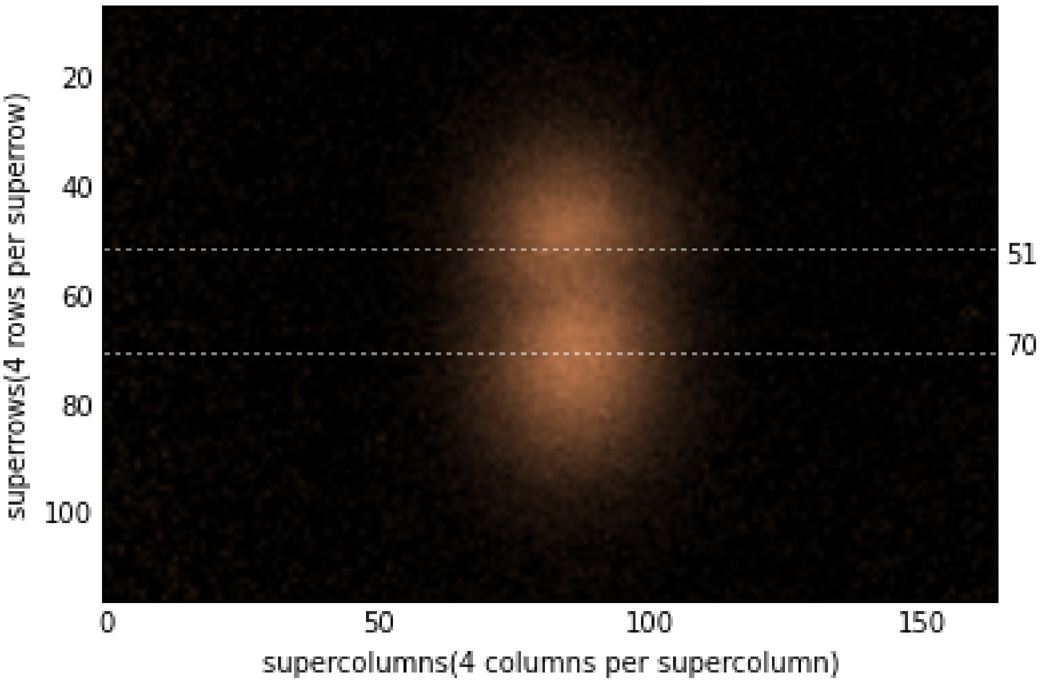

Figure 2.8: Sample absorption image of a laser-cooled atomic cloud. The image is a "mosaic"-ed image, where averaging is performed over 4 × 4 tiles on an original 656 × 492 image to obtained an errorbar associated with each "superpixel". Due to the small radius of the ML laser beam, the width of the atom's spatial distribution is performed for a selected region, shown as the region between the white dotted lines. Note that gravity needs to be taken into account for different expansion times when finding the correct selected region.

boundaries in 2.7**d**.

By fitting the spatial distribution of the atoms in the selected region at different expansion times (See Figure 2.8), we extract a 1D temperature, shown in the bottom of Fig. 2.9. The solid curve is based on the algebraic model developed in Section 2.4 to derive the Doppler limit and is fit for a resonant single-beam excitation rate of $(4800 \pm 400)\ \mathrm{s}^{-1}$ and linewidth $\gamma_{\mathrm{eff}}/2\pi = (1.88 \pm 0.07)$ MHz (see Section 2.5.1), consistent with the single-beam recoil measurements and laser power fluctuations discussed above. We realize a minimum temperature of $(57 \pm 2)\ \mu$K (Fig. 2.10).

It should be noted the atoms are in a molasses during the ML laser illumination. The cooling force from the ML molasses is a damping force that introduces extra dynamics, which is not captured by the simple model of Eq. (2.29). We therefore developed a Monte Carlo simulation to model an expanding cloud of atoms (in three dimensions) that is subject to the optical forces of counterpropogating laser beams in one dimension. The data points marked "Constrained" in Figure 2.9 and Figure 2.10 are derived from analysis that relies on our simulation. For each temperature data point we simulate experiment parameters (detuning, initial sample temperature, initial sample width, ML cooling duration, etc.) along with the experimental measured widths of our atomic cloud during free expansion. We run the simulation multiple times as a function of scattering rate and select the simulation that minimizes χ^2 between the experimentally measured widths and the simulation widths. From the best simulation we define a temperature using $T \equiv \frac{m}{k_\mathrm{B}}\sigma_v^2$ where σ_v is the standard deviation of the simulation's velocity distribution. Despite the fact that the free expansion model does not include effects of the ML laser, the two methods give almost the same temperatures, which can be seen by comparing the blue and gray points in Fig. 2.9 in the main text and the black and red points in the inset of that figure. There seems to be a slightly higher inferred temperature when the Monte Carlo assisted analysis ("Constrained") is used in cases where the acceleration from the ML laser is large.

We also note that the reduced temperature is hotter than the expected Doppler limit of 31 μK for our system (see Eq. 2.49). We find experimentally that the temperature inferred from free-expansion imaging is highly sensitive to beam alignment, and therefore suspect the discrepancy is due to imperfect balancing of the forward and backward scattering forces at some locations in the sample [68]. We calculate that the scattering rate due to single-photon excitation on $5S \to 5P$ under these far-detuned conditions is of order ≈ 1 s^{-1}, which would contribute a negligible amount of force in 4 ms. The absence of observable single-photon processes from possible near-resonant optical comb teeth is further evident in the period of the frequency dependence of Fig. 2.5**a**, **b** and Fig. 2.9, which repeat every f_r (as opposed to $2f_\mathrm{r}$, which would be expected for resonant single-photon processes [70]).

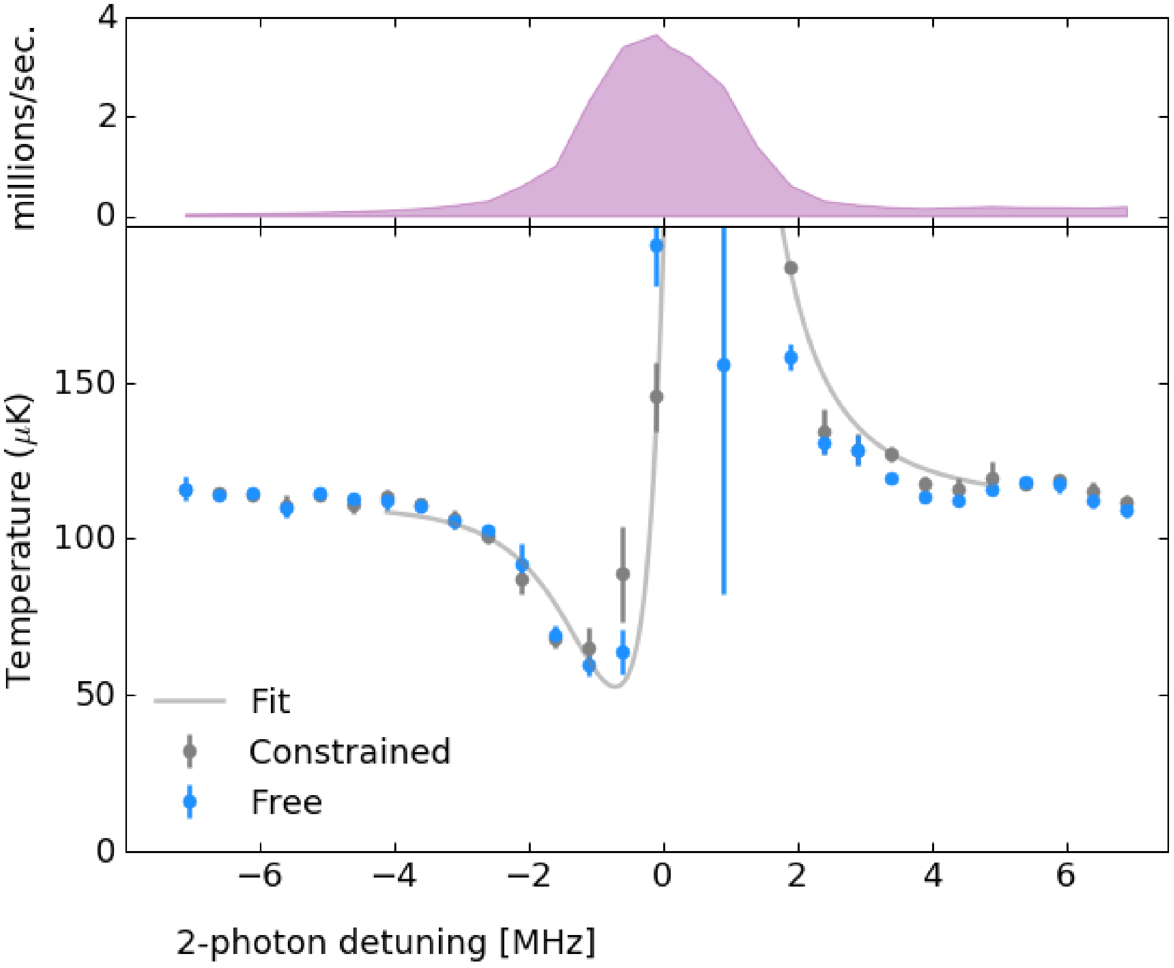

Figure 2.9: Detuning dependence of 420 nm fluorescence (top) and the resulting temperature (bottom) of rubidium atoms laser-cooled by an optical frequency comb on a two-photon transition. The solid curve is fit for scattering rate, effective linewidth and detuning offset of data analyzed with the aid of a Monte Carlo technique (data labeled "Constrained"). The same data are also analyzed using a free expansion model ("Free"), and agree well with the Monte Carlo assisted analysis.

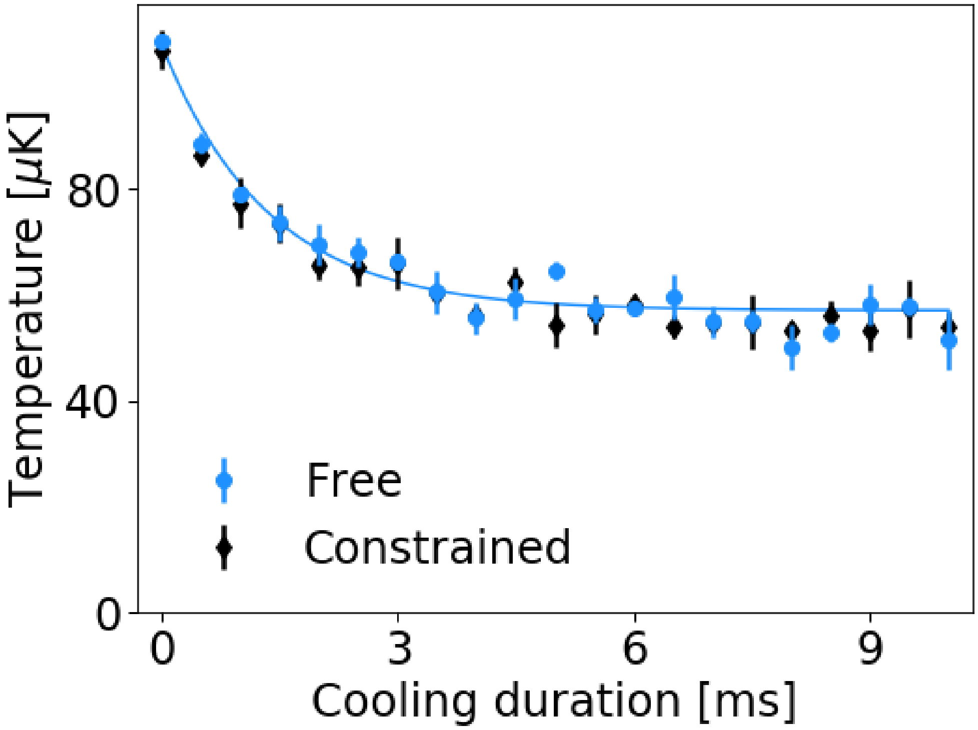

Figure 2.10: Temperature v.s. time when the laser detuning is optimized for cooling, giving a minimum temperature of (57 ± 2) μK. The time decay of the 420 nm fluorescence shows that atoms leave the interaction region due to transverse motion in (4.0 ± 0.3) ms (see Figure 2.11), but steady-state 1D temperature is reached in $\tau = (1.28 \pm 0.09)$ ms. Error bars are statistical over repeated measurements, and do not include the systematic effect of beam mode mismatch, discussed below.

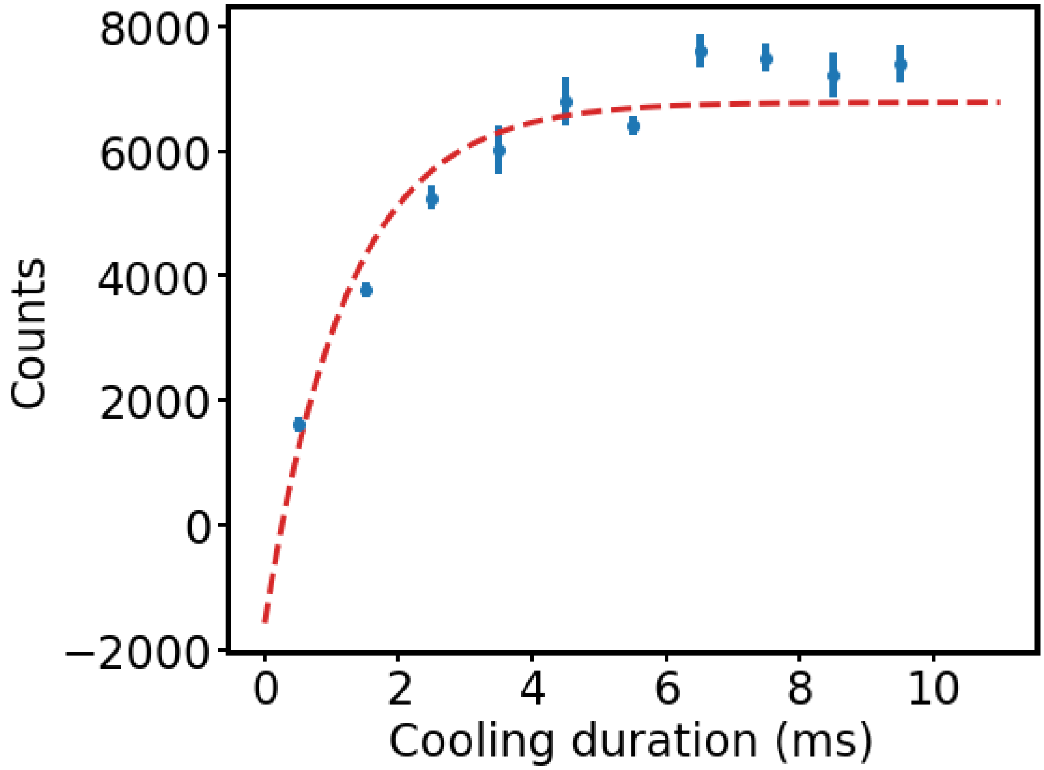

Figure 2.11: Time decay of the 420 nm fluorescence. Blue data points are the PMT counts collected during cooling as a function of cooling duration. Red dashed curve is a fit to the integral of the exponential decay function, with a decay constant 1.24 ms. This means that ≈ 95% of the atoms leave the interaction region in 4.0 ms.

2.5.3 Optical Frequency Comb Two-Photon MOT

To investigate the feasibility of using this technique to make a MOT, a quadrupole magnetic field with a gradient of 7.7 G/cm is introduced and the ML beam polarizations are set to drive $\sigma^{\pm}$ transitions in the standard single-photon CW MOT configuration [80] to make a 1D MOT. We displace the atom cloud from the trap center and monitor the atoms as they are pushed toward the trap center, as shown in Figure 2.12. The corresponding phase space plot is shown in Figure 2.13. The system is modeled as a damped harmonic oscillator and fitting the motion of the atoms yields a trapping frequency of $\nu_{\mathrm{MOT}} = (40 \pm 9)$ Hz and a cyclic damping rate of (37 ± 4) Hz. These MOT parameters imply a resonant excitation rate of $(7000 \pm 1000)\ \mathrm{s}^{-1}$ and an effective magnetic line shift of $(0.5 \pm 0.2)\ \mu_{\mathrm{B}}$ (see Section 2.3). The average of the calculated line shifts for all $\Delta m_F = +2$ $(\sigma^+\sigma^+)$ transitions would be 1.2 μ_{B} for $F_{\mathrm{g}} = 3 \rightarrow F_{\mathrm{e}} = 5$. By measuring the polarization of the beam before and after the vacuum chamber for each pass, we infer that the fraction of the laser power with the nominally desired polarization at the location of the atoms is 97% for the forward beam and 87% for the retro-reflected beam. In a simple 1D model with magnetic field (quantization axis) parallel to the light's $\hat{\boldsymbol{k}}$-vector, $\sigma^+\sigma^+$, $\sigma^-\sigma^-$, $\sigma^+\sigma^-$, and $\sigma^-\sigma^+$ transitions can be driven. Including the average line shifts from all of the $\Delta m = 0$ (from $\sigma^+\sigma^-$ and $\sigma^-\sigma^+$ transitions) and $\Delta m = -2$ transitions (from $\sigma^-\sigma^-$) weighted by our polarization measurements yields an effective magnetic line shift of 0.68 μ_{B}. During the ≈ 4 milliseconds of ML illumination before the atoms' transverse motion causes them to exit the interaction volume, we do not detect any atom loss due to photoionization, consistent with the measured photoionization cross section [33].

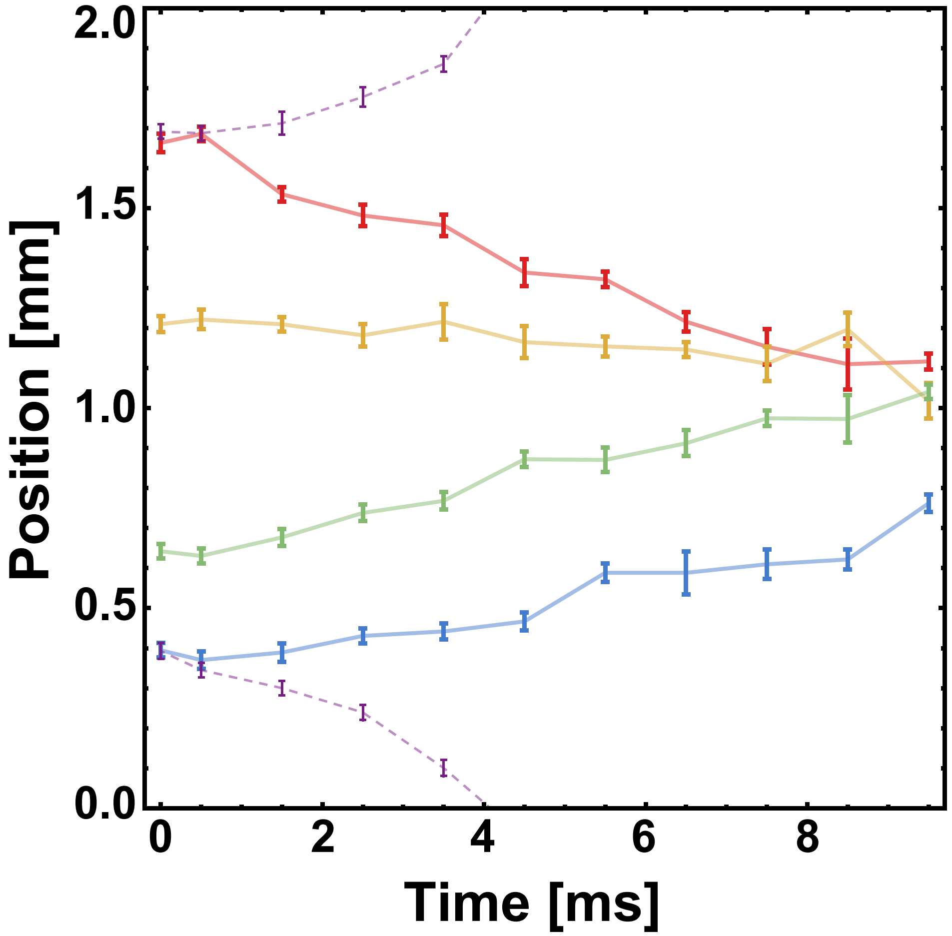

Figure 2.12: Position space trajectories for atoms trapped in a two-photon, optical frequency comb MOT. The MOT is first displaced from the trap center by applying a bias magnetic field to the CW MOT. We then release the MOT by turning off the CW lasers and the bias field, and turn on the ML laser for 1D trapping. For four different displacements (shown in red, yellow, green and blue), the atoms follow a trajectory that leads back to the trap center. Purple dashed trajectories show the behavior when the ML beam polarizations are intentionally reversed and exhibit an anti-confining force. The corresponding phase space plot is shown in Figure 2.13

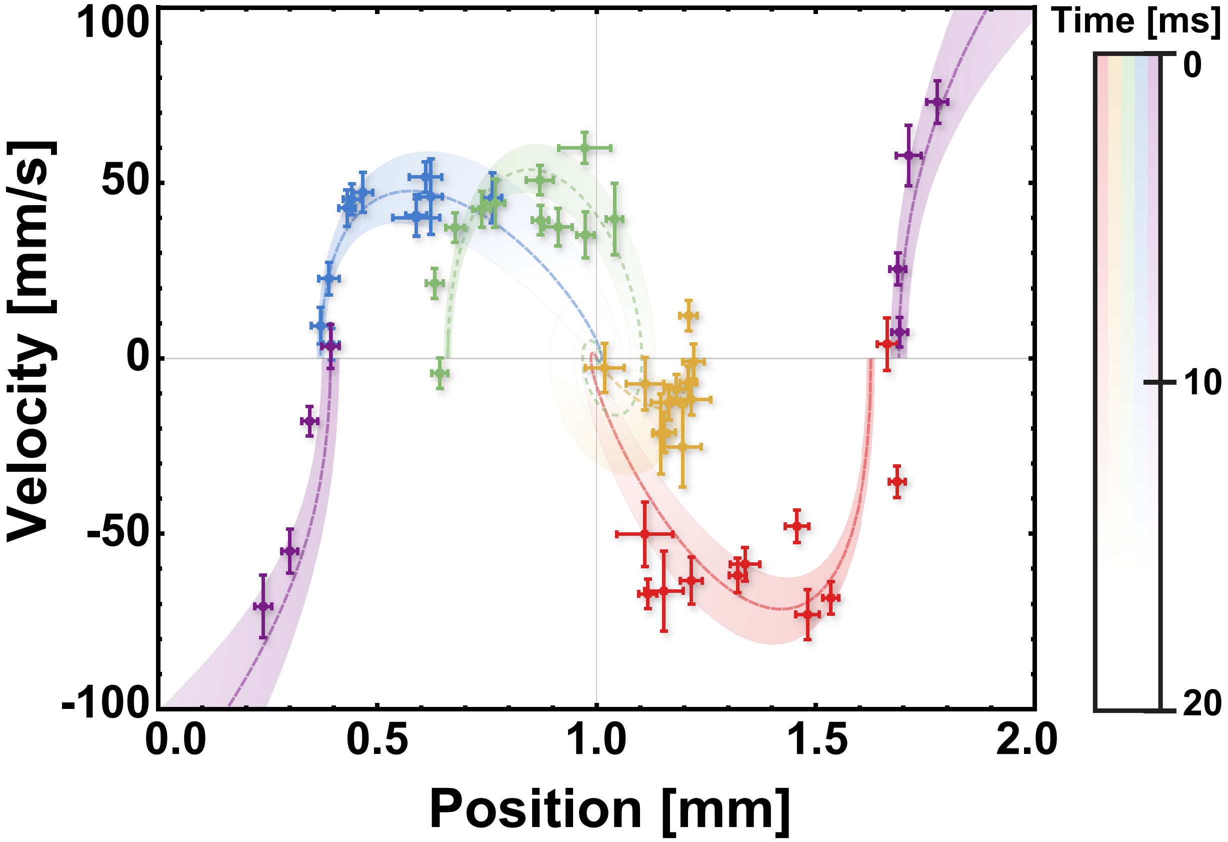

Figure 2.13: Phase space trajectories for atoms trapped in a two-photon, optical frequency comb MOT. Smooth curves are fits to a damped harmonic oscillator, with fit uncertainties shown as bands. Purple features show the behavior when the ML beam polarizations are intentionally reversed and exhibit an anti-confining force. Error bars are statistical over repeated measurements. The corresponding position space plot is shown in Figure 2.12

2.6 Outlook

Laser cooling and trapping with an optical frequency comb for one-photon transition typically cannot efficiently use the full power of laser, because of the many frequency components that are not used in the laser cooling and trapping process. However, optical frequency comb laser cooling and trapping could be suitable if a laser cooling and trapping scheme can make use of multiple comb teeth, by using the optical frequency comb as both the cooling and repumping laser. Take this idea, one step further, multiple species can be cooled and trapped simultaneously with a single optical frequency comb. For the demonstration of loading and trapping of both species of rubidium atoms in an one-photon optical frequency comb MOT with a single ML laser, see Appendix B.

Indeed, the techniques presented in this chapter is most powerful if simultaneous addressing of multiple transitions are required for ultraviolet light. The high instantaneous intensity of the ML laser makes it suitable for generation of ultraviolet light from nonlinear processes. It is possible to apply the techniques presented in this chapter in the deep UV to laser cool and magneto-optically trap species such as H, C, N, O, and $\bar{\mathrm{H}}$ (anti-hydrogen).

Figure 2.14 illustrates a potential laser cooling and trapping scheme for H and $\bar{\mathrm{H}}$. Two-photon Doppler cooling has previously been proposed on the $1S\rightarrow 2S$ transition for H and $\bar{\mathrm{H}}$ (through forced quenching of the $2S$ state) with a CW laser [101] or optical frequency comb [59] centered at 243 nm. We propose to cool on the $1S\rightarrow 2S$ transition instead. There are multiple reasons for using this transition: we have demonstrated a similar $5S\rightarrow 5D$ transition, and the $1S\rightarrow 2S$ transition has a lower photoionization losses [55]. Further, multiple teeth of the two-photon comb (see Eq. (2.31) and Figure 2.3) can be used simultaneously to drive different hyperfine and fine-structure transitions in parallel at no cost in additional laser power (Figure 2.14). In the limit that both the average and instantaneous excited state probabilities are small ($\Omega_N \ll \Gamma < 2\pi f_\mathrm{r}$) with unequal detunings from resonance for each transition being driven, coherences between multiple excited states can be neglected and each line will act essentially as an independent two-level system.

In addition, a comb tooth spacing of $f_{\mathrm{r}} = 83.5$ MHz will simultaneously drive all six of the allowed [21] hyperfine and fine structure transitions [66] on $1S \rightarrow 3D$ with a red detuning between $\Gamma/3$ and Γ. The optical frequency comb's ability to "repump" its own hyperfine states allows this scheme to be applied robustly to magnetically trapped samples, where the presence of polarization imperfections or off-resonant excitation to undesired excited states can cause spin flips that must be repumped. As mentioned at the beginning of this section and documented in Appendix B, we have demonstrated a single ML laser can simultaneously address multiple transitions to laser cool and repump a MOT.

Due to low anticipated scattering rates, H and $\bar{\mathrm{H}}$ (and species like C, N and O) will likely need to be slowed using other means [49, 51]. Direct comb laser cooling and trapping would then be used to cool them to the Doppler limit in a MOT.

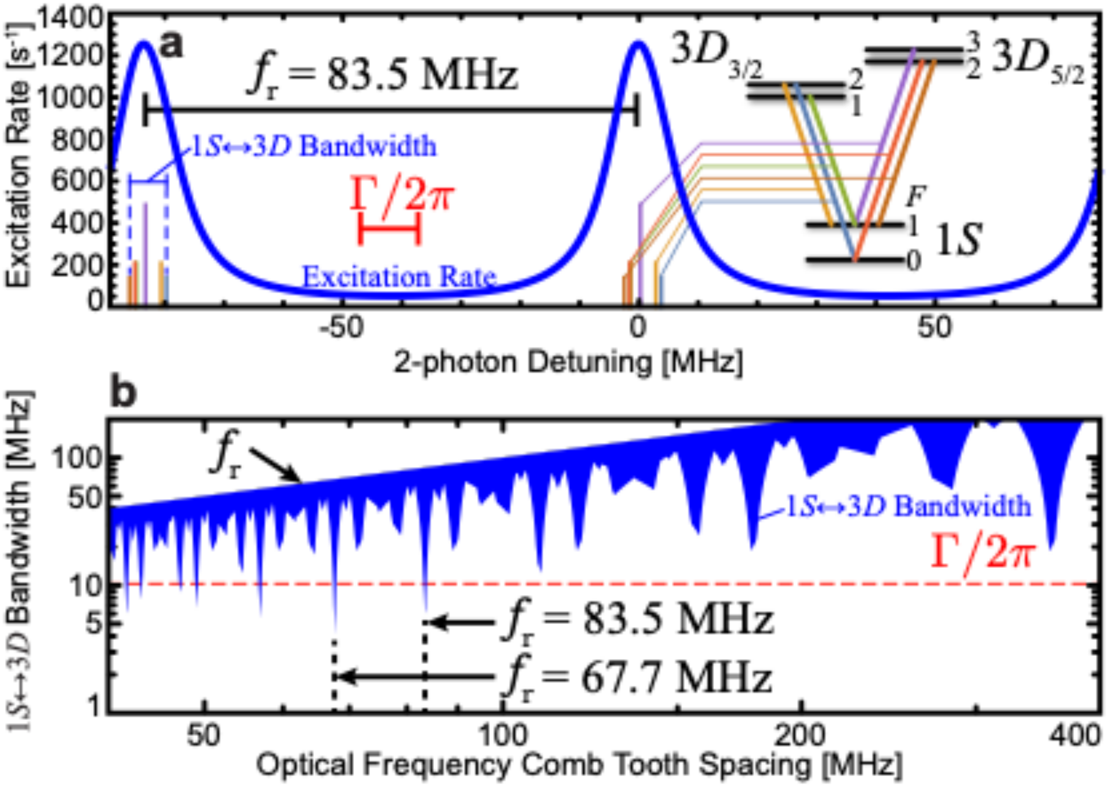

Figure 2.14: Calculated parameters for laser cooling atomic hydrogen on $1S \rightarrow 3D$. **a** Calculated excitation rate (blue) as a function of twice the optical frequency (the two-photon effective frequency at 102.5 nm) for a comb with repetition rate $f_r = 83.5$ MHz. The spectrum shown is the atomic spectrum modulo f_r, which is how the spectrum will appear when scanning a frequency comb.**b** The bandwidth spanned by the six allowed fine and hyperfine transition frequencies modf_r is less than the natural linewidth of $\Gamma/2\pi = 10.3$ MHz for this repetition rate and a few others.

CHAPTER 3

Momentum Transfer via a Stimulated Force

3.1 Advantages of Using a Stimulated Force for Laser Slowing

The rich internal structure and the readily available long-range and anisotropic interactions present in diatomic molecules make them highly desirable candidates for precision measurements [98, 48, 94, 6, 65], quantum information processing [28, 9, 81, 50, 12, 73] and quantum chemistry [77, 67]. A few years ago, the first molecular magneto-optical trap (MOT) was demonstrated by the Demille group at Yale with SrF [13] in 2014, and subsequently demonstrated by the Doyle group at Harvard [8] and by the Tarbutt group at Imperial College [92] in 2017, both with CaF. Despite the great success in producing molecular MOTs, the number of molecules that can be loaded in a MOT is low. To date the highest number of molecules ever loaded in a MOT is on the order of 10^5 [8]. The primary limiting factor to the number of trappable molecules in a MOT turns out to be the number of molecules that are slowed to a laser-coolable and -trappable speed. This is because unlike atoms, molecules have complex structures. As shown in Figure 3.1, the presence of more than one atoms in a molecule results in vibrational and rotational motions. This means that after a molecule is driven to the excited state, there are a multitude of possible vibrational and rotational states the molecule can spontaneously decay into. Take CaF for example, as illustrated in Figure 3.2 [8], one CaF molecule would decay into a dark state after every 500 excitations. On the other hand, typically 10^4 photons are needed for laser slowing and trapping of molecules coming off a cryogenic buffer gas beam or a supersonic beam source. Adding additional repump lasers would get the molecule out of the dark states, at the cost of reduced scattering rate, which subsequently results in prolongation of slowing distance. As the slowing distance

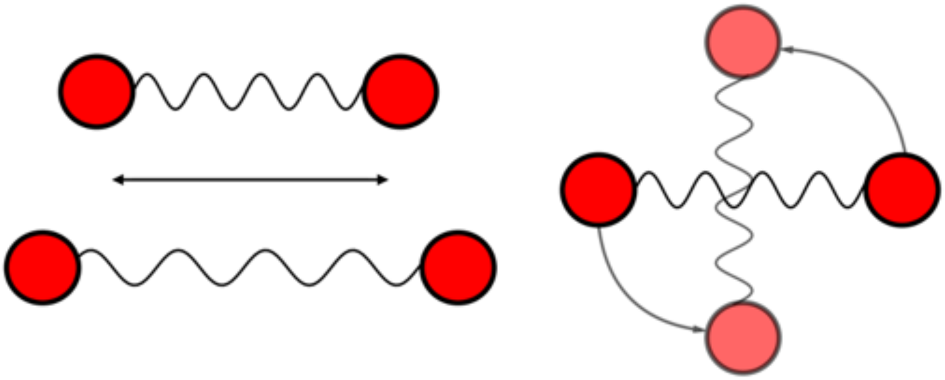

Figure 3.1: Presence of rotational and vibrational motions in a diatomic molecule.

gets longer, the molecular beam becomes more spread-out in the transverse direction, thus further reducing the number of laser coolable/trappale molecules.

Stimulated optical forces might be a better candidate to transfer momentum to a molecular beam. Stimulated forces employ stimulated emissions instead of spontaneous emissions to return an excited molecule back down to the ground state. This property has two main implications: first, large number of momentum transfers can be delivered before a spontaneous emission sets in, thus reducing the possibility of the molecule accidentally falling into a dark state; second, stimulated forces are not limited by the scattering rate γ of a transition, and can be many times stronger than the spontaneous scattering forces - hence a much smaller slowing distance. To demonstrate the short distance an ideal stimulated force can bring, we following the deceleration scheme proposed by Jayich *et al.* [56] and make the following computation (the details of the scheme are given in Section 3.2):

Assume we want to slow a cryogenic buffer gas beam source of CaF moving at $v_0 = 150$ m/s [8]. Using a ML laser centered at 531 nm, the number of momentum transfers required to slow the beam to a full stop is ≈ 16000. With a repetition rate of $f_{\text{rep}} = 80$ MHz, the time required to apply this many momentum transfers is ≈ 2 ms, and the distance traveled by a molecule before coming to a full stop is ≈ 1.5 cm. In comparison, white light slowing has demonstrated laser slowing from 60 m/s to laser trappable speed in 20 cm for a small population [46].

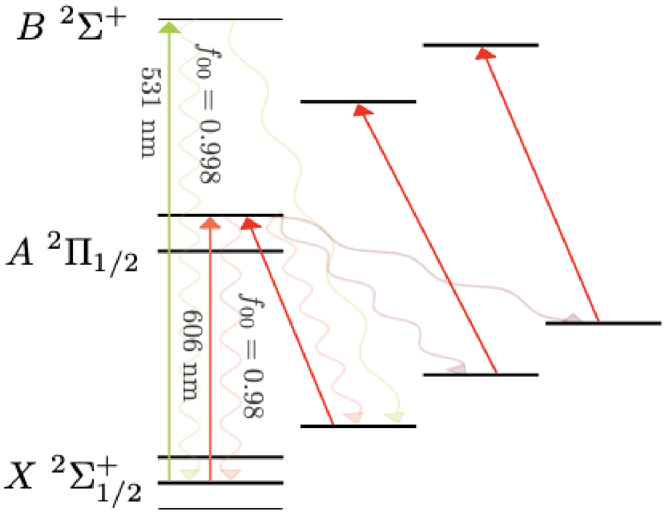

Figure 3.2: Energy level diagram of CaF [8]. The solid lines are transitions for excitation, while the wavy lines indicate potential decay paths to different vibrational levels from the main photon cycling transitions.

3.2 Stimulated Force Slowing with ML Laser Pulses

In this section we describe our method of laser deceleration (proposed by Jayich *et al.* [56]).

The stimulated force we demonstrate here is generated by the fast repetition of a cycle in which a time-ordered, counterpropagating pair of picosecond laser pulses ("π-pulses") illuminate the sample. As illustrated in Figure 3.3 (see also [58, 56, 93, 75, 39]), a ground-state molecule from a molecular beam is first excited by absorbing a photon from a "pump pulse" that is counter-propagating with respect to the molecular beam, thereby losing momentum $\hbar k$. The molecule is then immediately illuminated by a co-propagating "dump pulse," which deterministically drives the molecule back to its original ground state via stimulated emission and removes another $\hbar k$ of momentum from the molecule. By setting the spacial path length difference between the pump and dump beam path, the temporal delay between the pump and dump pulse can be chosen, hence the direction of net momentum transfers can be controlled.

This cycle can be repeated immediately to create an approximately continuous decel-

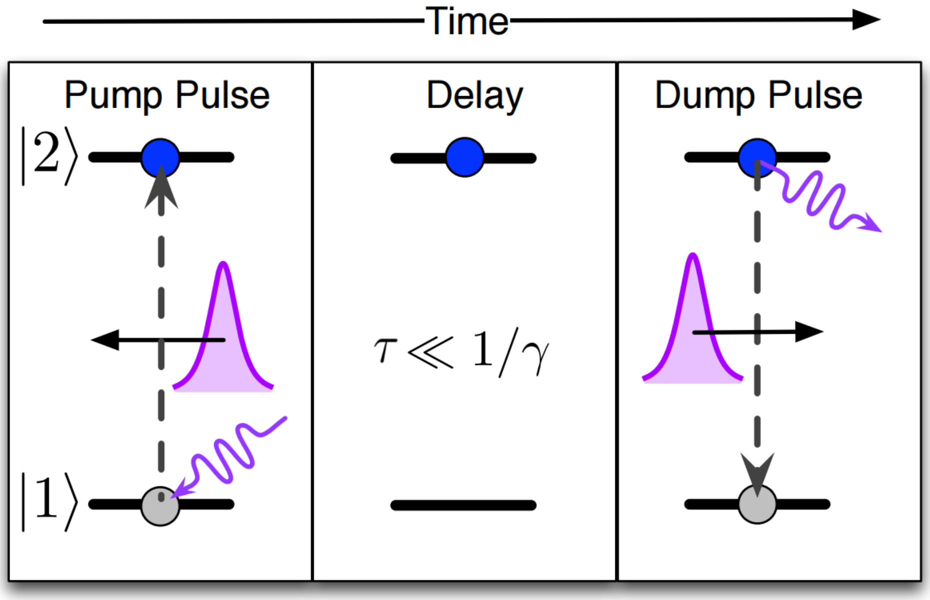

Figure 3.3: Pulse sequence of the stimulated force. A "pump" pulse, counter-propagating to the direction of the molecular beam, excites each molecule, removing $\hbar k$ momentum. Before the molecule spontaneously decays ($\tau \ll 1/\gamma$, where $1/\gamma$ is the spontaneous emission lifetime), a co-propagating "dump" pulse deterministically removes another $\hbar k$ momentum, bringing each molecule back to its initial ground state.

eration force that can be much stronger than spontaneous scattering. Assuming perfect population transfer fidelity and infinite laser power, this scheme will only be limited by the finite duration of the ML laser pulse. In addition, the broad spectrum coverage of the ultrafast laser pulses ($>$ 10 GHz for a 30 ps pulse) allows for simultaneous deceleration of molecules from a wide range of velocities.

The effectiveness of this scheme depends on how well each pump or dump pulse can transfer population between the ground state and the excited state. Consider the case where a first pump pulse fails to excite the molecule to its excited state. If the co-propagating dump pulse successfully excites the molecule, then the molecule would gain instead of lose a momentum $\hbar k$. A subsequent pump pulse could then de-excite the molecule, adding another $\hbar k$ and make things even worse: indeed, a failed population transfer could reverse the direction of the stimulated force!

3.2.1 Single Photon Cooling

As a result of the broad spectrum coverage of the ML laser, the stimulated force slowing method described in the previous section is not velocity-selective. This means that ML laser pulses would keep transfering momentum to molecules that have been slowed to a full stop, and the molecules would be accelerated in the reverse direction back to the beam source if no stopping mechanism is applied.

In [56], the authors also provided a way to stop the molecules that have reached a desired stopping velocity. After a burst of deceleration cycles of ML pulses, a narrow-band colinear CW laser is turned on to optically pump molecules that have reached a desired stopping velocity into a long-lived dark state. Because of Doppler shift, molecules that do not fall into the stopping velocity range are not sensitive to the CW laser, hence only molecules that have reached the stopping velocity would be “selected” out of the effect of further ML laser pulses. By choosing the duration of the ML pulse burst, we can ensure all molecules that have reached the stopping velocity are optically pumped and are no longer addressable by the ML laser.

This method has the advantage that it performs single-photon cooling at the same time. Because of the narrow frequency band of the CW laser, dark state molecules optically pumped by the CW laser are highly localized in velocity space, hence experience a phase space compression. Entropy is carried away by the spontaneously emitted photons, and the molecular beam is thus cooled.

3.3 Benchmarking Stimulated Force with ML Laser Pulses

To benchmark the effectiveness of the stimulated force molecular slowing scheme proposed in Section (3.2), an atomic acceleration experiment is designed and performed. Instead of directly testing the stimulated force on a molecular beam, we illuminate an atomic MOT (initially at rest) with a train of ML pulses, and observe the resultant speed.

Benchmarking the stimulated force consists of two parts: benchmarking how well a single ML pulse (pair) can transfer population between the ground and excited state, and benchmarking the accelerating efficiency for a train of pulse pairs. In Section (3.4) we will develop the theory for single ML pulse population transfer and describe the experiment that characterize the single pulse population transfer fidelity in our system, and in Section (3.5) we'll develop the theory for momentum transfer for a train of pulse pairs, and the experimental procedure that benchmarks the efficiency of our system.

3.4 Single ML Pulse (Pair) Excitations

In this section, we start by developing a theory to describe atomic excitation by a single ML pulse. This theory provides the ML laser power needed to achieve the π-pulse condition for an atom located at the beam waist center. We then develop a theory for a finite volume atomic sample to account for the finite size of the atomic MOT in our experimental setup. Finally we present experimental results for these space-averaged excitations by measuring the fluorescence of single ML-pulse(-pair)-illuminated MOT. The results presented in this section benchmark the effectiveness of ML pulses to transfer population between two states, which is an indicator for the effectiveness of the stimulated force with ML pulses to transfer momentum.

3.4.1 Atomic Excitation by a Mode-Locked Pulse

In this subsection, we follow [83] to derive the probability of a ground state atom getting excited by a ML laser pulse.

Consider an atom in the state described by

$$|\psi\rangle = c_1|1\rangle + c_2|2\rangle, \tag{3.1}$$

subject to the following two-level Hamiltonian:

$$H = \frac{\hbar}{2}\begin{pmatrix} -\Delta & \Omega^* \\ \Omega & \Delta \end{pmatrix}. \tag{3.2}$$

Here $|1\rangle$ and $|2\rangle$ represent the ground and excited state respectively, $\Delta \equiv \omega_{\mathrm{a}} - \omega_{\mathrm{laser}}$ is the detuning between the laser and transition frequency, and

$$\Omega(t) = -\frac{\langle 1|\boldsymbol{\mu}\cdot\mathbf{E}(t)|2\rangle}{\hbar} = -\frac{\langle 1|\mu\mathcal{E}(t)|2\rangle}{\hbar} \tag{3.3}$$

is the Rabi frequency, where $\boldsymbol{\mu}$ is the electric dipole moment, $\mathbf{E}(t)$ is the time-dependent electric field strength, and μ and $\mathcal{E}(t)$ are their amplitude. We have assumed the dipole and the electric field aligns in the same direction implicitly. Further, we assume the ML laser pulse's electric field has a hyperbolic secant profile [44]:

$$\mathcal{E}(t) = \mathcal{E}_0 \operatorname{sech}\left(\frac{t}{T_{\mathrm{p}}}\right). \tag{3.4}$$

Then

$$\Omega(t) = \Omega_0 \mathrm{sech}\left(\frac{t}{T_{\mathrm{p}}}\right), \tag{3.5}$$

where $\Omega_0 = -\frac{\langle 1|\mu\mathcal{E}_0|2\rangle}{\hbar} = -\mathcal{E}_0\frac{\langle 1|\mu|2\rangle}{\hbar}$, the peak Rabi frequency, is time-independent.

Apply the Hamiltonian to the time-dependent Schrödinger equation

$$i\hbar\frac{\mathrm{d}}{\mathrm{d}t}|\psi\rangle = H|\psi\rangle, \tag{3.6}$$

and for convenience define $\epsilon \equiv -\dfrac{\Delta}{2}$ and $\nu \equiv \dfrac{\Omega}{2}$, we get

$$i\dot{c}_1 = \epsilon c_1 + \nu c_2, \tag{3.7}$$

$$i\dot{c}_2 = \nu c_1 - \epsilon c_2 \tag{3.8}$$

which can be combined as

$$\ddot{c}_2 - \frac{\dot{\nu}}{\nu}\dot{c}_2 + \left(i\epsilon\frac{\dot{\nu}}{\nu} + \epsilon^2 + \nu^2 - i\dot{\epsilon}\right)c_2 = 0. \tag{3.9}$$

Define a transformation

$$z = \frac{1}{2}\left(\tanh\frac{t}{T_\mathrm{p}} + 1\right), \tag{3.10}$$

$$\dot{c}_2 = \frac{\mathrm{d}c_2}{\mathrm{d}t} = \frac{\mathrm{d}c_2}{\mathrm{d}z}\frac{\mathrm{d}z}{\mathrm{d}t}, \tag{3.11}$$

$$\ddot{c}_2 = \frac{\mathrm{d}}{\mathrm{d}t}\dot{c}_2 = \frac{\mathrm{d}^2c_2}{\mathrm{d}z^2}\left(\frac{\mathrm{d}z}{\mathrm{d}t}\right)^2 + \frac{\mathrm{d}c_2}{\mathrm{d}z}\frac{\mathrm{d}^2z}{\mathrm{d}t^2}. \tag{3.12}$$

With the identity

$$\mathrm{sech}^2x + \tanh^2x = 1, \tag{3.13}$$

we can get

$$\frac{\mathrm{d}z}{\mathrm{d}t} = \frac{1}{2T_\mathrm{p}}\mathrm{sech}^2\left(\frac{t}{T_\mathrm{p}}\right) = \frac{2(1-z)z}{T_\mathrm{p}}, \tag{3.14}$$

$$\frac{\mathrm{d}^2z}{\mathrm{d}t^2} = -\frac{1}{T_\mathrm{p}^2}\mathrm{sech}^2\left(\frac{t}{T_\mathrm{p}}\right)\tanh\left(\frac{t}{T_\mathrm{p}}\right) = -\frac{4z(1-z)(2z-1)}{T_\mathrm{p}^2}, \tag{3.15}$$

and

$$\nu^2 = \left(\frac{\Omega_0}{2}\right)^2\mathrm{sech}^2\left(\frac{t}{T_\mathrm{p}}\right) = \Omega_0^2(1-z)z, \tag{3.16}$$

$$\nu = \Omega_0\sqrt{(1-z)z}. \tag{3.17}$$

Also note

$$\begin{aligned}\frac{\dot{\nu}}{\nu} &= \frac{\dot{\Omega}}{\Omega} = \frac{-\Omega_0\mathrm{sech}\left(\frac{t}{T_\mathrm{p}}\right)\tanh\left(\frac{t}{T_\mathrm{p}}\right)\Big/T_\mathrm{p}}{\Omega_0\mathrm{sech}\left(\frac{t}{T_\mathrm{p}}\right)} \\ &= -\frac{1}{T_\mathrm{p}}\tanh\left(\frac{t}{T_\mathrm{p}}\right) \\ &= -\frac{1}{T_\mathrm{p}}(2z-1). \end{aligned} \tag{3.18}$$

Putting Eq. (3.10), (3.11), (3.12), (3.14), (3.15), (3.16) and (3.18) into Eq. (3.9),

$$z(1-z)\frac{\mathrm{d}^2 c_2}{\mathrm{d}z^2} - (z-\frac{1}{2})\frac{\mathrm{d}c_2}{\mathrm{d}z} + \frac{(\epsilon T_\mathrm{p})^2 + (\Omega_0 T_\mathrm{p})^2(1-z)z - i\dot{\epsilon}T_\mathrm{p}^2 - i\epsilon(2z-1)T_\mathrm{p}}{4(1-z)z} = 0. \quad (3.19)$$

In the resonant case, $\Delta = 0$, $\epsilon = 0$, Eq. (3.19) becomes

$$z(1-z)\frac{\mathrm{d}^2 c_2}{\mathrm{d}z^2} - \left(z-\frac{1}{2}\right)\frac{\mathrm{d}c_2}{\mathrm{d}z} + \left(\frac{\Omega_0 T_\mathrm{p}}{2}\right)^2 = 0. \quad (3.20)$$

Denote $\alpha = \frac{\Omega_0 T_\mathrm{p}}{2}$, $\beta = -\frac{\Omega_0 T_\mathrm{p}}{2}$, and $\gamma = \frac{1}{2}$, Eq. (3.20) can be written as

$$z(1-z)\frac{\mathrm{d}^2 c_2}{\mathrm{d}z^2} + [\gamma - (\alpha+\beta+1)z]\frac{\mathrm{d}c_2}{\mathrm{d}z} - \alpha\beta c_2 = 0. \quad (3.21)$$

Eq. (3.21) is the *hypergeometric equation*, and its solution is given by [40]

$$c_2(z) = AF(\alpha,\beta;\gamma;z) + Bz^{1-\gamma}F(\alpha-\gamma+1,\beta-\gamma+1;2-\gamma;z), \quad (3.22)$$

where F is hypergeometric function

$$\begin{aligned} F(\alpha,\beta;\gamma;z) &= 1 + \frac{\alpha\cdot\beta}{\gamma\cdot 1}z + \frac{\alpha(\alpha+1)\beta(\beta+1)}{\gamma(\gamma+1)\cdot 1\cdot 2}z^2 + \\ &\quad \frac{\alpha(\alpha+1)(\alpha+2)\beta(\beta+1)(\beta+2)}{\gamma(\gamma+1)(\gamma+2)\cdot 1\cdot 2\cdot 3}z^3 + \ldots \end{aligned} \quad (3.23)$$

Then obviously

$$F(\alpha,\beta;\gamma;0) = 1. \quad (3.24)$$

The following identity for the hypergeometric functions is also true:

$$F(\alpha,\beta;\gamma;1) = \frac{\Gamma(\gamma)\Gamma(\gamma-\alpha-\beta)}{\Gamma(\gamma-\alpha)\Gamma(\gamma-\beta)}, \quad (3.25)$$

Now consider an atom starting from the ground state. Equivalently $c_2(t\to-\infty) = c_2(z=0) = 0$ and $c_1(t\to-\infty) = c_1(z=0) = 1$. Then

$$c_2(z=0) = A \Longrightarrow A = 0, \quad (3.26)$$

$$c_2(z) = Bz^{1-\gamma}F(\alpha-\gamma+1,\beta-\gamma+1;2-\gamma;z). \quad (3.27)$$

To get the value of B, differentiate Eq. (3.27) with respect to t,

$$\begin{aligned}\dot{c}_2(z) &= \frac{\mathrm{d}c_2(z)}{\mathrm{d}z}\frac{\mathrm{d}z}{\mathrm{d}t} \\ &= \frac{2(1-z)zB}{T_\mathrm{p}}\Big[(1-\gamma)z^{-\gamma}F(\alpha-\gamma+1,\beta-\gamma+1;2-\gamma;z)+ \\ &\quad z^{1-\gamma}F'(\alpha-\gamma+1,\beta-\gamma+1;2-\gamma;z)\Big] \end{aligned} \tag{3.28}$$

where F' is understood to be $\dfrac{\mathrm{d}F}{\mathrm{d}z}$. Rearrange Eq. (3.8) and use $\epsilon = 0$:

$$c_1(z) = \frac{1}{\nu}\left(i\dot{c}_2(z)+\epsilon c_2(z)\right) = \frac{i\dot{c}_2(z)}{\nu} \tag{3.29}$$

Put Eq. (3.17), (3.24) and (3.28) into Eq. (3.29), and use $\gamma = \dfrac{1}{2}$,

$$\begin{aligned}c_1(z) &= \frac{i\sqrt{1-z}B}{\Omega_0 T_\mathrm{p}}F(\alpha-\gamma+1,\beta-\gamma+1;2-\gamma;z)+ \\ &\quad \frac{2iz\sqrt{1-z}B}{\Omega_0 T_\mathrm{p}}F'(\alpha-\gamma+1,\beta-\gamma+1;2-\gamma;z). \end{aligned} \tag{3.30}$$

Apply the initial condition $c_1(z=0)=1$,

$$\frac{iB}{\Omega_0 T_\mathrm{p}} = 1 \Longrightarrow B = \frac{\Omega_o T_\mathrm{p}}{i}. \tag{3.31}$$

To obtain the excitation probability of an atom after illuminated by a ML pulse, consider $c_2(t\to\infty) = c_2(z=1)$. Putting Eq. (3.25) and (3.31) into Eq. (3.27),

$$\begin{aligned}c_2(z=1) &= BF(\alpha+\frac{1}{2},\beta+\frac{1}{2};\frac{3}{2};1) \\ &= \frac{\Omega_o T_\mathrm{p}}{i}\frac{\Gamma\left(\frac{3}{2}\right)\Gamma\left(\frac{3}{2}-(\alpha+\frac{1}{2})-(\beta+\frac{1}{2})\right)}{\Gamma\left(\frac{3}{2}-(\alpha+\frac{1}{2})\right)\Gamma\left(\frac{3}{2}-(\beta+\frac{1}{2})\right)} \\ &= \frac{\Omega_o T_\mathrm{p}}{i}\frac{\Gamma(3/2)\Gamma(1/2)}{\Gamma(1-\alpha)\Gamma(1-\beta)} \\ &= \frac{\Omega_o T_\mathrm{p}}{i}\frac{\pi/2}{\Gamma(1-\alpha)\Gamma(1+\alpha)} \\ &= \frac{\Omega_o T_\mathrm{p}}{i}\frac{\pi/2}{\alpha\Gamma(1-\alpha)\Gamma(\alpha)} \\ &= \frac{\Omega_o T_\mathrm{p}}{i}\frac{\pi/2}{\alpha\pi/\sin(\pi\alpha)} \\ &= -i\sin\left(\frac{\pi\Omega_0 T_\mathrm{p}}{2}\right). \end{aligned} \tag{3.32}$$

Hence the excitation probability of an atom by a ML pulse is given by

$$\boxed{|c_2(t \to \infty)|^2 = \sin^2\left(\frac{\pi\Omega_0 T_{\mathrm{p}}}{2}\right)}. \tag{3.33}$$

This is known as the Rosen-Zener solution [83].

3.4.2 π-Pulse Condition

In this subsection, we will derive the ML laser beam condition in order to apply π-pulses [22].

As mentioned in Section 3.2, the effectiveness of the stimulated force depends critically on the ability of a single pulse to transfer population from one state to the other. Ideally each ML pulse should either excite a ground state atom to the excited state, or de-excite an excited atom to the ground state. A pulse that satisfies this requirement is called a π-pulse. Equivalently, the population transfer fidelity is one if both sides of Eq. (3.32) are 1. That is,

$$|c_2(t \to \infty)|^2 = \sin^2\left(\frac{\pi\Omega_0 T_{\mathrm{p}}}{2}\right) = 1, \tag{3.34}$$

and Ω_0 must satisfy

$$\Omega_0 T_{\mathrm{p}} = 1. \tag{3.35}$$

Before we proceed further with Eq. (3.35), we attempt to characterize the ML laser field. Without loss of generality we assume the atom is at the beam waist with a characteristic $1/e^2$ intensity radius (or equivalently a $1/e$ electric field amplitude radius) of w_0. The electric field can be written in the form

$$\boldsymbol{\mathcal{E}}(r,t) = \mathcal{E}_{\mathrm{center}}(t)\exp\left(-\frac{r^2}{w_0^2}\right)\hat{r}, \tag{3.36}$$

where $r = \sqrt{x^2+y^2}$ is the radial distance from the center axis of the beam, $\mathcal{E}_{\mathrm{center}}(t)$ is the peak electric field amplitude at the center axis of the beam. Using the relation between electric field and intensity

$$I(r,t) = \frac{1}{2}c\epsilon_0|\boldsymbol{\mathcal{E}}(r,t)|^2 = \frac{1}{2}c\epsilon_0|\mathcal{E}_{\mathrm{center}}(t)|^2\exp\left(-\frac{2r^2}{w_0^2}\right) \tag{3.37}$$

we find total instantaneous laser power

$$P(t) = \frac{\pi c \epsilon_0 w_0^2 |\mathcal{E}_{\text{center}}(t)|^2}{4} \tag{3.38}$$

We can only measure time-averaged laser power in the lab, hence to guide our experimental work we need to convert the instantaneous laser power in Eq. (3.38) to time-averaged laser power. To do so, we start by finding the total laser energy in each ML pulse. Assume the electric field amplitude takes the form given by Eq. (3.4):

$$P_{\text{pulse}} \quad = \quad \int_{-\infty}^{\infty} P(t) dt = \frac{\pi c \epsilon_0 w_0^2|}{2} |\mathcal{E}_{0,\text{center}}|^2 T_{\text{p}}. \tag{3.39}$$

For a ML laser with repetition rate f_{r}, the time-averaged laser power $\bar{P}$ is given by

$$\bar{P} = \frac{\pi c \epsilon_0 w_0^2|}{2} |\mathcal{E}_{0,\text{center}}|^2 T_{\text{p}} f_{\text{r}}. \tag{3.40}$$

The electric field amplitude at the center axis of the beam is

$$|\mathcal{E}_{0,\text{center}}| = \sqrt{\frac{2\bar{P}}{\pi c \epsilon_0 w_0^2 T_{\text{p}} f_{\text{r}}}}. \tag{3.41}$$

For an atomic transition with saturation intensity I_{sat}

$$I_{\text{sat}} \equiv \frac{\hbar \omega_{\text{a}}^3 \gamma}{12 \pi c^2}, \tag{3.42}$$

where ω_{a} is the atomic transition (angular) frequency and $\gamma \equiv 1/\tau$ is the natural linewidth (τ is the lifetime of the excited state), the Rabi frequency is related to the electric field of the laser via

$$|\Omega| = \gamma \sqrt{\frac{I}{2 I_{\text{sat}}}} = |\mathcal{E}| \sqrt{\frac{3 \pi \gamma \epsilon_0}{\hbar} \left(\frac{c}{\omega_{\text{a}}}\right)^3}. \tag{3.43}$$

In order to require the center axis Rabi frequency at the beam waist to satisfy the π-pulse condition (3.35), we must have

$$|\mathcal{E}_{0,\text{center}}| \sqrt{\frac{3 \pi \gamma \epsilon_0}{\hbar} \left(\frac{c}{\omega_{\text{a}}}\right)^3} T_{\text{p}} = 1, \tag{3.44}$$

or

$$|\mathcal{E}_{0,\text{center}}| = \frac{1}{T_{\text{p}}} \sqrt{\frac{\hbar}{3 \pi \gamma \epsilon_0} \left(\frac{\omega_{\text{a}}}{c}\right)^3}. \tag{3.45}$$

Combining Eq. (3.41) and (3.45) to get the π-pulse condition time-averaged laser power

$$\boxed{\bar{P}_\pi = \frac{\hbar w_0^2 f_\mathrm{r} \omega_\mathrm{a}^3}{6\gamma T_\mathrm{p} c^2}}. \tag{3.46}$$

For $w_0 = 0.65$ mm, $f_\mathrm{r} = 80$ MHz, $T_\mathrm{p} = 30$ ps on a 780 nm transition with a 6.07 MHz linewidth (the ${}^2S_{1/2} \to {}^2P_{3/2}$ transition for ^{85}Rb), the time-averaged laser power for π-pulse condition at the beam waist (on the center axis) is ≈81 mW.

3.4.3 Single Pulse (Pair) Excitation for a Finite Size Sample

In this subsection, we will develop a theory to describe the atomic excitation in a sample of atoms whose size is many times larger than the laser wavelength.

Each ML pulse can be thought of as an operator that rotates the internal state and changes the momentum state of an atom. We can represent the state of an atom as $|i, n\rangle$, where $i \in \{1, 2\}$ represents the internal state of the atom, and $n \equiv \frac{mv}{\hbar k}$ corresponds to the number of $\hbar k$ momentum an atom has in the pump beam propagation direction (assume the atom starts from at rest). Using

$$\int_{-\infty}^{\infty} \mathrm{sech}\left(\frac{t}{T_\mathrm{p}}\right) \mathrm{d}t = \pi T_\mathrm{p}, \tag{3.47}$$

we can rewrite Eq. (3.33), the excitation probability of a ground state atom by a ML pulse, as

$$\mathcal{P}_\mathrm{e}(\theta) = \sin^2\left(\frac{\pi \Omega_0 T_\mathrm{p}}{2}\right) = \sin^2\left(\frac{\theta}{2}\right), \tag{3.48}$$

where

$$\begin{aligned} \theta &\equiv \pi \int_{-\infty}^{\infty} \Omega(t) \mathrm{d}t \\ &= \pi \Omega_0 \int_{-\infty}^{\infty} \mathrm{sech}\left(\frac{t}{T_\mathrm{p}}\right) \mathrm{d}t \\ &= \pi \Omega_0 T_\mathrm{p} \end{aligned} \tag{3.49}$$

is the temporal pulse area (with a constant factor π). We can then write the pump beam pulse operator as

$$\begin{aligned} U_{\mathrm{p}}(\theta) &= \left(\sum_n \rightarrow\right) \cos\left(\frac{\theta}{2}\right)|1,n\rangle\langle 1,n| + \cos\left(\frac{\theta}{2}\right)|2,n\rangle\langle 2,n| - \\ &\qquad i\sin\left(\frac{\theta}{2}\right)|1,n-1\rangle\langle 2,n| - i\sin\left(\frac{\theta}{2}\right)|2,n+1\rangle\langle 1,n|, \end{aligned} \tag{3.50}$$

and the dump beam pulse operator as

$$\begin{aligned} U_{\mathrm{d}}(\theta) &= \left(\sum_n \rightarrow\right) \cos\left(\frac{\theta}{2}\right)|1,n\rangle\langle 1,n| + \cos\left(\frac{\theta}{2}\right)|2,n\rangle\langle 2,n| - \\ &\qquad i\sin\left(\frac{\theta}{2}\right)|1,n+1\rangle\langle 2,n| - i\sin\left(\frac{\theta}{2}\right)|2,n-1\rangle\langle 1,n|. \end{aligned} \tag{3.51}$$

It should be understood that an implicit summation over n is taken for these operators even if the summation is not written explicitly from now on.

Consider an atom in the state $|\psi\rangle = |1,n\rangle$. The state after a pump pulse is given by

$$\begin{aligned} \tilde{\rho}_{\mathrm{p}} &= U_{\mathrm{p}}(\theta)|\psi\rangle\langle\psi|U_{\mathrm{p}}^{\dagger}(\theta) \\ &= U_{\mathrm{p}}(\theta)|1,n\rangle\langle 1,n|U_{\mathrm{p}}^{\dagger}(\theta) \\ &= \left[\cos\left(\frac{\theta}{2}\right)|1,n\rangle\langle 1,n| - i\sin\left(\frac{\theta}{2}\right)|2,n+1\rangle\langle 1,n|\right]U_{\mathrm{p}}^{\dagger}(\theta) \\ &= \cos^2\left(\frac{\theta}{2}\right)|1,n\rangle\langle 1,n| + \sin^2\left(\frac{\theta}{2}\right)|2,n+1\rangle\langle 2,n+1| - \\ &\quad -i\sin\left(\frac{\theta}{2}\right)\cos\left(\frac{\theta}{2}\right)\left(|2,n+1\rangle\langle 1,n| - |1,n\rangle\langle 2,n+1|\right). \end{aligned} \tag{3.52}$$

In deriving Eq. (3.33), we assumed the atom is a point located at the beam waist center position. In practice, however, the atoms are distributed over a macroscopic volume, typically with a $1/\mathrm{e}^2$ number density radius of $\sim 100\ \mu$m. This is a much bigger scale than the wavelength of an optical transition, which means atoms at different spacial locations will have different spatial phase. The overall effect of this finite sample size on ML pulse excitation is that the phase of atoms in the sample are all scrambled. The approach we take to account for this effect is to drop the off-diagonal matrix elements of the density matrix to average over all relative pulse phases. The effective state after the pump pulse is therefore

$$\rho_{\mathrm{p}} = \cos^2\left(\frac{\theta}{2}\right)|1,n\rangle\langle 1,n| + \sin^2\left(\frac{\theta}{2}\right)|2,n+1\rangle\langle 2,n+1|. \tag{3.53}$$

By the same token, to get the state of the atom after the dump pulse, we can apply the dump pulse operator to the density matrix ρ_{p} to find $\rho_{\mathrm{pd}} = U_{\mathrm{p}}(\theta)\rho_{\mathrm{p}}U_{\mathrm{p}}^{\dagger}(\theta)$. However, this does not account for the possible spontaneous emission that happens in between the pump and dump pulses. To include the spontaneous emission effect, assume the atomic decay rate is γ and the inter-pulse delay time is τ. The probability that a spontaneous emission happens for an excited atom in between the pump and dump pulse is

$$\mathcal{P}_{\gamma\tau} = \left(1 - \mathrm{e}^{-\gamma\tau}\right)\sin^2\left(\frac{\theta}{2}\right). \tag{3.54}$$

Then the state right before the dump pulse arrives is

$$\begin{aligned}\rho_{\tau\mathrm{p}} &= \cos^2\left(\frac{\theta}{2}\right)|1,n\rangle\langle 1,n| + \left(1 - \mathrm{e}^{-\gamma\tau}\right)\sin^2\left(\frac{\theta}{2}\right)|1,n+1\rangle\langle 1,n+1| + \\ &\quad \mathrm{e}^{-\gamma\tau}\sin^2\left(\frac{\theta}{2}\right)|2,n+1\rangle\langle 2,n+1|,\end{aligned} \tag{3.55}$$

and the state of the atom right after the dump pulse is

$$\begin{aligned}\rho_{\mathrm{d}\tau\mathrm{p}} = &= U_{\mathrm{d}}(\theta)\rho_{\tau\mathrm{p}}U_{\mathrm{d}}^{\dagger}(\theta) \\ &= |1\rangle\langle 1| \otimes \left[\cos^4\left(\frac{\theta}{2}\right)|n\rangle\langle n| + \left(1 - \mathrm{e}^{-\gamma\tau}\right)\cos^2\left(\frac{\theta}{2}\right)\sin^2\left(\frac{\theta}{2}\right)|n+1\rangle\langle n+1| + \right. \\ &\quad \left. \mathrm{e}^{-\gamma\tau}\sin^4\left(\frac{\theta}{2}\right)|n+2\rangle\langle n+2|\right] + \\ &\quad |2\rangle\langle 2| \otimes \left[\cos^2\left(\frac{\theta}{2}\right)\sin^2\left(\frac{\theta}{2}\right)|n-1\rangle\langle n-1| + \left(1 - \mathrm{e}^{-\gamma\tau}\right)\sin^4\left(\frac{\theta}{2}\right)|n\rangle\langle n| + \right. \\ &\quad \left. \mathrm{e}^{-\gamma\tau}\cos^2\left(\frac{\theta}{2}\right)\sin^2\left(\frac{\theta}{2}\right)|n+1\rangle\langle n+1|\right] + \text{ off-diagonal terms.}\end{aligned} \tag{3.56}$$

The probability that an atom emits a photon *after* both pulses is

$$\mathcal{P}_{\gamma\mathrm{dp}} = \mathrm{Tr}_n(\langle 2|\rho_{\mathrm{d}\tau\mathrm{p}}|2\rangle) = (1 + \mathrm{e}^{-\gamma\tau})\sin^2\left(\frac{\theta}{2}\right)\cos^2\left(\frac{\theta}{2}\right) + (1 - \mathrm{e}^{-\gamma\tau})\sin^4\left(\frac{\theta}{2}\right). \tag{3.57}$$

The expected number of photons emitted per atom per pulse pair, then, is

$$\langle N_\gamma(\theta)\rangle = \mathcal{P}_{\gamma\tau} + \mathcal{P}_{\gamma\mathrm{dp}} = 2\sin^2\left(\frac{\theta}{2}\right)\left[1 - \mathrm{e}^{-\gamma\tau}\sin^2\left(\frac{\theta}{2}\right)\right],$$

or

$$\boxed{\langle N_\gamma(\theta)\rangle = 2\sin^2\left(\frac{\theta}{2}\right)\left[1 - \mathrm{e}^{-\gamma\tau}\sin^2\left(\frac{\theta}{2}\right)\right]}. \tag{3.58}$$

Next, we will average over different pulse areas θ. There are two reasons to why we need to average over pulse areas: first, the MOT has a finite size, and for an atom located 100 μm away from the beam center of a 0.65 mm beam, the amplitude of electric field is 98.8% compare to at the center of the beam. Second, there is pulse-to-pulse fluctuation in energy per pulse (this will be addressed in Section 3.4.4).

We assume the pulse areas from the pump and dump pulses are completely correlated but chosen from a normal distribution centered at θ_0 with standard deviation $\kappa\theta_0$:

$$D(\theta, \theta_0, \kappa) = \frac{1}{\kappa\theta_{\mathrm{o}}}\frac{1}{\sqrt{2\pi}}\mathrm{e}^{-\left(\frac{\theta}{\theta_{\mathrm{o}}}-1\right)^2/2\kappa^2}. \tag{3.59}$$

Here κ is the fractional standard deviation. Using Eq. (3.48) and (3.59), we can find the average expected excitation probability by a single ML pulse:

$$\bar{P}_1(\theta_{\mathrm{o}}, \kappa) \;=\; \int_{-\infty}^{\infty} D(\theta, \theta_0, \kappa)\mathcal{P}_{\mathrm{e}}(\theta)\mathrm{d}\theta = \frac{1}{2}\left(1 - \mathrm{e}^{-\kappa^2\theta_{\mathrm{o}}^2/2}\cos\left(\theta_{\mathrm{o}}\right)\right), \tag{3.60}$$

or

$$\boxed{\bar{P}_1(\theta_{\mathrm{o}}, \kappa) = \frac{1}{2}\left(1 - \mathrm{e}^{-\kappa^2\theta_{\mathrm{o}}^2/2}\cos\left(\theta_{\mathrm{o}}\right)\right)}. \tag{3.61}$$

At π-pulse condition, $\theta_{\mathrm{o}} = \pi$. We define

$$\bar{P}_\kappa \equiv \bar{P}_1(\pi, \kappa) = \frac{1}{2}\left(1 + \mathrm{e}^{-\kappa^2\pi^2/2}\right), \tag{3.62}$$

then

$$\mathrm{e}^{-\kappa^2\pi^2/2} = 2\bar{P}_\kappa - 1. \tag{3.63}$$

We can also find the probability of an atom in the excited state after both the pump and dump pulse, but this quantity is hard to measure directly because the possible spontaneous emissions in between pump and dump pulses complicate any fluorescence measurement. An easier quantity to measure is the expected average number of photons emitted per pump-dump pulse pair:

$$\begin{aligned}\left\langle \bar{N}_\gamma(\theta_{\mathrm{o}})\right\rangle \;&=\; \int_{-\infty}^{\infty} D(\theta)\left\langle N_\gamma(\theta)\right\rangle \mathrm{d}\theta \\ &=\; \left(1 - \mathrm{e}^{-\kappa^2\theta_{\mathrm{o}}^2/2}\cos\left(\theta_{\mathrm{o}}\right)\right) - \\ &\quad\; \frac{1}{4}\mathrm{e}^{-\gamma\tau}\left(3 + \mathrm{e}^{-2\kappa^2\theta_{\mathrm{o}}^2}\cos\left(2\theta_{\mathrm{o}}\right) - 4\mathrm{e}^{-\kappa^2\theta_{\mathrm{o}}^2/2}\cos\left(\theta_{\mathrm{o}}\right)\right),\end{aligned} \tag{3.64}$$

or

$$\boxed{\left\langle \bar{N}_{\gamma}(\theta_{\mathrm{o}}) \right\rangle = \left(1 - \mathrm{e}^{-\kappa^2\theta_{\mathrm{o}}^2/2}\cos(\theta_{\mathrm{o}})\right) - \frac{1}{4}\mathrm{e}^{-\gamma\tau}\left(3 + \mathrm{e}^{-2\kappa^2\theta_{\mathrm{o}}^2}\cos(2\theta_{\mathrm{o}}) - 4\mathrm{e}^{-\kappa^2\theta_{\mathrm{o}}^2/2}\cos(\theta_{\mathrm{o}})\right)}. \tag{3.65}$$

At the π-pulse condition, Eq. (3.65) reduces to

$$\left\langle \bar{N}_{\gamma}(\pi) \right\rangle = 1 - \frac{3}{4}\mathrm{e}^{-\gamma\tau} + (1 - \mathrm{e}^{-\gamma\tau})(2\bar{P}_{\kappa} - 1) - \frac{1}{4}\mathrm{e}^{-\gamma\tau}(2\bar{P}_{\kappa} - 1)^4. \tag{3.66}$$

We will use the theory we have developed in this subsection to determine experimental parameters in the next subsection (3.4.4).

3.4.4 Experimental Results on Single-Pulse(-Pair)-Induced MOT Fluorescence

As explained in Section (3.2), for ML deceleration of molecules, it is important to ensure high population transfer fidelity between the ground and excited states by single pump and dump pulses. In this subsection, we will describe a method that allows us to characterize and optimize the population transfer fidelity in our system, and present the experimental results.

As illustrated in Figure 3.4, we characterize population transfer fidelity by collecting spontaneous emission fluorescence after illuminating the MOT with one ML pump pulse, one dump pulse, and one pump-then-dump pulse pair. The path length difference between the pump and dump beam path would give rise to a delay of (310 ± 60) ps. We first prepare a ^{85}Rb MOT of $\sim 10^7$ atoms with initial temperature of $\sim 120\,\mu$K. The MOT temperature is determined by methods described in Section 2.3.1. We then turn off the MOT's magnetic field and CW lasers (both the cooling and repumping laser) to release the atoms, and illuminate the ML laser pulse onto the atoms. A Conoptics Model 360-80 Pockels cell is used for pulse picking (power extinction ratio$\geq 0.7\%$). 2.5 μs elapses between the release of atoms and the ML pulse arrives. Another 2.5 μs later the MOT's magnetic field and CW lasers are turned back on, and wait for another 45 μs later before starting the next fluorescence collection sequence. A Thorlabs PDA36A photodiode is left on to collect the fluorescence emitted by the excited atoms during the entire process, with a trigger synchronized to the ML pulse.

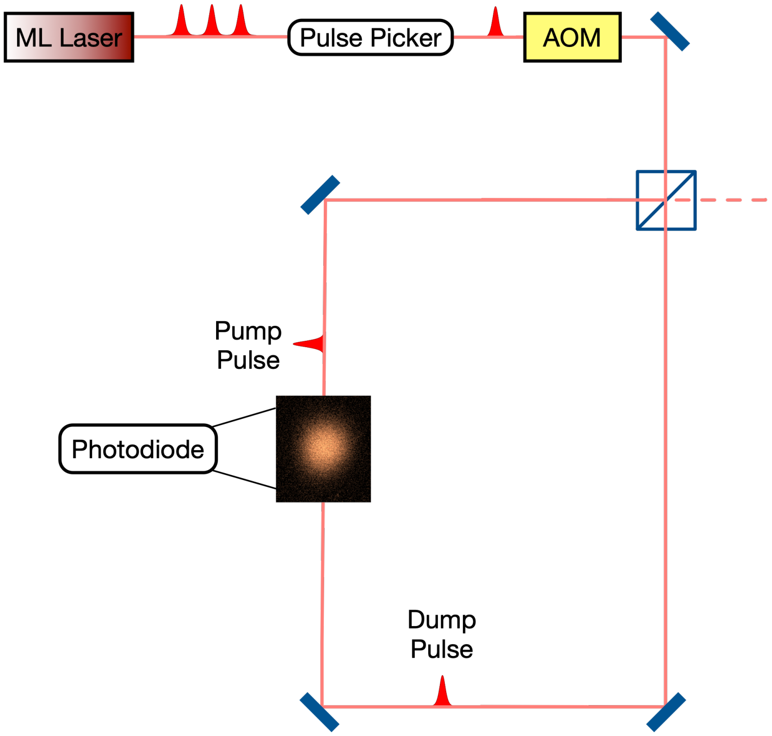

Figure 3.4: Experimental setup for single-pulse(-pair)-induced MOT fluorescence. A pre–cooled sample of atoms are released from a MOT by turning off the MOT magnetic field and CW cooling laser, after which a single pump pulse, or a single dump pulse, or a pair of pump and dump pulse, is sent to the atoms for excitation, after which fluorescence is measured with a photodiode. The dump pulse is 310 ps behind the pump pulse, by introducing a beam path length difference of $\approx$ 10 cm. Pulse picking is enabled by the pulse picker, which is a Conoptics Model 360-80 Pockels cell.

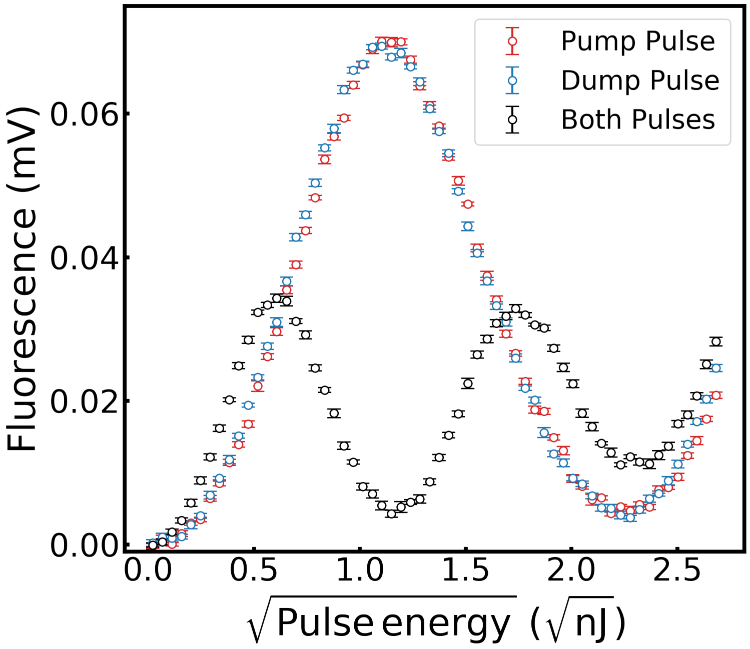

Figure 3.5: Fluorescence from single pulse pulse (red), dump pulse (blue) and pump-dump pulse pair (black). We vary the laser pulse energy with an acousto-optical modulator. Each data point is an average over 2000 runs where each run a single ML pulse or pulse pair is illuminated onto the atomic cloud. The fluorescence is collected with a Thorlabs PDA36A photodiode. A sample averaged time trace of fluorescence is shown in Figure 3.6.

This process is repeated 2000 times per pulse energy for averaging.

The results are demonstrated in Figure 3.5. The red points, blue points and black data points are the fluorescence obtained from the pump pulse only, dump pulse only, and pump-then-dump pulse pair configurations, respectively. The measured fluorescence is taken from the maximum value of a fluorescence time series in scope trace (see sample scope trace see Figure 3.6). The pump beam and dump beam need to be carefully mode-matched (including beam size, power and alignment matching) for best signal.

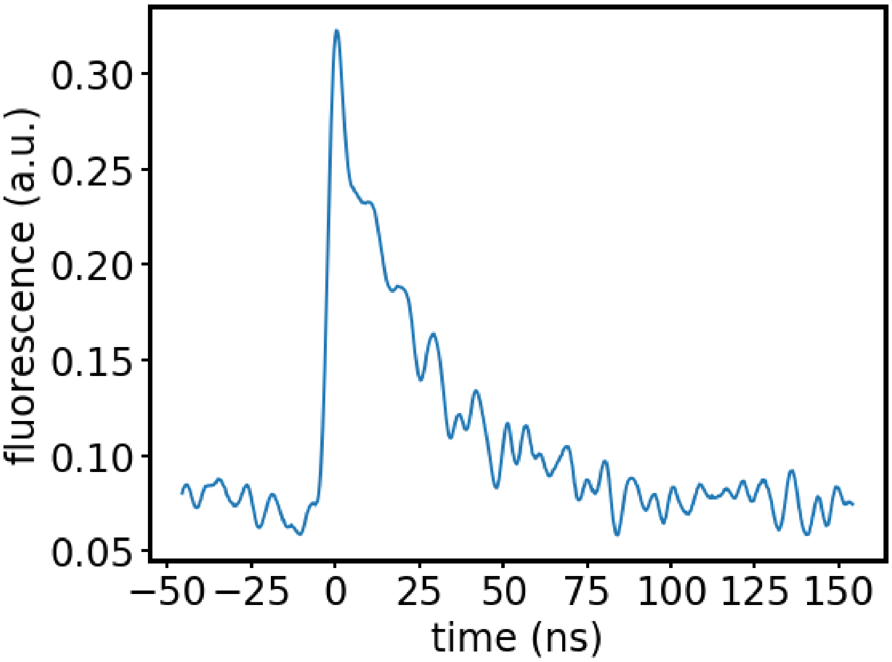

Figure 3.6: Sample time trace of fluorescence after single ML pulse (pair) illumination. The maximum value of a trace is taken as the fluorescence of a particular data run.

At the best signal, the pump beam and dump beam signals match almost exactly at every laser power (equivalently electric field strength, as is plotted in Figure 3.5). The pump-then-dump signal should be at a local minima at where the pump and dump only signals are at local maxima. This is expected if this laser power corresponds to the π-pulse condition.

It should be noted that the π-pulse condition as indicated by the single pulse maxima and pump-then-dump local minima happens at a pulse energy of $\sim$ 1.2 nJ, or $\sim$ 96 mW time averaged power. This value is in reasonable agreement with the 81 mW laser power predicted in Section 3.4.2, and provides a calibration of $\frac{w_0^2}{T_\mathrm{p}}$, both of which are difficult to measure precisely.

Another thing to note in Figure (3.5) is that the y axis is given in mV, whereas we want it converted to excitation probability. In order to compare our results to the theory we have derived in Section (3.4.3), we need to calibrate the level of fluorescence corresponding to an excitation probability of 1. While it is not possible to do so experimentally, Section (3.4.3) shed some light to how a combination of data and theory could allow such a calibration.

Consider $\left\langle \bar{N}_\gamma(\theta) \right\rangle$ and $\bar{P}_1(\theta, \kappa)$ at π-pulse condition. Using Eq. (3.61) and (3.66), we can find the ratio between them:

$$\mu = \frac{\left\langle \bar{N}_\gamma(\pi) \right\rangle}{\bar{P}_1(\pi, \kappa)} = \frac{1 - \frac{3}{4}\mathrm{e}^{-\gamma\tau} + (1 - \mathrm{e}^{-\gamma\tau})(2\bar{P}_\kappa - 1) - \frac{1}{4}\mathrm{e}^{-\gamma\tau}(2\bar{P}_\kappa - 1)^4}{\bar{P}_\kappa} \tag{3.67}$$

In terms of quantities we can measure, the ratio μ corresponds to the ratio between $V_2(\pi)$ and $V_1(\pi)$ in Figure (3.5), since $V_1(\pi)$ and $V_2(\pi)$ corresponds to the pump-only or dump-only, and pump-then-dump fluorescence at π-pulse condition:

$$\mu = \frac{V_2(\pi)}{V_1(\pi)} \tag{3.68}$$

For purpose of calibration, fluorescence signal from pump-only and dump-only data are averaged per laser power, and we obtain

$$V_1(\pi) = (69.72 \pm 0.49)\mathrm{mV}, \tag{3.69}$$

$$V_2(\pi) = (4.26 \pm 0.50)\mathrm{mV}. \tag{3.70}$$

Subsequently, we can find the value of μ:

$$\mu = 0.0611 \pm 0.0072. \tag{3.71}$$

From Eq. (3.67) and (3.71), we get

$$\boxed{\bar{P}_\kappa = 0.980 \pm 0.005}. \tag{3.72}$$

The uncertainty is obtained by combining the uncertainty from the fluorescence measurements and the uncertainty from the pump-dump pulse delay. The corresponding fractional standard deviation κ can be found to be

$$\kappa = 0.09 \pm 0.01. \tag{3.73}$$

It should be mentioned that we have tried to measure κ experimentally to investigate whether κ is dominated by temporal fluctuation in ML laser pulse energy. 10000 ML pulses

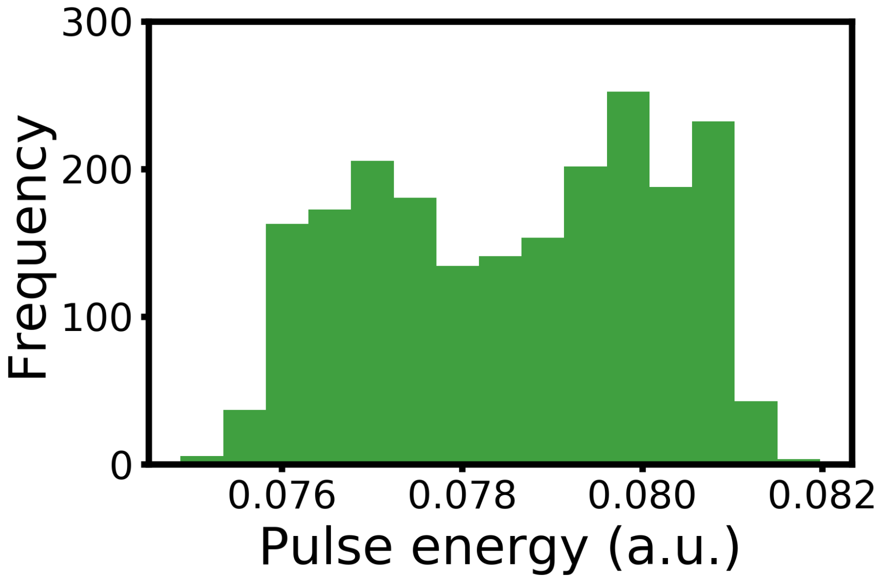

Figure 3.7: Laser power fluctuation. 10000 ML pulses are reflected off a microscope slide onto a SM05PD2A photodiode, and are then binned for the histogram. The y-axis is a counting of the frequency of different laser power occurrence. The fractional standard deviation of the shown data is 0.02.

sampled by a microscope slide are reflected onto a SM05PD2A photodiode. A fractional standard deviation of 2% in laser power is obtained (see Figure 3.7), corresponding to 1% fractional standard deviation in pulse area. Therefore transverse intensity variation of the beam across the atomic sample is speculated to be the cause of the large volume of κ extracted from the fluorescence measurements.

At this point, we infer the π-pulse area and characterize the x-axis of Figure 3.5 using Eq. (3.61), as shown in Figure 3.8. Theoretical values for single pulse fluorescence and pump-then-dump fluorescence are also plotted on Figure (3.8), as the purple dashed curve and the grey dashed curve, respectively. As a test of consistency of this model (Eq. (3.61) and (3.65)), we can compute the value of $\bar{P}_1$ at the 2π-pulse condition:

$$\bar{P}_1(2\pi, \kappa) = 0.07 \pm 0.02. \tag{3.74}$$

The measured value of $\bar{P}_1(2\pi, \kappa)_{\text{measured}}$ is $\bar{P}_1(2\pi, \kappa)_{\text{measured}} = 0.059 \pm 0.008$, in agreement

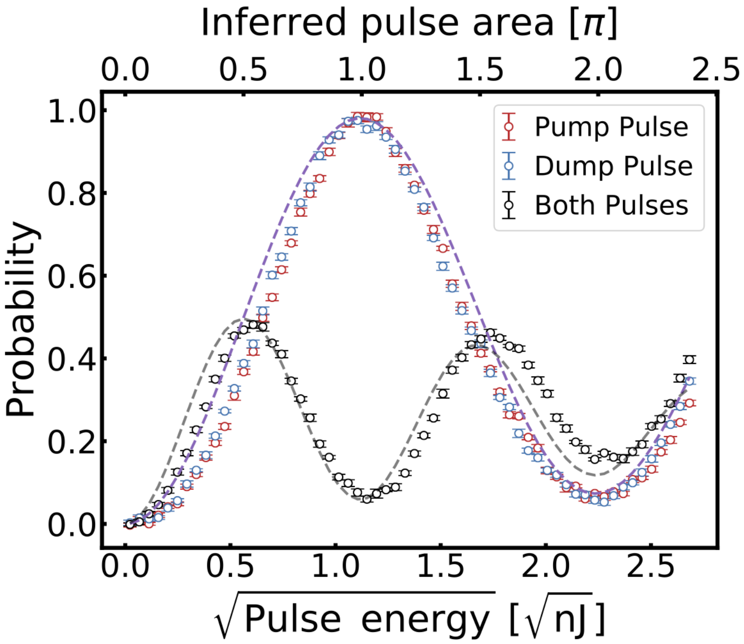

Figure 3.8: Fits to fluorescence data. The y-axis is obtained from the calibration method described in Section 3.4.4. The purple dashed line shows the fitting result of single pulse data to Eq. (3.61), and the gray dashed line is calculated with Eq. (3.65) using parameters obtained from single pulse data fitting.

with the theory.

3.5 Momentum Transfer with ML Pulse Stimulated Force

In this section, we continue to develop the theory from the previous section to benchmark the effectiveness of transferring momentum with ML pulse stimulated force. We also compare the experimental results with the theoretical predictions.

3.5.1 Theoretical Description of Momentum Transfer from a ML Pulse Stimulated Force

We have derived the expected number of spontaneous emission events per pulse (pair) in Section 3.4.3, and we can calculate the expected number of momentum transfer per pulse pair $\langle n_{\hbar k}(\theta)\rangle$ from the number of spontaneous emission events. Specifically, in our formalism in Section 3.4.3, the initial momentum of an atom in state $|i, n\rangle$ is

$$p_i = n\hbar k, \tag{3.75}$$

and the final momentum state right after the dump pulse is a superposition of different momentum states, with the probabilities given by the diagonal matrix elements of Eq. (3.56). The expected momentum of the final state p_f can be calculated as

$$p_f \quad = \quad \left[n + 2\mathrm{e}^{-\gamma\tau}\sin^4\left(\frac{\theta}{2}\right)\right]\hbar k. \tag{3.76}$$

Hence the number of expected momentum transfer after this pump-dump pulse pair is

$$\langle n_{\hbar k}(\theta)\rangle = \frac{p_f - p_i}{\hbar k} = 2\mathrm{e}^{-\gamma\tau}\sin^4\left(\frac{\theta}{2}\right). \tag{3.77}$$

Similar to Section 3.4.3, we want to average over different pulse area θ to account for the finite sample size:

$$\begin{aligned}\langle \bar{n}_{\hbar k}(\theta)\rangle &= \int_{-\infty}^{\infty} D(\theta)\langle n_{\hbar k}(\theta)\rangle \mathrm{d}\theta \\ &= 2\mathrm{e}^{-\gamma\tau}\int_{-\infty}^{\infty} D(\theta)\sin^4\left(\frac{\theta}{2}\right)\mathrm{d}\theta \\ &= \boxed{\frac{1}{4}\mathrm{e}^{-\gamma\tau}\left(3+\mathrm{e}^{-2\kappa^2\theta_{\mathrm{o}}^2}\cos\left(2\theta_{\mathrm{o}}\right)-4\mathrm{e}^{-\kappa^2\theta_{\mathrm{o}}^2/2}\cos\left(\theta_{\mathrm{o}}\right)\right)}. \end{aligned} \tag{3.78}$$

At the π-pulse condition, $\theta_{\mathrm{o}} = \pi$,

$$\langle \bar{n}_{\hbar k}(\pi)\rangle = e^{-\gamma\tau}\left(\frac{3}{4}+(2\bar{P}_{\kappa}-1)+(2\bar{P}_{\kappa}-1)^4\right). \tag{3.79}$$

The overall efficiency of the ML pulse stimulated force can be obtained by dividing $\langle \bar{n}_{\hbar k}(\theta_{\mathrm{o}})\rangle$ by 2:

$$\epsilon_{\mathrm{ML}} = \frac{1}{2}\langle \bar{n}_{\hbar k}(\pi)\rangle = \frac{1}{8}e^{-\gamma\tau}\left(3+4(2\bar{P}_{\kappa}-1)+4(2\bar{P}_{\kappa}-1)^4\right). \tag{3.80}$$

3.5.2 Experimental Characterization of Momentum Transfer with a ML Pulse Stimulated Force

The experimental measurement done on population transfer fidelity in Section 3.4.4, and theoretical derivation in Section 3.5.1 provide an upper bound on the performance of the ML pulse stimulated force. In this section, we report the direct measurement on the effectiveness momentum transfer from ML pulse stimulated force.

As illustrated in Figure 3.9, we illuminate a cloud of atoms at rest with 1000 pump-dump ML pulses, and measure the final speed of the atoms by performing time-of-flight (TOF) measurements along the direction of the pump pulse beam. A resonant, cw laser beam centered 4-6 mm away from the initial position of the atomic cloud in the direction of the stimulated force is used to record absorption as a function of time for atoms accelerated by the pump-dump pulse pairs.The pump-dump pulse pairs are separated from one another by 250 ns. This delay is enabled by a Conoptics Model 360-80 pulse picker (see Section 5.2), and is chosen such to minimize potential comb tooth effects. Figure 3.10 shows the relevant time intervals and frequencies for this experiment.

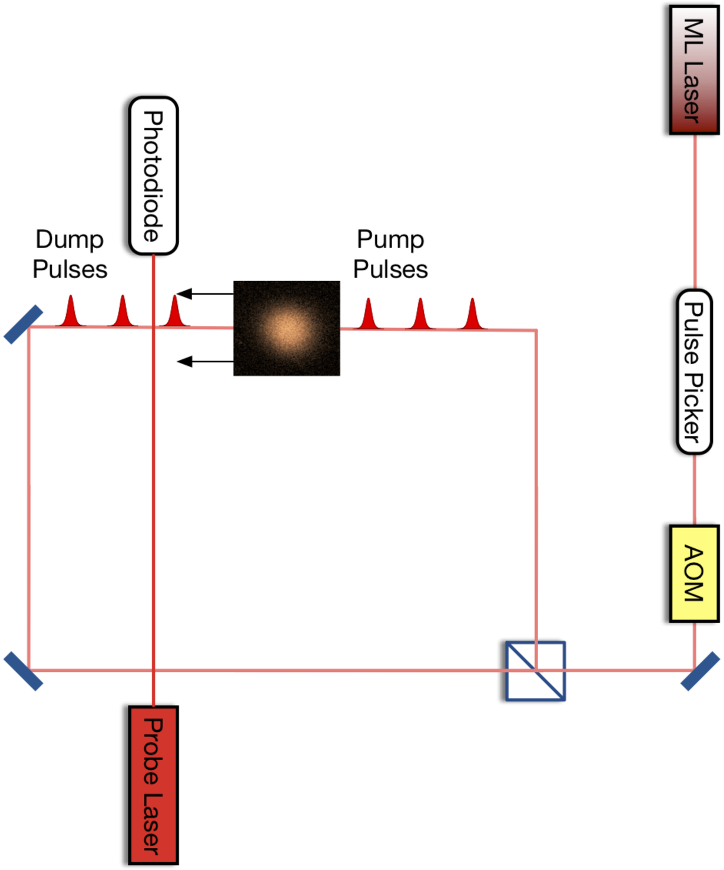

Figure 3.9: Experiment setup for measuring momentum transfers resulted from ML laser pulse. A resonant probe laser is placed at different displacements along the pump beam direction for time-of-flight measurement. The pulse picker allows pulse pairs to be introduced into the interaction region every 250 ns. This timing is chosen to eliminate potential comb tooth effects, such that a P-state Rb atom, excited by a first pulse pair, decays to the ground state 99.99% of the time when the next pulse comes in.

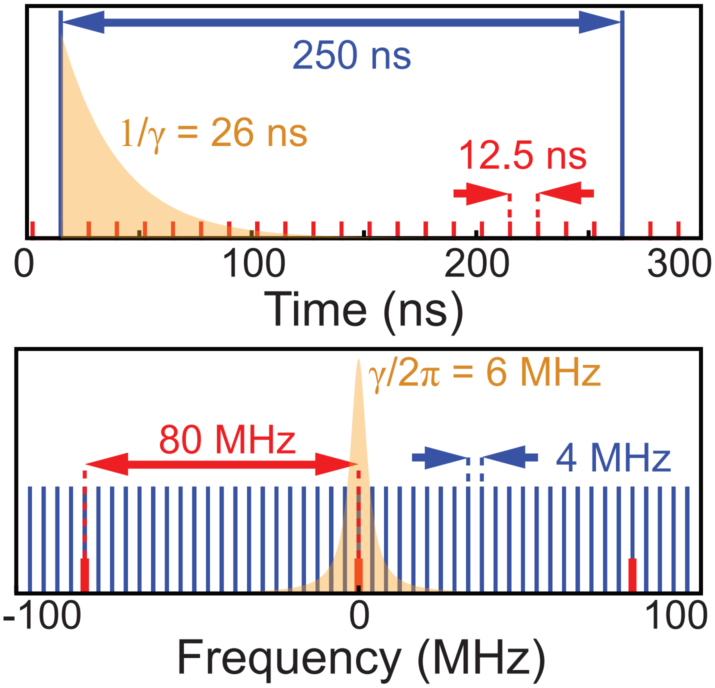

Figure 3.10: Time domain (upper) and frequency domain (lower) illustration of single-beam processes in this work. The ML laser generates 30 ps pulses at 12.5 ns intervals (80 MHz, red). A Pockels cell increases this inter-pulse delay to 250 ns (4 MHz, blue) to ensure $> 99.99\%$ decay probability between pulses. The excited state probability for an atom excited by the first pulse is represented by the yellow area in the time domain figure. The corresponding atomic spectrum is shown in the frequency domain figure.

We vary the ML pulse energy to find the optimal pulse energy that gives the earliest arrival times, which corresponds to the largest number of momentum transfers from 2000 total possible momentum transfers of $\hbar k$. Two typical traces are plotted in Figure 3.11. The blue "good" trace has an earlier arrival time than the orange "bad" trace, indicating a better ML pulse energy to use to efficiently transfer momentum to the atoms.

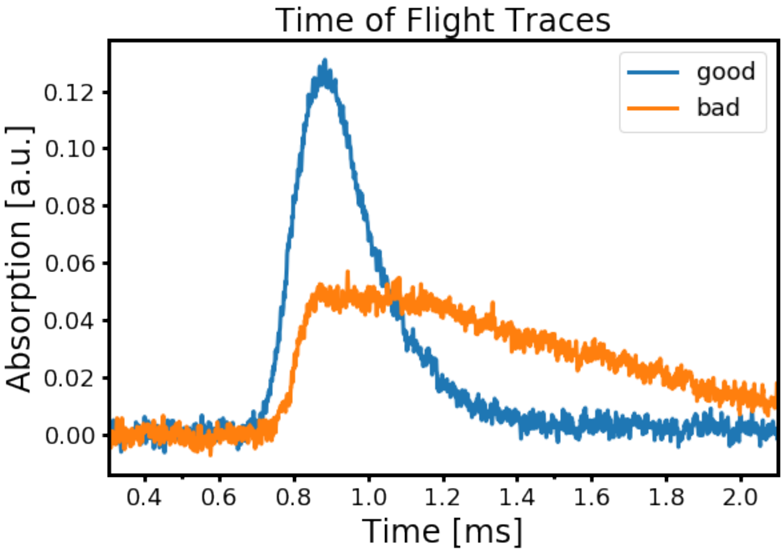

Figure 3.11: TOF traces of a good (high population transfer fidelity) versus bad (low population transfer fidelity) ML laser pulse power for efficient momentum transfer. A TOF trace with an earlier arrival time, marked by an earlier rising edge, corresponds to a better momentum transfer efficiency and hence a higher population transfer fidelity.

The effect of of varying ML pulse energy on TOF measurements are demonstrated in Figure 3.12. In proximity to the π-pulse energy, the stimulated force becomes more efficient, resulting in better acceleration and earlier arrival times. Further, as the population transfer fidelity nears 1, the outcome of each pulse pair becomes more deterministic, and a narrower speed distribution follows. For perfect population transfer, the final speed distribution has a spread exactly equal to the starting velocity distribution, while for a population transfer fidelity of 50%, the pulse pairs impose a random walk to the atoms, resulting in a velocity spread proportional to $\sqrt{N}$, where N is the number of pulse pairs. The clumping up of atoms during earlier arrival times for the data with better population transfer fidelity in Figure 3.12 is a result of narrower speed distribution. While the observed spread in arrival times of the atoms are clearly on the order of 0.1 ms, the spread expected from quantum projection noise is on the order of 0.01 ms (See Appendix A). This much wider spread implies systematic variations in population transfer fidelity associated with the nonuniform transverse intensity profiles of the beams. Some locations in space thus experience systematically higher population transfer fidelity than others. We are most interested in these atoms since these represent the ensemble most interesting for considering future applications to molecules. As such, we focus on optimizing the fastest moving 10% of the atomic population.

We park the ML laser pulse energy at a power that gives optimal momentum transfer (earliest arrival timein Figure 3.12), and vary the location of the TOF detection probe laser at 5 different displacement from the initial MOT location. The arrival times of the fastest moving 10% of the atoms are plotted in Figure 3.14. For these atoms, we obtain a velocity of (11.0 ± 0.3) m/s, corresponding to a total momentum transfer of $(1820 \pm 50)\hbar k$ from 2000 pulses. Using this momentum transfer efficiency, Eq. 3.80 can be solved for the effective average π-pulse population transfer fidelity, yielding $\bar{P} = (0.958 \pm 0.014)$. The lower values of $\bar{P}$ measured from *in situ* acceleration measurements as compared to those inferred from few-pulse fluorescence experiments (e.g. Fig. 3.8) highlight the need to perform measurements of this kind by measuring the actual momentum transfer, which is sensitive to more potential systematic effects than observations of internal state dynamics.

3.5.3 Comb Tooth Effect

Despite the 0.7% extinction ratio obtained from the pulse picker, small comb tooth effects can become important for a long pushing sequence. To investigate the comb tooth effect from our pulses, we scan the frequency of the nearest comb tooth by applying scanning the ML laser cavity piezo voltage. Similar to Section 3.5.2, we perform TOF measurement at 3 different displacements for all frequencies. We then calculate the speed and predicted initial position via a linear fit from the arrival times of the fastest 10% of the atoms in each TOF

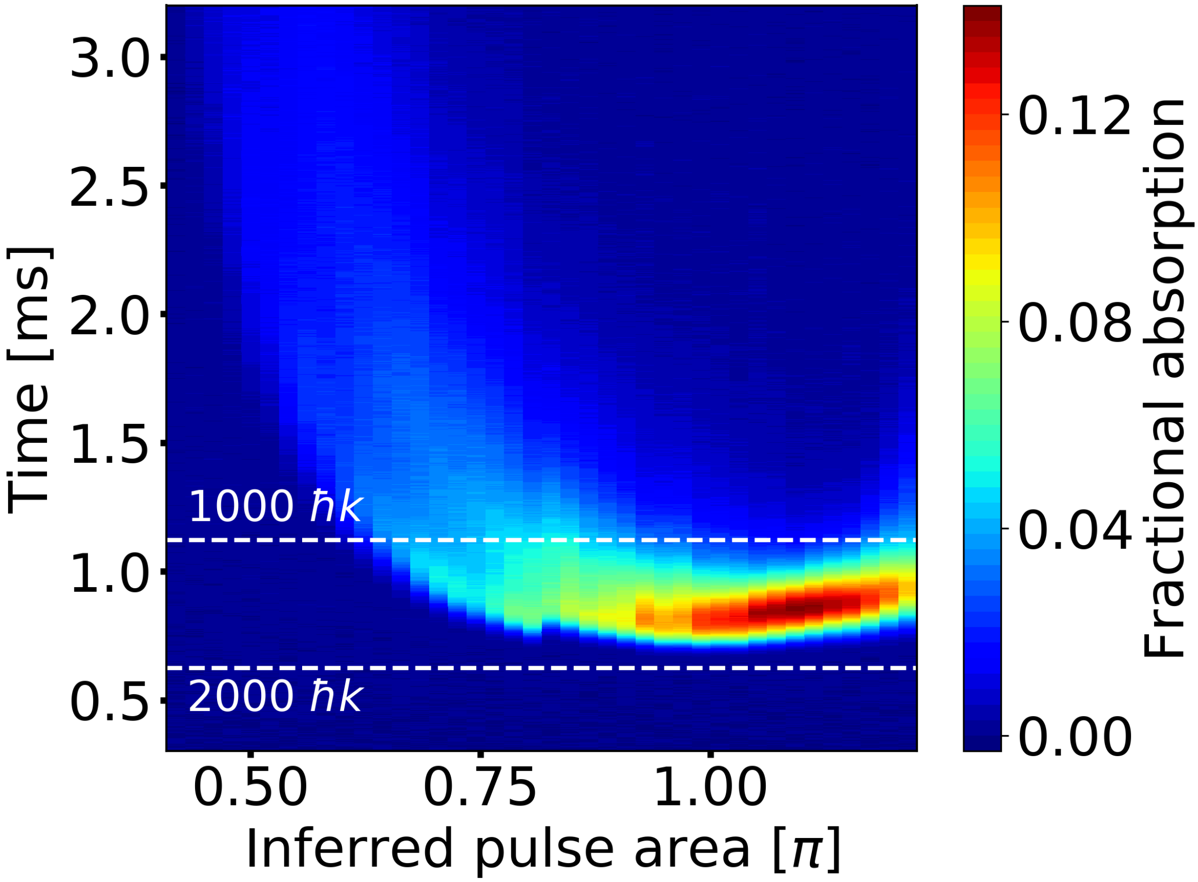

Figure 3.12: Effect of varying pulse energy on the arrival times of the atoms at the TOF detection position. Each vertical cross-section is a TOF trace (see Fig 3.13). The dashed guide lines represent the theoretical arrival times if the indicated momentum had been transfered to the atoms. These diagnostic data were taken before optimizing the force, and the arrival times of the fastest 10% atoms corresponds to $\Upsilon \approx 6$.

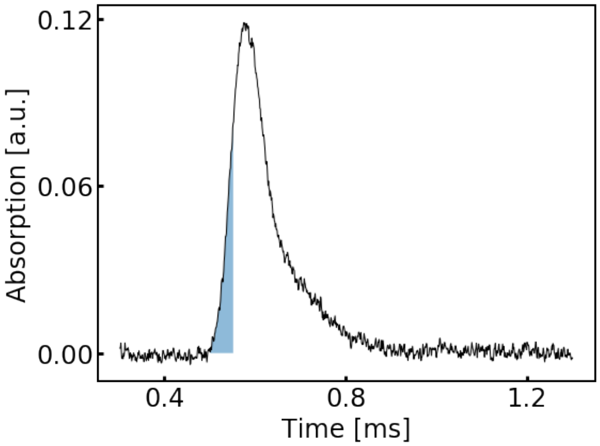

Figure 3.13: Sample TOF trace used to calculate the arrival time of the fastest 10% of the atoms (blue shaded region) with a 4.5 mm displacement from the initial atomic cloud position.

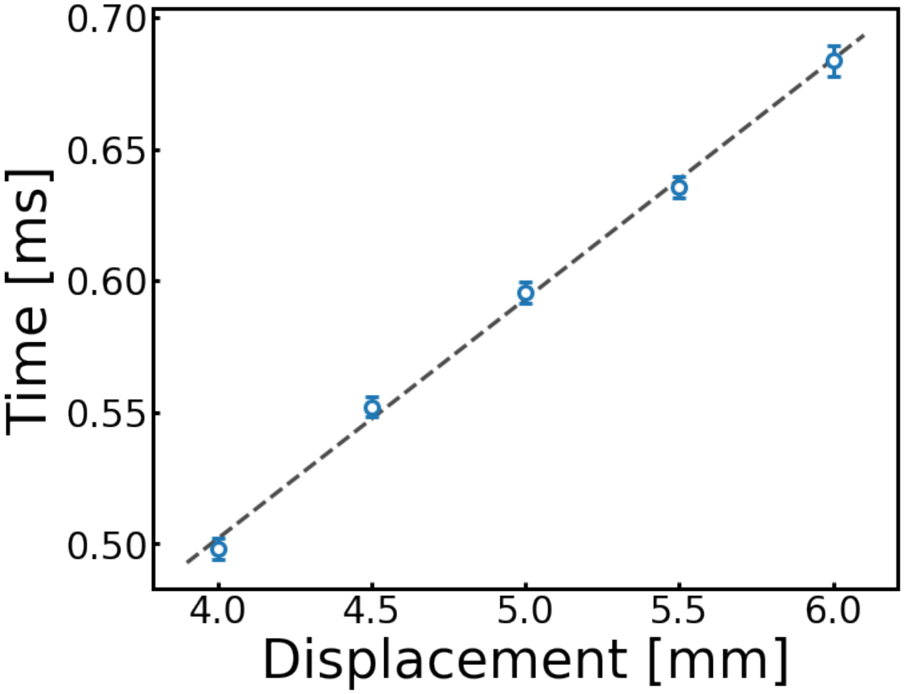

Figure 3.14: Arrival times of the fastest 10% of the atoms at 5 different TOF detection positions, and the velocity fit (dashed line) obtained from the position and time data.

trace. The results are shown in Figure 3.15. The spikes in arrival time around 0 V, 4 V and 8 V correspond to nearest comb tooth frequencies that are in resonance with the atomic transition. Away from the proximity of the atomic transition, the nearest comb tooth has little effects on the fitted speeds and initial positions.

Figure 3.16 shows the calculated quasi-steady-state normalized scattering rate for illumination by a ML pulse train. We calculate the comb tooth visibility for our experiment parameters. The comb tooth visibility for the desired pushing pulses with a 250 ns separation is 0.017, consistent with the observation from Figure 3.15 in frequency ranges away from the resonance frequencies. To ensure the comb tooth effects are minimized in this experiment, we therefore choose a long pump-dump pulse pair separation of 250 ns, and deliberately adjust the ML laser comb tooth positions such that no frequency comb tooth is near the transition.

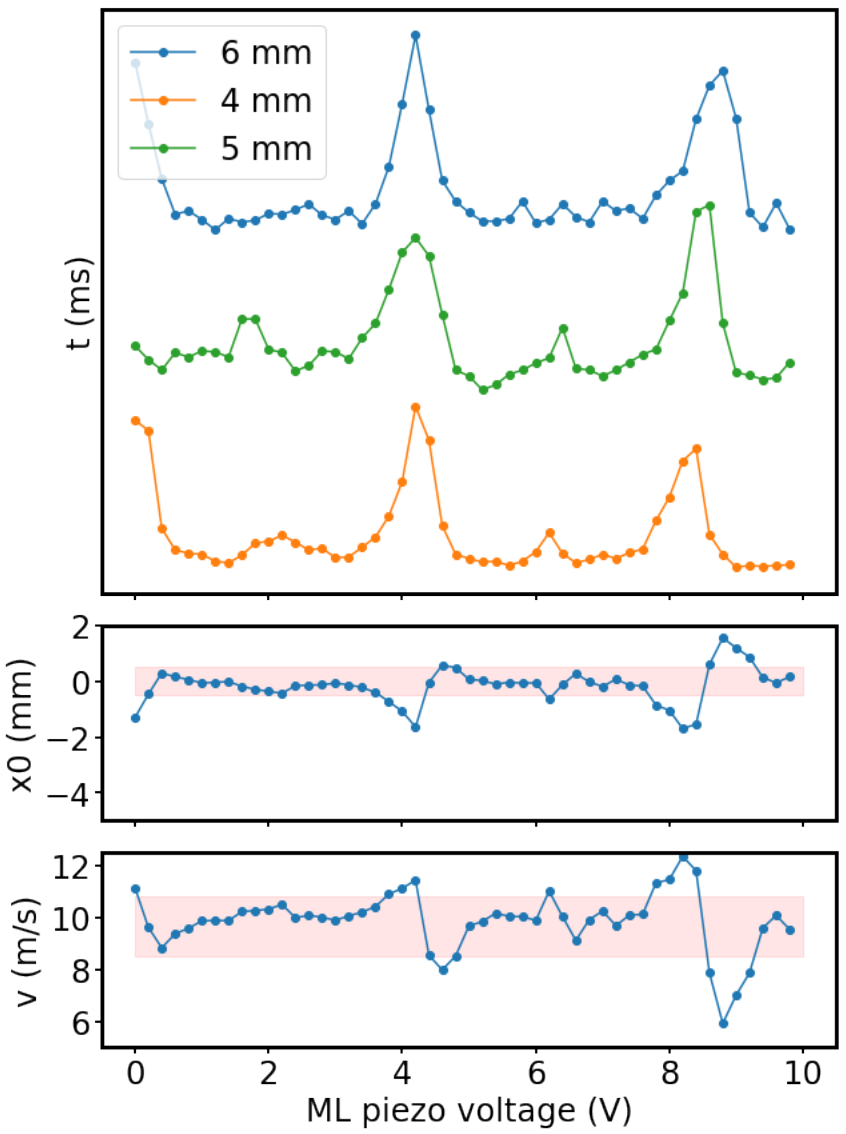

Figure 3.15: Stimulated force comb tooth dependence. The top plot shows the arrival times of the fastest 10% of the atoms for different ML laser cavity piezo voltages. The spikes in arrival time around 0 V, 4 V and 8 V correspond to nearest comb tooth frequencies that are in resonance with the atomic transition. The middle and bottom plots are the fitted initial positions and final speeds after momentum transfers from the arrival times. Away from the proximity of the atomic transition, the nearest comb tooth has little effect on the speed and initial position. The pink band in the middle and bottom plots shows the range of initial positions and speeds that fitted initial positions and falls speeds falls into for the data not in the proximity of the atomic transition.

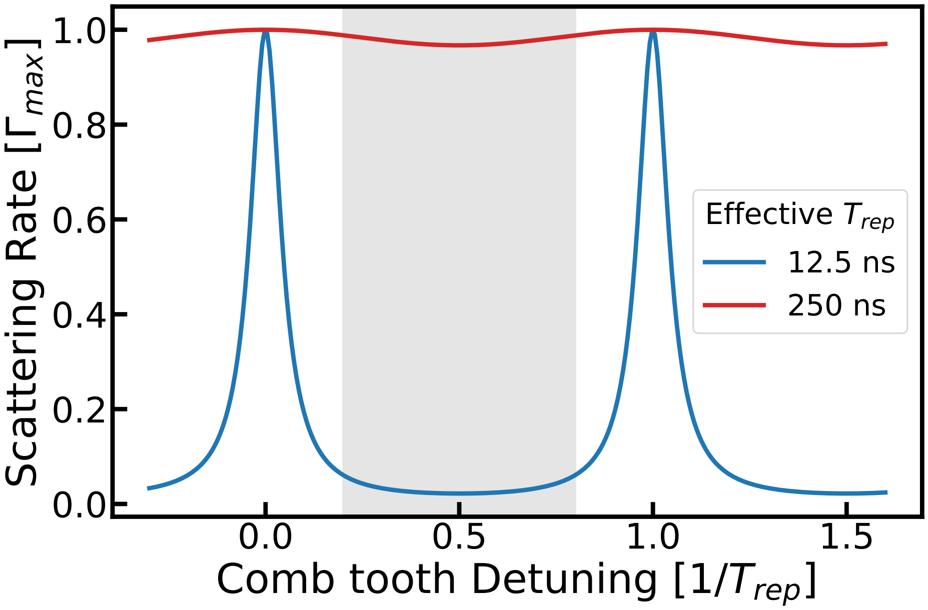

Figure 3.16: Calculated quasi-steady-state normalized scattering rate for illumination by a ML pulse train. For the experiments in this work, the frequency comb was operated in the shaded region with respect to the blue curve.

3.6 Comparison of the ML Pulse Stimulated Force to Other Forces

As mentioned in Section 3.1, one advantage of the stimulated force over spontaneous scattering force is the large number of momentum transfers that can be delivered before a spontaneous emission happens, which reduces the possibility of molecules falling into dark states. A reasonable figure of merit for evaluating the gain in requisite cycle closure of stimulated over spontaneous scattering is the average momentum transferred (in units of the photon momentum, $\hbar k$) per spontaneous emission event, which we denote by the symbol Υ. For spontaneous scattering, $\Upsilon = 1$. For most stimulated scattering schemes, the stimulated processes can be driven quickly compared to the spontaneous emission lifetime, and the stimulated force can therefore be stronger than the spontaneous scattering force by a factor of approximately Υ.

For the work in Section 3.4 and 3.5, we assume full spontaneous emission of any excited population before the next pulse pair. This allows us to write the figure of merit Υ as

$$\Upsilon = \frac{\langle \bar{n}_{\hbar k}(\pi) \rangle}{\langle \bar{N}_{\gamma}(\pi) \rangle} = \left(\frac{8\bar{P}_{\kappa}}{\mathrm{e}^{-\gamma\tau}\left(3 + 4(2\bar{P}_{\kappa} - 1) + (2\bar{P}_{\kappa} - 1)^4\right)} - 1 \right)^{-1} . \tag{3.81}$$

Note that Υ is evaluated at the π-pulse condition because we are trying to look for the maximal attainable factor gain. For the population transfer fidelity obtained by fluorescence measurement in Section 3.4, $\bar{P}_{\kappa} = 0.980 \pm 0.005$, giving $\Upsilon = 32 \pm 4$, while for the population transfer fidelity obtained by directly measure the speed of atoms illuminated by a ML pulse train with TOF in Section 3.5, $\bar{P}_{\kappa} = 0.958 \pm 0.014$, and the figure of merit $\Upsilon = 19^{+6}_{-4}$.

Comparison of this measurement of Υ to other methods in the literature is complicated by the fact that very few demonstrations of stimulated slowing techniques report the average gains in cycle closure that they are designed to provide (though a recent demonstration of the bichromatic force on polyatomic molecules [62] achieved $\Upsilon = (3.7 \pm 0.7)$ [61]). Two other performance indicators are more common: the excited state fraction, which determines the ensemble-averaged radiative decay rate, and the force gain factor, which is the ratio of the magnitude of the stimulated force over the theoretical maximum radiative force for an ideal two-level system. The time-averaged excited state fraction induced by the bichromatic force for a two-level system can be optimized to 41%, though it could be improved further to 24% with a four-color force scheme [36]. The pulsed scheme in this work can be viewed as a polychromatic limit of the bichromatic force, and the time-averaged pump-then-dump excited state fraction achieved here is $(1.0 \pm 0.2)\%$. Likewise, experimental work on bichromatic deflection has demonstrated a force gain factor improvement of 1.1 [62] on polyatomic molecules and a similar value on diatomic molecules [37], whereas spontaneous scattering force experiments on polyatomic [64] and diatomic [88] molecules have shown force gain factors of 0.5 and 0.29 respectively. With the intentionally low repetition rate adopted in our measurement to eliminate comb tooth systematics (See Section 3.5.3), we measure a force gain factor of (0.38 ± 0.01), already comparable to spontaneous scattering.

3.7 Application of the ML Pulse Stimulated Force

One possible application of this scheme would be for laser deceleration of YbOH, a polyatomic molecule candidate for future measurements of the electron electric dipole moment [29]. White light slowing with five repump lasers has been proposed to produce a spontaneous scattering force sufficient for stopping a beam of YbOH [65], whereas use of this pulsed stimulated optical force with $\Upsilon = 19$ would reduce the number of repump lasers by three, and is likely to apply a much stronger force, thereby increasing the molecular flux. Other applications for the pulsed stimulated force include those for which spontaneous emission leads to decoherence of quantum superpositions of momentum states, such as atom interferometry and trapped ion entangling gates [60, 57, 99, 15, 45].

CHAPTER 4

Conclusion

In this thesis, I present my work on two experiments: direct frequency comb laser cooling and trapping on a two-photon transition, and demonstration of a stimulated force that has suppressed spontaneous emissions.

Despite the success in both demonstrations, neither experiments are likely to be pursued further in the Campbell group. Optical frequency comb laser cooling of hydrogen on a two photon transition would require a lot of laser power in the ultraviolet, and would require a slowing stage to slow hydrogen to a laser coolable speed. Laser slowing of molecules with the ML laser pulse stimulated force would also require additional laser power to expand the ML laser beam size that would slow down a comparable number of molecules as other slowing methods, for example white light slowing. Nevertheless, with enough knowledge on the molecule structure and with enough laser power, the ML laser pulse stimulated force could be a promising candidate to efficiently slow down a molecular beam.

CHAPTER 5

Experiment Apparatus and Software

In this chapter, we document the apparatus and software used in experiments for future reference.

5.1 LabRAD

LabRAD (Lab Rapid Application Development) is a software platform developed and maintained by the Martinis Group at the University of California, Santa Barbara. It is designed for research or production environment requiring complex instrument control and/or data acquisition. It provides a platform to break up a complex software project into small, manageable modules that can be written in different programming languages, run on different computers, and independently maintained by different developers [3].

The work presented in this thesis uses pyLabRAD [4], a Python interface to Labrad. Servers and clients used to control experiment apparatus can be found in [1] and [2].

5.2 Tsunami Mode-locked Ti:sapphire laser

A mode-locked laser is a laser that applies either passive or active mode-locking such that different frequency component can be locked in-phase and constructively interfere, resulting in emission of ultrashort pulses. We use a Spectra-Physics Tsunami Mode-locked Ti:sapphire laser for both experiments in Chapter 2 and Chapter 3.

We use LabRAD to control the switching on and off of the Tsunami ML laser. To ensure mode-locking, the output of the ML laser is sampled to a Electro-Optics Tech GaAs ET-

4000 photodiode, whose signal is then sent to a spectrum analyzer. We use the spread and steadiness of the comb observed on the spectrum analyzer as an indicator for the robustness of mode-locking (see Figure 5.1). It is possible to change the temporal pulse width produced by the ML laser. The Gires-Tournois interferometers inside the ML laser needs to be replaced.

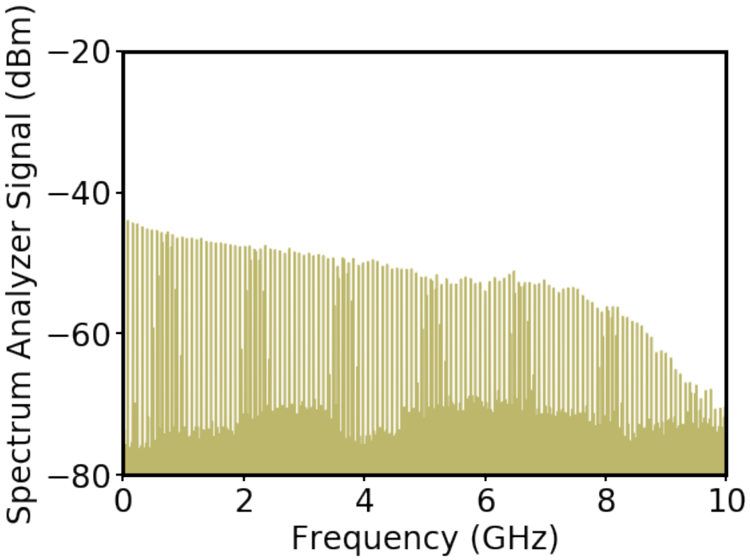

Figure 5.1: Illustration of a spectrum analyzer data for a well-mode-locked frequency comb. The frequency comb seen by the spectrum analyzer is the beating signal between different frequency comb teeth. The comb spreads out to 10 GHz, which is the cutoff frequency of the GaAs ET-4000 photodiode.

5.2.1 Pulse Picking with Conoptics Pockels Cell

We use a Conoptics Model 360-80 Modulator for pulse selection. The pulse picker is controlled by a Conoptics Model 305 Synchronous Countdown module and is amplified with a Conoptics Model 25D. We prepare a ML laser beam with a $1/e^2$ intensity radius of ≈ 1.5 mm with a max time-averaged laser power of ≈ 2.2 W. Higher laser power makes extinction ratio inconsistent, which might be due to heating in the modulator crystal. We use a Glan-laser polarizer (Thorlabs GL10-B) to clean up polarization before the ML laser beam enters the pulse picker. To characterize the extinction ratio of the pulse picker, set the pulse picker trigger mode to single shot mode (S.S. on the Model 305 front panel) on the pulse picker electronics, and send in a series of TTL pulses to the pulse picker. A microscope slide is used to sample ML laser pulses onto a photodiode, which can be connected to a scope. By carefully aligning the ML beam with respect to the pulse picker, and tuning the BIAS Control knob on the Model 25D amplifier, a minimum extinction ratio of 0.7% can be reached.

5.2.2 Locking the ML laser

For the experiment described in Chapter 2, we frequency lock the optical frequency comb to stabilize the nearest comb tooth with respect to the two-photon resonance for the $5S \rightarrow 5D$ two-photon transition in rubidium (Figure 2.4). We sample a fraction of the laser power and send it to a hot Rb vapor cell in a counter-propagating geometry [82]. Each excitation to the $5^2D_{5/2}$ state produces a spontaneously emitted 420 nm photon as part of a cascade decay 6.5% of the time (Fig. 2.4), which is collected from the pulse collision volume and monitored with a photon-counting detector.

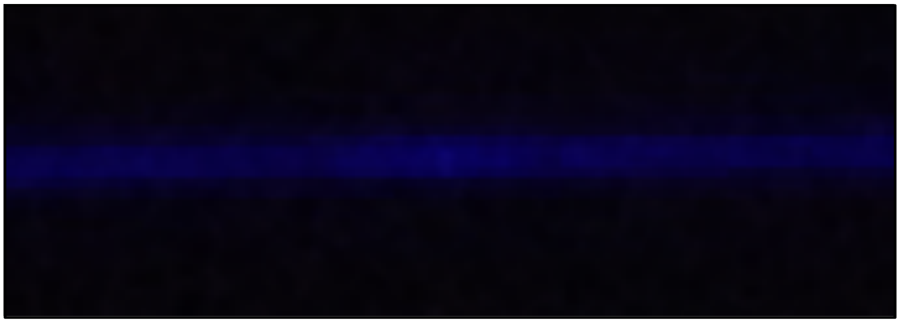

Figure 5.2: Heated rubidium vapor cell. Two counter-propagating 778 nm beams are introduced into the rubidium vapor cell and overlapped. The blue trace is the fluorescence from the $6\ ^2P_{3/2} \rightarrow 5\ ^2S_{1/2}$ transition with a 420 nm, where the $6\ ^2P_{3/2}$ state is a decay product from the $5\ ^2D_{5/2}$ state, which is the two-photon transition excited state. The tiny bright spot in the middle is a Doppler free region where mode-locked laser pulses collide.

To maintain sufficient laser stability for Doppler cooling and trapping, we stabilize the

ML laser by locking it to an external cavity. The free spectral range of the external cavity is pressure tuned to be an integer multiple ($q = 25$) of the ML laser repetition rate to guarantee that multiple teeth from across the laser spectrum contribute to the Pound-Drever-Hall error signal used for the lock. A piezo-mounted mirror on the external cavity is then used to stabilize it to the $5^2S_{1/2}, F_\mathrm{g} = 3$ to $5^2D_{5/2}, F_\mathrm{e} = 5$ line using FM spectroscopy of the vapor cell. We note that this optical frequency comb is not self referenced and that we feed back to an unknown combination of f_r and f_0 to maintain the two-photon resonance condition, which is the only frequency parameter that needs to be actively stabilized. The pulse chirp is periodically minimized by adjusting a Gires-Tournois interferometer in the laser cavity to maximize the blue light emitted from atoms in the initial CW MOT. The frequency of the ML laser light used for cooling and trapping is tuned from the vapor cell lock point using an acousto-optic modulator downstream.

5.3 CW Lasers

We use a total of three CW lasers for the experiments described in Chapter 2 and Chapter 3: a reference laser (*Bamm Bamm*) that is locked by saturated absorption (sat-abs) spectroscopy, a main cooling laser for the MOT (*Pebbles*), and a repump laser (*Dino*).

5.3.1 Saturated Absorption Lock

We use saturated absorption spectroscopy [35] to lock a reference laser to the $^{85}\mathrm{Rb}\ 5^2S_{1/2} \rightarrow 5^2P_{3/2}$ transition. Figure 5.3.

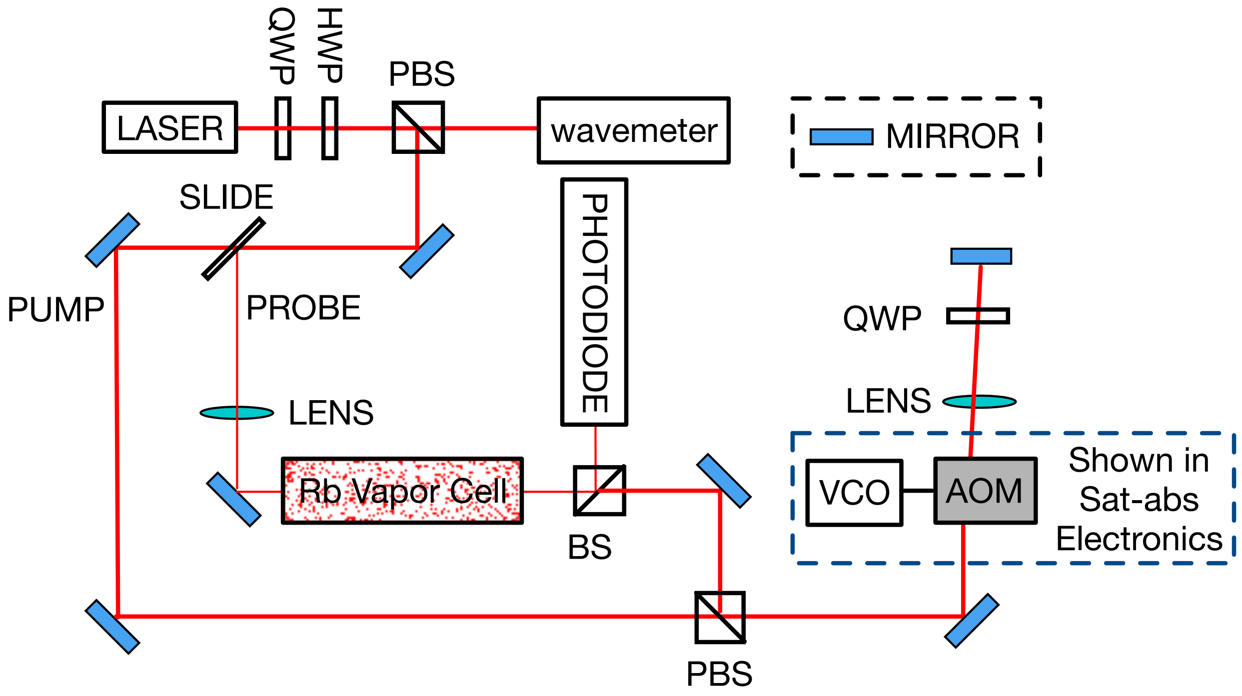

Figure 5.3: Schematic for the saturated absorption lock. Some beam pointing mirrors for easier alignments have been removed from the schematic drawing for simplicity.

The sat-abs reference laser made from a Photodigm PH780DBR180T8 DBR laser diode. We use a Stanford SRS laser diode controller box to control the laser. Error signal from the electronics is sent to a New Focus LB1005 Servo controller to feed back to the laser controller. A schematic of the electronics circuits for the sat-abs lock is shown in Figure 5.4. A sample trace from the saturated absorption signal for locking is shown in Figure 5.5

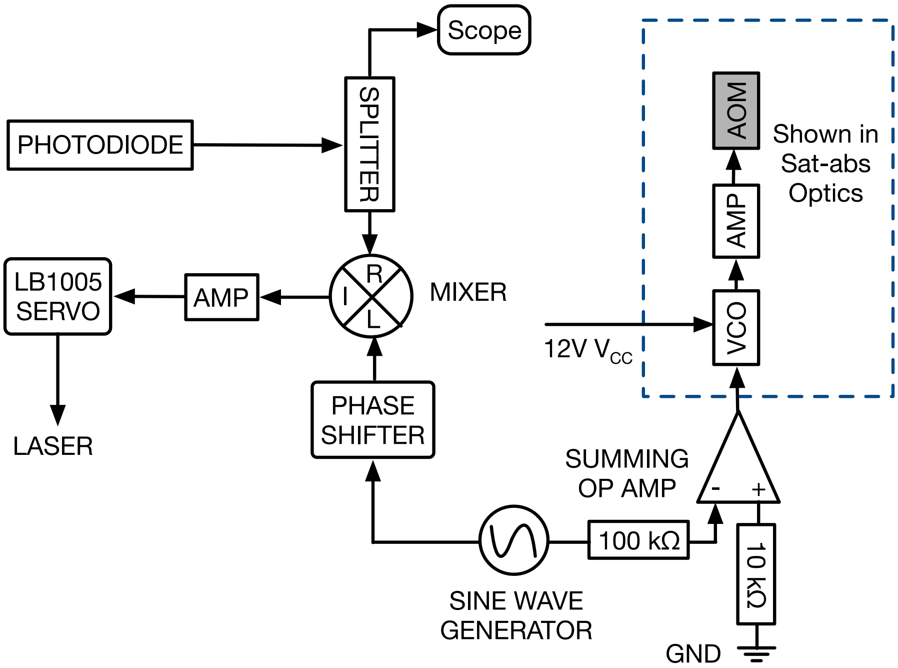

Figure 5.4: Electronics circuit for the saturated absorption lock.

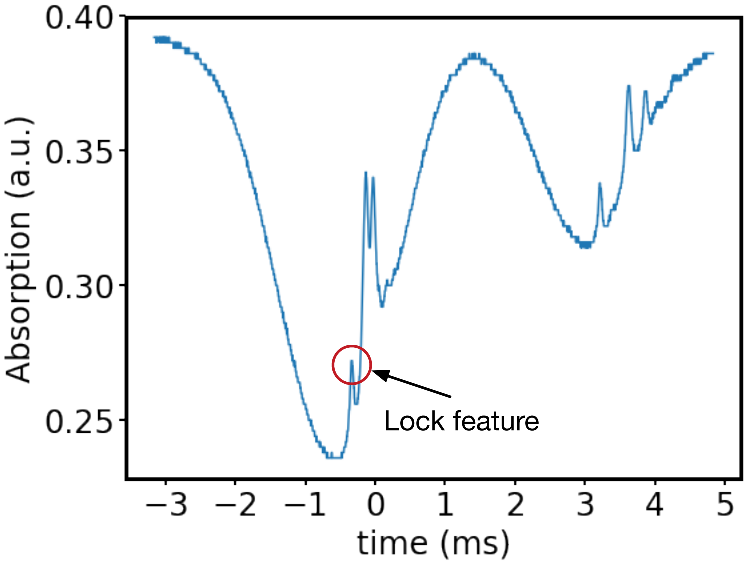

Figure 5.5: Saturated absorption lock signal. The feature to lock to is indicated by the arrow.

5.3.2 Cooling and Repumping Lasers

Both the cooling laser and repumping lasers are offset-locked to the reference sat-abs laser [85]. The schematic setup for the offset lock optics are drawn in Figure 5.6. LASER 1 (the reference laser) and LASER 2 (the cooling or the repump laser) in Figure 5.6) are combined by a beam splitter and the polarization is cleaned up with a polarizing beam splitter, and their beating is then detected with a photodiode.

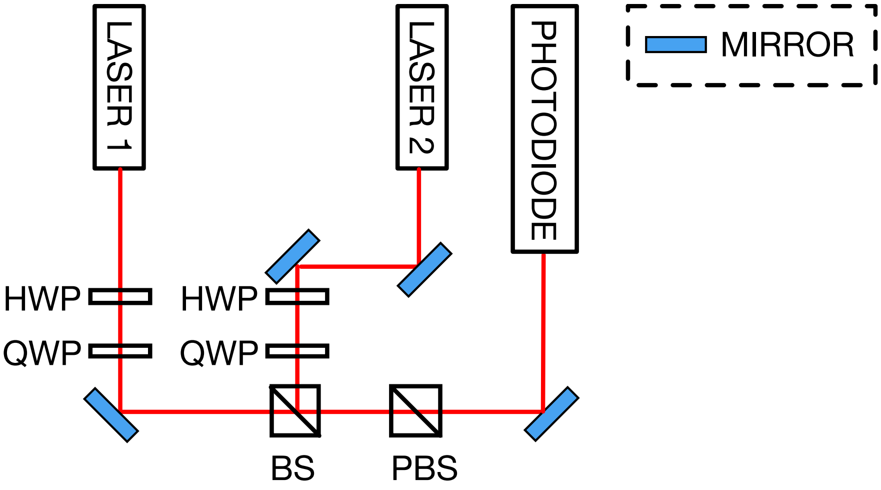

Figure 5.6: Schematic for the offset lock optics.

The cooling laser is made from a Photodigm PH780DBR120T8 DBR laser diode. Same as the reference laser, we use a Stanford SRS laser diode controller to control the cooling laser. The repump laser is a homemade external cavity diode laser, which is controlled by a MOGLab laser controller box. The schematic of the electronics circuit to produce the feedback error signal is shown in Figure 5.7.

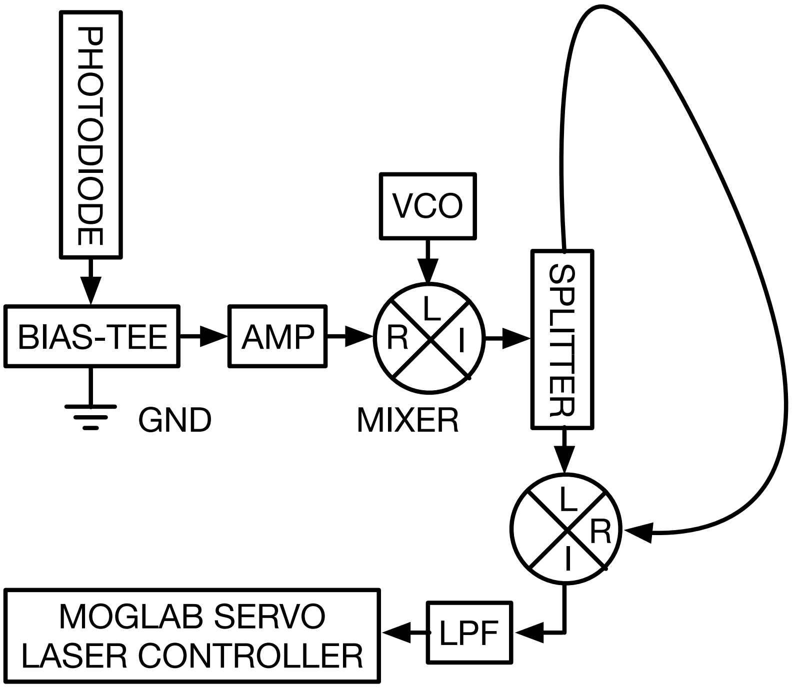

Figure 5.7: Electronics circuit for the saturated offset lock.

Appendix A

Variance in Number of Momentum Transfers and Spread in TOF Arrival Times

Getting the arrival time of the absolute maximum absorption for each of the 5 different TOF measurement position, and fitting to a straight line results in a max-density speed of 9.8 m/s, or 81.4% overall pushing efficiency. This corresponds to $\langle \bar{n}_{\hbar k}(\pi) \rangle = 1.63$, $\bar{P} = 89.8\%$ using Eq. (3.80) and Eq. (3.79), and $\kappa = 0.215$ using Eq. (3.61)

If we denote the probability of getting $n\hbar k$ per pulse pair by $\mathcal{P}_n$, and assume the pump and dump beams are exactly the same so that $\mathcal{P}_1 = \mathcal{P}_{-1}$, then from the calculation above, $\mathcal{P}_2 = 0.814$. By combining and integrating terms in Eq. (3.56), we can find $\mathcal{P}_1 = \mathcal{P}_{-1} = 0.0747$, and $\mathcal{P}_0 = 1 - \mathcal{P}_{-1} - \mathcal{P}_1 - \mathcal{P}_2$. These outcomes form a multinomial distribution, whose definition are given in [96]. Instead of following the terminologies in [96], it is easier to interpret the multinomial distribution as N independent *categorical trials* [97]. A categorical distribution is a discrete probability distribution whose sample space is the set of n individually identified items. It is the generalization of the Bernoulli distribution for a categorical random variable, which is a random variable that takes on one of a limited number of possible values. The probability mass function f is:

$$f(x = i \mid \boldsymbol{p}) = p_i, \tag{A.1}$$

where $\boldsymbol{p} = (p_1, \ldots, p_n)$, p_i represents the probability of seeing element i and $\displaystyle\sum_{i=1}^{n} p_i = 1$.

Let X_i for $i = 1, \ldots, N$ denote the outcome of N independent trials to sample from a categorical distribution, and $X = \displaystyle\sum_{i=1}^{N} X_i$. Then we can find the variance of each X_i by definition:

$$\mathrm{Var}(X_i) = E(X_i^2) - E(X_i)^2, \tag{A.2}$$

and the total variance of X is given by

$$\mathrm{Var}(X) = \sum_{i=1}^{N} \mathrm{Var}(X_i) = N\mathrm{Var}(X_1) \tag{A.3}$$

since these are N independent trials.

Now back to our case. We have $p_1 = \mathcal{P}_2 = 0.814$, $p_2 = \mathcal{P}_1 = p_3 = \mathcal{P}_{-1} = 0.075$, $p_4 = \mathcal{P}_0 = 1 - \mathcal{P}_{-1} - \mathcal{P}_1 - \mathcal{P}_2 = 0.036$, and the outcome of each category $x_1 = 2$, $x_2 = 1$, $x_3 = -1$, $x_4 = 0$. Then

$$E(X_1^2) = \sum_{i=1}^{n} p_i x_i^2 = 0.814 * 4 + 0.075 * 1 + 0.075 * 1 + 0 = 3.406. \tag{A.4}$$

Then

$$\mathrm{Var}(X_1) = E(X_1^2) - E(X_1)^2 = 3.406 - 1.628^2 = 0.756, \tag{A.5}$$

hence $\mathrm{Var}(X) = 1000 \times \mathrm{Var}(X_1) = 756$, standard deviation is then 27.5. Then the max-density speed is 9.8 ± 0.2, which would give a uncertainty of $approx 15\,\mu$m for a displacement of 4.5 mm. In contrast, from Figure 3.13, the spread in arrival time is clearly on the order of 100 μm. Therefore the difference in momentum transfer fidelity is not due to quantum projection noise.

Appendix B

Dual Species MOT

This appendix reports the production of a dual species MOT of rubidium 85 and 87 with a single ML laser as the cooling and repumping laser. The experiment was performed by Andrew Jayich, a previous postdoc and now an assistant professor at University of California, Santa Barbara. The author of this thesis was not involved in this experiment. This appendix is put in this thesis since the author is the only graduate student working on its subsequent experiment.

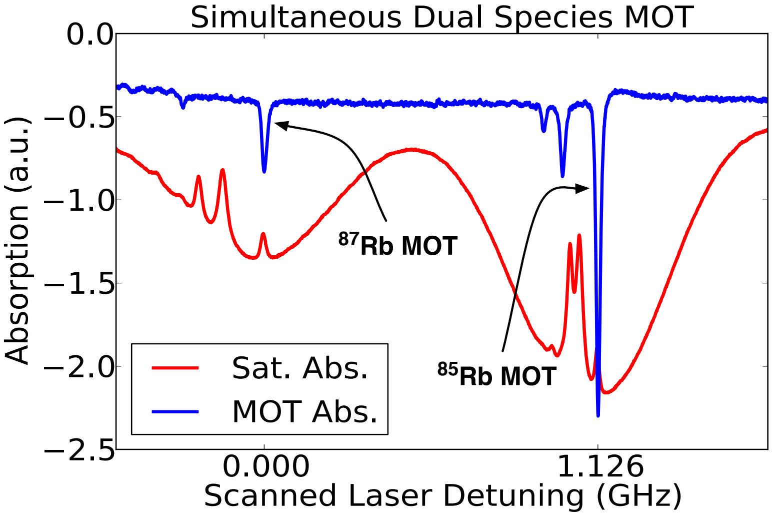

Figure B.1: Simultaneous dual species MOT absorption as probe laser frequency is scanned. A saturated absorption spectroscopy is performed simultaneously as the probe laser is scanned.

Due to the many different frequency components in an optical frequency comb, a single ML laser can simultaneously act as the cooling and repumping laser for laser cooling and trapping. In addition, because of its broad bandwidth, the ML laser can simultaneously address multiple species. In Campbell lab a dual species MOT has been produced with a single ML laser. Similar to a regular CW laser MOT (see Section 2.3), three pairs of counter-propagating ML lasers beams orthogonal to one another overlap in a rubidium vapor cell that is subject to the inhomogeneous magnetic field produced by a anti-Helmholtz coil. Both nearest comb teeth, one for ^{85}Rb and one for ^{87}Rb, must both be red-detuned to allow cooling. A weak CW probe laser illuminates on the atomic sample, whose absorption signal is collected with a photodiode.

Figure B.1 shows the absorption spectrum of the dual species MOT as the frequency of probe laser is scanned. To identify the absorption peaks, the same probe laser is used to perform a saturated absorption spectroscopy on a rubidium vapor cell simultaneously. The laser frequencies for making a ^{85}Rb MOT and a ^{87}Rb are indicated by two arrows.

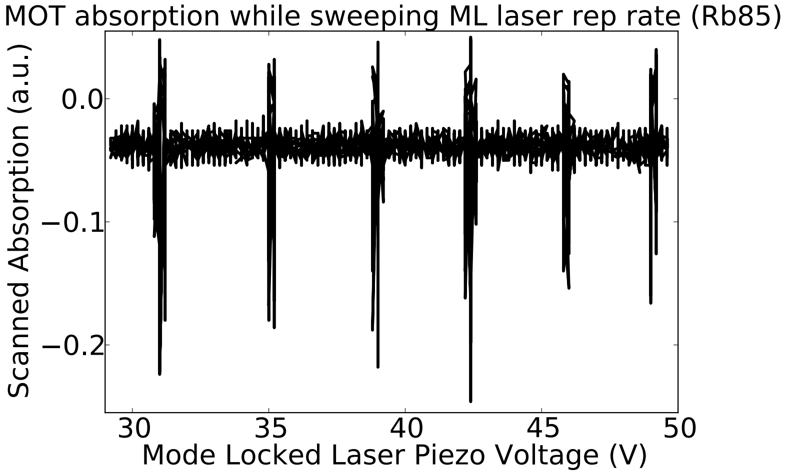

Figure B.2: Simultaneous dual species MOT absorption as the nearest comb tooth to the cooling transition is scanned. The periodicity demonstrates that a single comb tooth is responsible for the laser cooling and trapping.

To verify the optical power comes primarily from a single tooth of the optical frequency comb, the frequency of the nearest comb tooth to the ^{85}Rb $5^2S_{1/2} \rightarrow 5^2P_{3/2}$ transition is scanned by scanning the piezo voltage applied to a ML laser cavity mirror. This changes the length of the ML laser cavity length, which changes the repetition frequency f_{r} and hence the frequency of the nearest comb tooth (See Eq. 2.30). Figure B.2 shows the resulting absorption signal. The periodic absorptive feature demonstrates that a single frequency comb tooth is responsible for the cooling and trapping of ^{85}Rb.

BIBLIOGRAPHY

[1] Campbell lab common repository. https://github.com/CampbellGroup/common.

[2] Campbell lab molecules repository. https://github.com/CampbellMolecules/molecules/.

[3] Labrad. https://sourceforge.net/p/labrad/wiki/Home/.

[4] pylabrad. https://github.com/labrad/pylabrad.

[5] M. Ahmadi, B. X. R. Alves, C. J. Baker, W. Bertsche, E. Butler, A. Capra, C. Carruth, C. L. Cesar, M. Charlton, S. Cohen, R. Collister, S. Eriksson, A. Evans, N. Evetts, J. Fajans, T. Friesen, M. C. Fujiwara, D. R. Gill, A. Gutierrez, J. S. Hangst, W. N. Hardy, M. E. Hayden, C. A. Isaac, A. Ishida, M. A. Johnson, S. A. Jones, S. Jonsell, L. Kurchaninov, N. Madsen, M. Mathers, D. Maxwell, J. T. K. McKenna, S. Menary, J. M. Michan, T. Momose, J. J. Munich, P. Nolan, K. Olchanski, A. Olin, P. Pusa, C. Ø. Rasmussen, F. Robicheaux, R. L. Sacramento, M. Sameed, E. Sarid, D. M. Silveira, S. Stracka, G. Stutter, C. So, T. D. Tharp, J. E. Thompson, R. I. Thompson, D. P. van der Werf, and J. S. Wurtele. Observation of the 1s–2s transition in trapped antihydrogen. *Nature*, 541:506 EP –, 12 2016.

[6] Emine Altuntaş, Jeffrey Ammon, Sidney B. Cahn, and David DeMille. Demonstration of a sensitive method to measure nuclear-spin-dependent parity violation. *Phys. Rev. Lett.*, 120:142501, Apr 2018.

[7] Loïc Anderegg, Benjamin L. Augenbraun, Yicheng Bao, Sean Burchesky, Lawrence W. Cheuk, Wolfgang Ketterle, and John M. Doyle. Laser cooling of optically trapped molecules. *Nature Physics*, 14(9):890–893, 2018.

[8] Loïc Anderegg, Benjamin L. Augenbraun, Eunmi Chae, Boerge Hemmerling, Nicholas R. Hutzler, Aakash Ravi, Alejandra Collopy, Jun Ye, Wolfgang Ketterle, and John M. Doyle. Radio frequency magneto-optical trapping of caf with high density. *Phys. Rev. Lett.*, 119:103201, Sep 2017.

[9] A. André, D. DeMille, J. M. Doyle, M. D. Lukin, S. E. Maxwell, P. Rabl, R. J. Schoelkopf, and P. Zoller. A coherent all-electrical interface between polar molecules and mesoscopic superconducting resonators. *Nature Physics*, 2:636 EP –, Aug 2006. Article.

[10] D. Aumiler and T. Ban. Simultaneous laser cooling of multiple atomic species using an optical frequency comb. *Phys. Rev. A*, 85:063412, 2012.

[11] Y. V. Baklanov and V. P. Chebotayev. Narrow resonances of two-photon absorption of super-narrow pulses in a gas. *Applied Physics*, 12:97, 1977.

[12] M. A. Baranov, M. Dalmonte, G. Pupillo, and P. Zoller. Condensed matter theory of dipolar quantum gases. *Chemical Reviews*, 112(9):5012–5061, 2012. PMID: 22877362.

[13] J. F. Barry, D. J. McCarron, E. B. Norrgard, M. H. Steinecker, and D. DeMille. Magneto-optical trapping of a diatomic molecule. *Nature*, 512:286 EP –, Aug 2014.

[14] J. F. Barry, E. S. Shuman, E. B. Norrgard, and D. DeMille. Laser radiation pressure slowing of a molecular beam. *Phys. Rev. Lett.*, 108:103002, Mar 2012.

[15] C D B Bentley, A R R Carvalho, and J J Hope. Trapped ion scaling with pulsed fast gates. *New Journal of Physics*, 17(10):103025, oct 2015.

[16] D. J. Berkeland and M. G. Boshier. Destabilization of dark states and optical spectroscopy in zeeman-degenerate atomic systems. *Phys. Rev. A*, 65:033413, Feb 2002.

[17] Axel Beyer, Lothar Maisenbacher, Arthur Matveev, Randolf Pohl, Ksenia Khabarova, Alexey Grinin, Tobias Lamour, Dylan C. Yost, Theodor W. Hänsch, Nikolai Kolachevsky, and Thomas Udem. The rydberg constant and proton size from atomic hydrogen. *Science*, 358(6359):79–85, 2017.

[18] B. B. Blinov, Jr. R. N. Kohn, M. J. Madsen, P. Maunz, D. L. Moehring, and C. Monroe. Broadband laser cooling of trapped atoms with ultrafast pulses. *J. Opt. Soc. Am. B*, 23(6):1170–1173, Jun 2006.

[19] I. Bloch, J. Dalibard, and S. Nascimbène. Quantum simulations with ultracold quantum gases. *Nature Physics*, 8:267, 2012.

[20] R. Bluhm, V. A. Kostelecký, and N. Russell. CPT and Lorentz tests in hydrogen and antihydrogen. *Phys. Rev. Lett.*, 82:2254, 1999.

[21] K. D. Bonin and T. J. McIlrath. Two-photon electric-dipole selection rules. *J. Opt. Soc. Am. B*, 1:52, 1984.

[22] Wesley C. Campbell. Atomix excitation by a mode-locked pulse. 2 2017.

[23] Lincoln D Carr, David DeMille, Roman V Krems, and Jun Ye. Cold and ultracold molecules: science, technology and applications. *New Journal of Physics*, 11(5):055049, may 2009.

[24] S. F. Cooper, Z. Burkley, A. D. Brandt, C. Rasor, and D. C. Yost. Cavity-enhanced deep ultraviolet laser for two-photon cooling of atomic hydrogen. *Opt. Lett.*, 43(6):1375–1378, Mar 2018.

[25] J. Davila-Rodriguez, A. Ozawa, T. W. Hänsch, and T. Udem. Doppler cooling trapped ions with a uv frequency comb. *Phys. Rev. Lett.*, 116:043002, 2016.

[26] B. de Beauvoir, C. Schwob, O. Acef, L. Jozefowski, L. Hilico, F. Nez, L. Julien, A. Clairon, and F. Biraben. Metrology of the hydrogen and deuterium atoms: Determination of the rydberg constant and lamb shifts. *The European Physical Journal D - Atomic, Molecular, Optical and Plasma Physics*, 12(1):61–93, Sep 2000.

[27] M. H. G. de Miranda, A. Chotia, B. Neyenhuis, D. Wang, G. Quéméner, S. Ospelkaus, J. L. Bohn, J. Ye, and D. S. Jin. Controlling the quantum stereodynamics of ultracold bimolecular reactions. *Nature Physics*, 7:502, 2011.

[28] D. DeMille. Quantum computation with trapped polar molecules. *Phys. Rev. Lett.*, 88:067901, Jan 2002.

[29] Malika Denis, Pi A. B. Haase, Rob G. E. Timmermans, Ephraim Eliav, Nicholas R. Hutzler, and Anastasia Borschevsky. Enhancement factor for the electric dipole moment of the electron in the BaOH and YbOH molecules. *arXiv e-prints*, page arXiv:1901.02265, Jan 2019.

[30] S. M. Dickerson, J. M. Hogan, A. Sugarbaker, D. M. S. Johnson, and M. A. Kasevich. Multiaxis inertial sensing with long-time point source atom interferometry. *Phys. Rev. Lett.*, 111:083001, 2013.

[31] M. D. DiRosa. Laser-cooling molecules. *Eur. Phys. J. D*, 31:395, 2004.

[32] P. H. Donnan, M. C. Fujiwara, and F. Robicheaux. A proposal for laser cooling antihydrogen atoms. *J. Phys. B*, 46:025302, 2013.

[33] B. C. Duncan, V. Sanchez-Villicana, and P. L. Gould. Measurement of the Rb($5D_{5/2}$) photoionization cross section using trapped atoms. *Phys. Rev. A*, 63:043411, 2001.

[34] J. Dutta, B. B. Nath, P. C. Clark, and R. S. Klessen. The role of three-body H_2 formation in the fragmentation of primordial gas. *MNRAS*, 450:202, 2015.

[35] C.J. Foot. *Atomic physics*. Oxford master series in physics. Oxford University Press, 2005.

[36] S. E. Galica, L. Aldridge, and E. E. Eyler. Four-color stimulated optical forces for atomic and molecular slowing. *Phys. Rev. A*, 88:043418, Oct 2013.

[37] S. E. Galica, L. Aldridge, D. J. McCarron, E. E. Eyler, and P. L. Gould. Deflection of a molecular beam using the bichromatic stimulated force. *Phys. Rev. A*, 98:023408, Aug 2018.

[38] J. J. García-Ripoll, P. Zoller, and J. I. Cirac. Quantum information processing with cold atoms and trapped ions. *J. Phys. B*, 38:S567, 2005.

[39] A. Goepfert, I. Bloch, D. Haubrich, F. Lison, R. Schütze, R. Wynands, and D. Meschede. Stimulated focusing and deflection of an atomic beam using picosecond laser pulses. *Phys. Rev. A*, 56:R3354, 1997.

[40] F. Großmann. *Theoretical Femtosecond Physics: Atoms and Molecules in Strong Laser Fields*. Graduate Texts in Physics. Springer International Publishing, 2013.

[41] P. Hamilton, M. Jaffe, P. Haslinger, Q. Simmons, H. Müller, and J. Khoury. Atom-interferometry constraints on dark energy. *Science*, 349:849, 2015.

[42] P. Hamilton, A. Zhmoginov, F. Robicheaux, J. Fajans, J. S. Wurtele, and H. Müller. Antimatter interferometry for gravity measurements. *Phys. Rev. Lett.*, 112:121102, 2014.

[43] T. Haslwanter, H. Ritsch, J. Cooper, and P. Zoller. Laser-noise-induced population fluctuations in two- and three-level systems. *Phys. Rev. A*, 38:5652, 1988.

[44] H.A. Haus, C.V. Shank, and E.P. Ippen. Shape of passively mode-locked laser pulses. *Optics Communications*, 15(1):29 – 31, 1975.

[45] D. Heinrich, M. Guggemos, M. Guevara-Bertsch, M. I. Hussain, C. F. Roos, and R. Blatt. Ultrafast coherent excitation of a Ca\$$\hat{+}$\$ ion. *arXiv e-prints*, page arXiv:1812.08537, Dec 2018.

[46] Boerge Hemmerling, Eunmi Chae, Aakash Ravi, Loic Anderegg, Garrett K Drayna, Nicholas R Hutzler, Alejandra L Collopy, Jun Ye, Wolfgang Ketterle, and John M Doyle. Laser slowing of caf molecules to near the capture velocity of a molecular mot. *Journal of Physics B: Atomic, Molecular and Optical Physics*, 49(17):174001, 2016.

[47] E. Herbst. Chemistry in the interstellar medium. *Annu. Rev. Phys. Chem.*, 46:27, 1995.

[48] E A Hinds. Testing time reversal symmetry using molecules. *Physica Scripta*, 1997(T70):34, 1997.

[49] S. D. Hogan, A. W. Wiederkehr, H. Schmutz, and F. Merkt. Magnetic trapping of hyrdogen after multistage deceleration. *Phys. Rev. Lett.*, 101:143001, 2008.

[50] Eric R. Hudson and Wesley C. Campbell. Dipolar quantum logic for freely-rotating trapped molecular ions. *Phys. Rev. A*, 98:040302(R), 2018.

[51] M. T. Hummon, W. C. Campbell, H. Lu, E. Tsikata, Y. Wang, and J. M. Doyle. Magnetic trapping of atomic nitrogen (^{14}N) and cotrapping of NH ($X^3\Sigma^-$). *Phys. Rev. A*, 78:050702(R), 2008.

[52] M. T. Hummon, M. Yeo, B. K. Stuhl, A. L. Collopy, Y. Xia, and J. Ye. 2D magneto-optical trapping of diatomic molecules. *Phys. Rev. Lett.*, 110:143001, 2013.

[53] L. R. Hunter, S. K. Peck, A. S. Greenspon, S. Saad Alam, and D. DeMille. Prospects for laser cooling tlf. *Phys. Rev. A*, 85:012511, Jan 2012.

[54] E. Ilinova, M. Ahmad, and A. Derevianko. Doppler cooling with coherent trains of laser pulses and a tunable velocity comb. *Phys. Rev. A*, 84:033421, 2011.

[55] A. M. Jayich, X. Long, and W. C. Campbell. Direct frequency comb laser cooling and trapping. *Phys. Rev. X*, 6:041004, Oct 2016.

[56] A. M. Jayich, A. C. Vutha, M. T. Hummon, J. V. Porto, and W. C. Campbell. Continuous all-optical deceleration and single-photon cooling of molecular beams. *Phys. Rev. A*, 89:023425, Feb 2014.

[57] K. G. Johnson, J. D. Wong-Campos, B. Neyenhuis, J. Mizrahi, and C. Monroe. Ultrafast creation of large schrödinger cat states of an atom. *Nature Communications*, 8(1):697, 2017.

[58] A. P. Kazantsev. The acceleration of atoms by light. *Sov. Phys.-JETP*, 39:784, 1974.

[59] D. Kielpinski. Laser cooling of atoms and molecules with ultrafast pulses. *Phys. Rev. A*, 73:063407, 2006.

[60] T. Kovachy, P. Asenbaum, C. Overstreet, C. A. Donnelly, S. M. Dickerson, A. Sugarbaker, J. M. Hogan, and M. A. Kasevich. Quantum superposition at the half-metre scale. *Nature*, 528:530, Dec 2015.

[61] Ivan Kozyryev. private communication.

[62] Ivan Kozyryev, Louis Baum, Leland Aldridge, Phelan Yu, Edward E. Eyler, and John M. Doyle. Coherent bichromatic force deflection of molecules. *Phys. Rev. Lett.*, 120:063205, Feb 2018.

[63] Ivan Kozyryev, Louis Baum, Kyle Matsuda, and John M. Doyle. Proposal for laser cooling of complex polyatomic molecules. *ChemPhysChem*, 17:3641, 2018.

[64] Ivan Kozyryev, Louis Baum, Kyle Matsuda, Boerge Hemmerling, and John M Doyle. Radiation pressure force from optical cycling on a polyatomic molecule. *Journal of Physics B: Atomic, Molecular and Optical Physics*, 49(13):134002, jun 2016.

[65] Ivan Kozyryev and Nicholas R. Hutzler. Precision measurement of time-reversal symmetry violation with laser-cooled polyatomic molecules. *Phys. Rev. Lett.*, 119:133002, Sep 2017.

[66] A. E. Kramida. A critical compilation of experimental data on spectral lines and energy levels of hydrogen, deuterium, and tritium. *Atomic Data and Nuclear Data Tables*, 96:586, 2010.

[67] R. V. Krems. Cold controlled chemistry. *Phys. Chem. Chem. Phys.*, 10:4079–4092, 2008.

[68] P. D. Lett, W. D. Phillips, S. L. Rolston, C. E. Tanner, R. N. Watts, and C. I. Westbrook. Optical molasses. *J. Opt. Soc. Am. B*, 6:2084, 1989.

[69] J. Lim, J. R. Almond, M. A. Trigatzis, J. A. Devlin, N. J. Fitch, B. E. Sauer, M. R. Tarbutt, and E. A. Hinds. Laser cooled ybf molecules for measuring the electron's electric dipole moment. *Phys. Rev. Lett.*, 120:123201, Mar 2018.

[70] A. Marian, M. C. Stowe, J. R. Lawall, D. Felinto, and J. Ye. United time-frequency spectroscopy for dynamics and global structure. *Science*, 306:2063, 2004.

[71] Daniel J McCarron. Towards the mass production of slow, trappable molecules. *New Journal of Physics*, 20(5):051001, 2018.

[72] Harold Metcalf. Colloquium: Strong optical forces on atoms in multifrequency light. *Rev. Mod. Phys.*, 89:041001, 2017.

[73] A. Micheli, G. K. Brennen, and P. Zoller. A toolbox for lattice-spin models with polar molecules. *Nature Physics*, 2:341 EP –, Apr 2006. Article.

[74] Peter J. Mohr, David B. Newell, and Barry N. Taylor. Codata recommended values of the fundamental physical constants: 2014. *Rev. Mod. Phys.*, 88:035009, Sep 2016.

[75] B. Nölle, H. Nölle, J. Schmand, and H. J. Andrä. Atomic-beam deflection by double-Π-pulse laser technique. *Europhys. Lett.*, 33:261, 1996.

[76] E. B. Norrgard, D. J. McCarron, M. H. Steinecker, M. R. Tarbutt, and D. DeMille. Submillikelvin dipolar molecules in a radio-frequency magneto-optical trap. *Phys. Rev. Lett.*, 116:063004, Feb 2016.

[77] S. Ospelkaus, K.-K. Ni, D. Wang, M. H. G. de Miranda, B. Neyenhuis, G. Quéméner, P. S. Julienne, J. L. Bohn, D. S. Jin, and J. Ye. Quantum-state controlled chemical reactions of ultracold potassium-rubidium molecules. *Science*, 327(5967):853–857, 2010.

[78] Christian G. Parthey, Arthur Matveev, Janis Alnis, Birgitta Bernhardt, Axel Beyer, Ronald Holzwarth, Aliaksei Maistrou, Randolf Pohl, Katharina Predehl, Thomas Udem, Tobias Wilken, Nikolai Kolachevsky, Michel Abgrall, Daniele Rovera, Christophe Salomon, Philippe Laurent, and Theodor W. Hänsch. Improved measurement of the hydrogen $1s--2s$ transition frequency. *Phys. Rev. Lett.*, 107:203001, Nov 2011.

[79] M Petzold, P Kaebert, P Gersema, M Siercke, and S Ospelkaus. A Zeeman slower for diatomic molecules. *New Journal of Physics*, 20:042001, 2018.

[80] E. L. Raab, M. Prentiss, Alex Cable, Steven Chu, and D. E. Pritchard. Trapping of neutral sodium atoms with radiation pressure. *Phys. Rev. Lett.*, 59:2631, 1987.

[81] P. Rabl, D. DeMille, J. M. Doyle, M. D. Lukin, R. J. Schoelkopf, and P. Zoller. Hybrid quantum processors: Molecular ensembles as quantum memory for solid state circuits. *Phys. Rev. Lett.*, 97:033003, Jul 2006.

[82] S. Reinhardt, E. Peters, T. W. Hänsch, and T. Udem. Two-photon direct frequency comb spectroscopy with chirped pulses. *Phys. Rev. A*, 81:033427, 2010.

[83] N. Rosen and C. Zener. Double stern-gerlach experiment and related collision phenomena. *Phys. Rev.*, 40:502–507, May 1932.

[84] R. E. Ryan, L. A. Westling, R. Blümel, and H. J. Metcalf. Two-photon spectroscopy: A technique for characterizing diode-laser noise. *Phys. Rev. A*, 52:3157, 1995.

[85] U. Schünemann, H. Engler, R. Grimm, M. Weidemüller, and M. Zielonkowski. Simple scheme for tunable frequency offset locking of two lasers. *Review of Scientific Instruments*, 70(1):242–243, 1999.

[86] I. D. Setija, H. G. C. Werij, O. J. Luiten, M. W. Reynolds, T. W. Hijmans, and J. T. M. Walraven. Optical cooling of atomic hydrogen in a magnetic trap. *Phys. Rev. Lett.*, 70:2257–2260, Apr 1993.

[87] D. Sheng, A. P. Galván, and L. A. Orozco. Lifetime measurements of the 5d states of rubidium. *Phys. Rev. A*, 78:062506, 2008.

[88] E. S. Shuman, J. F. Barry, D. R. Glenn, and D. DeMille. Radiative force from optical cycling on a diatomic molecule. *Phys. Rev. Lett.*, 103:223001, Nov 2009.

[89] Matthew H. Steinecker, Daniel J. McCarron, Yuqi Zhu, and David DeMille. Improved radio-frequency magneto-optical trap of srf molecules. *ChemPhysChem*, 17(22):3664–3669, 2016.

[90] P. Strohmeier, T. Kersebom, E. Krüger, H. Nölle, B. Steuter, J. Schmand, and J. Andrä. Na-atom beam deceleration by a mode-locked laser. *Opt. Comm.*, 73:451, 1989.

[91] S Truppe, H J Williams, N J Fitch, M Hambach, T E Wall, E A Hinds, B E Sauer, and M R Tarbutt. An intense, cold, velocity-controlled molecular beam by frequency-chirped laser slowing. *New Journal of Physics*, 19(2):022001, 2017.

[92] S. Truppe, H. J. Williams, M. Hambach, L. Caldwell, N. J. Fitch, E. A. Hinds, B. E. Sauer, and M. R. Tarbutt. Molecules cooled below the doppler limit. *Nature Physics*, 13:1173 EP –, Aug 2017.

[93] V. S. Voĭtsekhovich, M. V. Danileĭko, A. M. Negriĭko, V. I. Romanenko, and L. P. Yatsenko. Observation of radiation pressure exerted on molecules. *JETP Lett.*, 59:408, 1994.

[94] A C Vutha, W C Campbell, Y V Gurevich, N R Hutzler, M Parsons, D Patterson, E Petrik, B Spaun, J M Doyle, G Gabrielse, and D DeMille. Search for the electric dipole moment of the electron with thorium monoxide. *Journal of Physics B: Atomic, Molecular and Optical Physics*, 43(7):074007, 2010.

[95] M. Watanabe, R. Ohmukai, U. Tanaka, K. Hayasaka, H. Imajo, and S. Urabe. Velocity control of an Yb beam by a frequency-doubled mode-locked laser. *J. Opt. Soc. Am. B*, 13:2377, 1996.

[96] Eric W Weisstein. Multinomial distribution. From MathWorld–A Wolfram Web Resource. http://mathworld.wolfram.com/MultinomialDistribution.html.

[97] Wikipedia contributors. Categorical distribution — Wikipedia, the free encyclopedia, 2019. https://en.wikipedia.org/wiki/Categorical_distribution.

[98] Dean A. Wilkening, Norman F. Ramsey, and Daniel J. Larson. Search for p and t violations in the hyperfine structure of thallium fluoride. *Phys. Rev. A*, 29:425–438, Feb 1984.

[99] J. D. Wong-Campos, S. A. Moses, K. G. Johnson, and C. Monroe. Demonstration of two-atom entanglement with ultrafast optical pulses. *Phys. Rev. Lett.*, 119:230501, 2017.

[100] Mark Yeo, Matthew T. Hummon, Alejandra L. Collopy, Bo Yan, Boerge Hemmerling, Eunmi Chae, John M. Doyle, and Jun Ye. Rotational state microwave mixing for laser cooling of complex diatomic molecules. *Phys. Rev. Lett.*, 114:223003, Jun 2015.

[101] V. Zehnlé and J. C. Garreau. Continuous-wave Doppler cooling of hydrogen atoms with two-photon transitions. *Phys. Rev. A*, 63:021402(R), 2001.

[102] V. Zhelyazkova, A. Cournol, T. E. Wall, A. Matsushima, J. J. Hudson, E. A. Hinds, M. R. Tarbutt, and B. E. Sauer. Laser cooling and slowing of caf molecules. *Phys. Rev. A*, 89:053416, May 2014.

[103] B. Zhu, B. Gadway, M. Foss-Feig, J. Schachenmayer, M. L. Wall, K. R. A. Hazzard, B. Yan, S. A. Moses, J. P. Covey, D. S. Jin, J. Ye, M. Holland, and A. M. Rey. Suppressing the loss of ultracold molecules via the continuous quantum Zeno effect. *Phys. Rev. Lett.*, 112:070404, 2014.